The Structure and Energetics of the Tropical Cyclone

By
William M. Frank

Department of Atmospheric Science
Colorado State University
Fort Collins, Colorado

Supported by grants: NOAA (NHEML) 04-6-022-44021, NOAA (NESS) 04-3-158-51,
and NSF ATM75-014240A01.
October 1976

Colorado State University

Department of Atmospheric Science

Paper No. 258

THE STRUCTURE AND ENERGETICS OF THE TROPICAL CYCLONE

by

William M. Frank

Department of Atmospheric Science

Colorado State University

Fort Collins, Colorado

October, 1976

Atmospheric Science Paper No. 258

ABSTRACT

THE STRUCTURE, DYNAMICS, AND ENERGETICS OF TROPICAL CYCLONES

This paper discusses the structure of tropical cyclones and the nature of the physical processes which maintain them. Analysis is based on a composite study of 10 years of northwest Pacific rawinsonde data ($\sim$ 18,000 soundings).

Tropical cyclones are found to exhibit strong persistent asymmetries. Horizontal eddy fluxes of momentum and kinetic energy are large and important to the large scale circulation, as are eddy generation and dissipation of kinetic energy. Vertical eddy fluxes of sensible heat, moisture and momentum accomplished by convective clouds are substantial. A simple cloud momentum flux parameterization is proposed. Substantial vertical mass recycling occurs in the middle and lower troposphere at all radii. Much of the convergence of mass and moisture is found to occur above the boundary layer suggesting that frictional convergence is not the sole forcing process of the radial circulation. Diurnal variations in temperature and precipitation are observed. Sea surface to air fluxes of sensible heat and moisture are smaller than those found in most previous studies. The mutual consistencies of the independent budget studies and the high accuracy of the uncorrected data support the usefulness of compositing as a valuable analysis technique.

TABLE OF CONTENTS

TABLE OF CONTENTS (cont'd)

1. INTRODUCTION

Tropical cyclones have been a subject of tropical meteorological interest in Europe since the voyages of Columbus and in Asia for over a millenium. Nevertheless, the large scale structure, dynamics and energetics of these storms are not well documented or understood due to previous limitations of conventional data sources over the oceans, difficulties in processing large amounts of data and large interstorm variabilities. This study employs the expanded data handling capacities and computational power of modern computers to process large amounts of rawinsonde data from many storms at many time periods. This allows the documentation and analysis of the persistent features of tropical cyclones to be made and increases our knowledge of the energetics of these systems.

The data set and compositing technique used are discussed in sections 1.3 and 1.4, and the detailed structure of tropical cyclones is presented in Chapters 2-4. The dynamics and energetics of these storms are analyzed in terms of budget studies of water vapor, moist static energy, angular momentum and kinetic energy in Chapters 5, 6, 7 and 8 respectively. The major findings are summarized in Chapter 9.

1.1 Overview of Tropical Cyclone Structure

A mature tropical cyclone typically consists of a warm core vortical circulation, cyclonic in the lower and anticyclonic in upper troposphere, with a core of intense winds and precipitation. The vortical perturbation of the winds upon the mean environment may extend outward well over 1000 km from the storm center as will be shown later. At the core there is typically a 5-50 km radius eye of warm, calm winds and

little deep convection surrounded by an eyewall cloud about 10-20 km thick (Shea & Gray, 1973) which exhibits extremely strong cyclonic wind flow (V_θ > 30 m/sec) and intense convection. Beyond the eyewall cloud the cyclonic winds gradually diminish with radius, and active convection is confined primarily to intense cyclonically curving squall lines known as spiral or feeder bands. Just outward from these strong convective areas there is usually a relatively clear or "moat" area with little or no intense convection. Beyond the moat ($r \geq 6^o$) convection approaches mean tropical conditions although the winds are obviously influenced by the storm. A dense cirrus shield typically covers the inner 0-4° radius or so.

A schematic diagram of an idealized mature tropical cyclone is shown in Fig. 1.1. Individual storms may be quite asymmetrical, and they vary enormously in size. Therefore, the distance scale in Fig. 1.1 is only an approximation. Since storm data is composited on a grid with fixed radial spacing, the composited radial bands of this study will only approximately correspond to the typical typhoon regimes shown.

1.2 Compositing Philosophy

Tropical cyclones spend most of their lifetimes over the warm tropical oceans from which they are always spawned. Traditional data sources are very sparse in such regions, and daily tropical weather analyses are notoriously unreliable. The severe winds found in tropical cyclones further reduce the availability of such data. On the infrequent occasions when a storm moves into a relatively dense land observation network, it is usually in an atypical decaying stage. The author does not believe that it is possible to obtain enough rawinsonde data

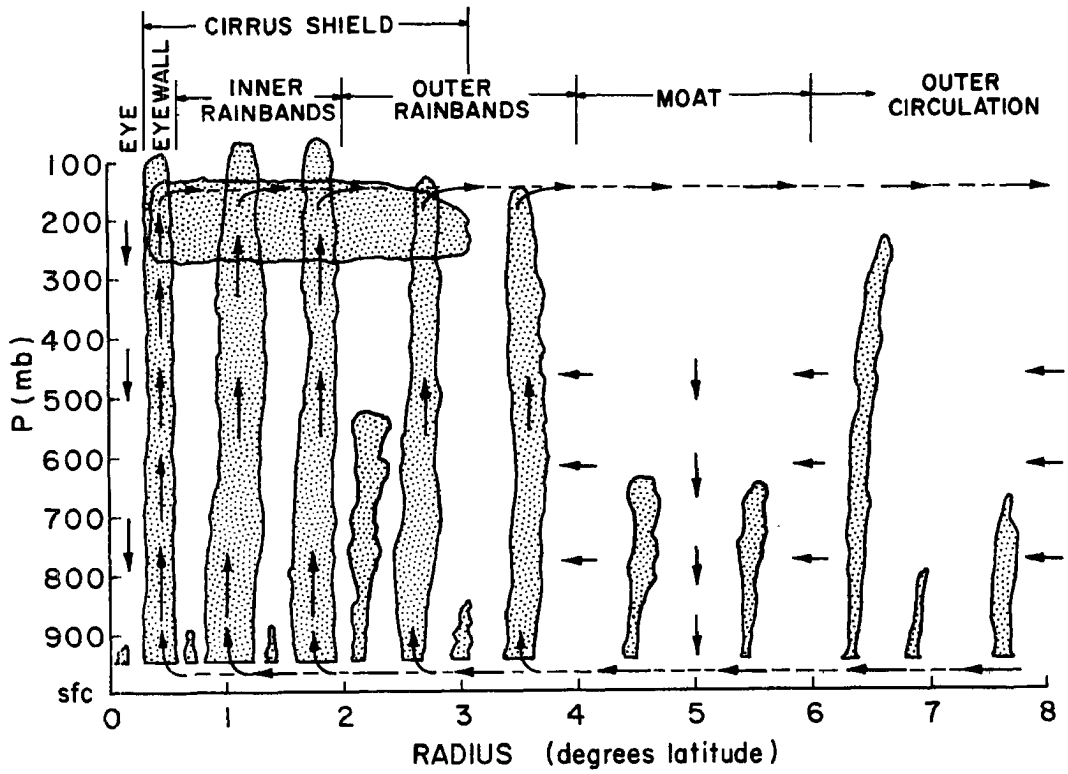

Fig. 1.1. Schematic view of typical tropical cyclone. Arrows denote the mean circulation.

or surface observations around any individual storm at one time period to permit quantitative analysis of storm structure, dynamics or energetics. High resolution satellite data is capable of achieving the necessary data density, but the number of parameters which can be measured accurately is inadequate at this time. In addition, vertical resolution is limited by the dense cirrus shield which covers most of the active convective area.

Aircraft data has provided the best information concerning the activities in the intense central core regions of tropical cyclones. There are a number of case studies of individual storms based on Northwest Atlantic hurricane flight data (Riehl & Malkus, 1961; Miller, 1962; Gray, 1962, 1967; LaSeur & Hawkins, 1963; Sheets, 1967a, 1967b, 1968; Hawkins

& Rubsam, 1968; Hawkins & Imbembo, 1976) and also statistical treatments of the flight data (Shea & Gray, 1973; Gray & Shea, 1973). However, logistical considerations have limited the ability of aircraft to provide information concerning the outer convective regions of the storm and its broader scale environment. Aircraft data also has been limited to a few flight levels per storm time period due to the usually low number of available aircraft, maximum ceilings of 200 mb or less, and dangerous low level flight conditions. These latter two restrictions are particularly important since the present study shows that the maximum inflow and outflow from Northwest Pacific typhoons usually occur near cloud base and 150 mb respectively.

None of the above data sources can produce an accurate vertical profile of the radial wind pattern around a single storm. Without such a profile it is impossible to compute meaningful budgets of energy, water vapor, momentum, vorticity, etc. In addition, vertical profiles of the other dynamic and thermodynamic variables cannot be determined fully over the mesoscale storm area. It is necessary to composite very large amounts of data from many similar storms at many time periods to obtain meaningful quantitative measurements of all of the useful parameters over a large area with a sufficiently high data density.

Although the extreme variabilities and individual asymmetries of tropical cyclones are well known, the author believes that the natures of the basic dynamic and energetic processes which govern these storms are largely invariant. Any compositing system smoothes out many of the individual characteristics of single storms, but a great deal of information concerning asymmetrical or "eddy" storm qualities can be deduced by use of proper data handling techniques. The methods used in this study are discussed below. Storms are so variable at individual time

periods that to form a general physical picture of their nature, it is often desirable to smooth out individual day variability.

Individual case studies of tropical storms have provided much valuable information concerning certain aspects of a few storms. Nevertheless, it appears that careful compositing of very large amounts of data around similar types of storms offers the best hope of furthering the existing knowledge of tropical cyclone structure, dynamics and energetics. Improvement of existing knowledge in these areas is badly needed to provide better baseline data for the many numerical tropical cyclone models now in use or being developed and to aid the development of new forecasting and modification techniques.

1.3 Data Set

This study utilizes ten years (1961-1970) of N.W. Pacific rawinsonde data to provide high density data coverage around composite tropical cyclones. About 18,000 soundings from the 30 stations shown in Fig. 1.2 are processed and used as the basis for this study. A similarly sized data sample for the same stations and 10 year period was composited around intensifying and non-intensifying tropical cloud clusters by Zehr (1976). All of the rawinsonde data are taken from daily Northern Hemisphere Data Tabulations (NHDT) tapes from the Asheville records center and the National Center for Atmospheric Research (NCAR) and from Japanese and East Asian upper air soundings. These latter soundings were card punched by the U.S. Navy for this project.

Rawinsonde data are used to analyze the storm from 2-14^{o} radius. Data are assumed accurate from 1-15^{o} radius for winds and from 0.7^{o}-15^{o} for thermodynamic variables. A combination of rawinsonde and

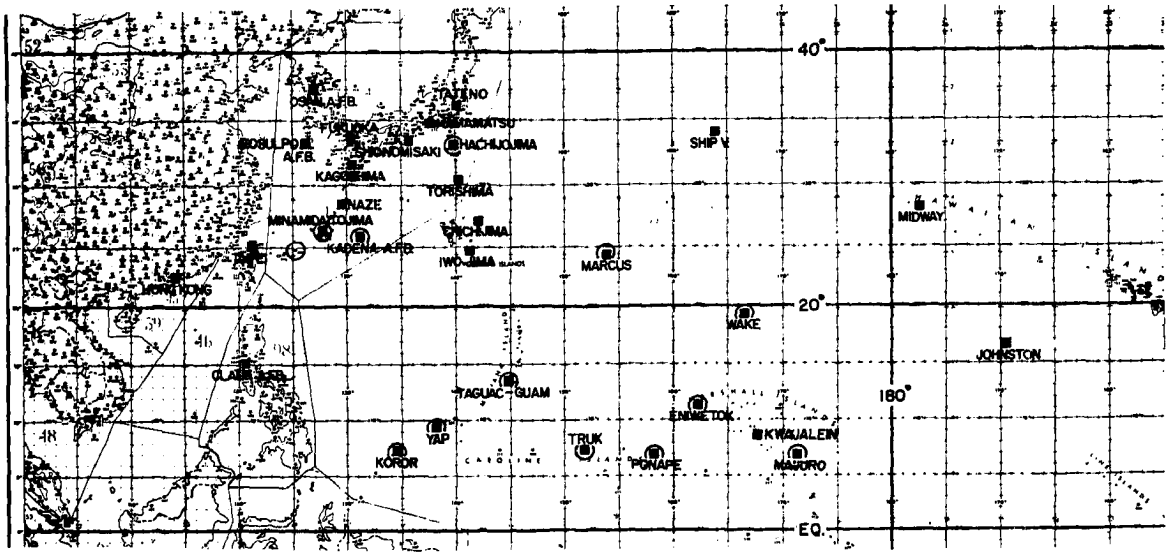

Fig. 1.2. Northwest Pacific rawinsonde data network. Rainfall data from circled stations is used in Chapters 4 and 5.

hurricane flight data (Shea & Gray, 1973; Gray & Shea, 1973) are used to analyze the inner spiral bands, eye and eyewall regions ($0\text{-}2^{o}$).

Satellite photographs and the Guam Fleet Weather Central Joint Typhoon Warning Center (JTWC) reports are used to locate storm circulation centers for gridding. A detailed study of typhoon cloud populations using high resolution Air Force DMSP APT pictures also is being performed at CSU by Major Charles Arnold (1977). Several early results from this study are used in the analysis of the typhoon energy budgets. Up to 21 years of hourly rainfall data from nine small N.W. Pacific island stations and 13 years of 12-hourly rainfall data from 4 small Japanese

islands are used in the water budget analysis. Rainfall stations are circled on Fig. 1.2.

1.4 Compositing Technique

Compositing is performed on a 15^{o} latitude radius cylindrical grid extending from sea level to 50 mb. The storm circulation center is located at each time period using the JTWC reports, and the grid is positioned with the storm at grid center of the lowest level. The horizontal grid is shown in Fig. 1.3. Whenever available rawinsonde soundings fall on the grid at a given time period for a given storm, each sounding is located relative to the storm center in cylindrical coordinates. All of the parameters to be composited, whether directly measured or computed from the directly measured parameters, are determined at the observation station locations at 19 vertical pressure levels. Certain corrections in the relative positions of the balloon and storm center are made. These corrections are discussed later.

The cylindrical grid consists of eight octants of 45^{o} azimuthal extent and eight radial bands extending from $0\text{-}1^{o}$, $1\text{-}3^{o}$, $3\text{-}5^{o}$, $5\text{-}7^{o}$, $7\text{-}9^{o}$, $9\text{-}11^{o}$, $11\text{-}13^{o}$, $13\text{-}15^{o}$. The 64 grid boxes are not equally sized. The geographical alignment of the grid varies with the coordinate system used (discussed below). After all parameters have been either measured or computed for each sounding, the value of each parameter is assigned to a point at the center of the grid box in which the sounding falls. All soundings falling in that grid space for the particular group of storms and time periods being analyzed are composited.

Parameters Composited. The following parameters are measured or computed at each level for each sounding:

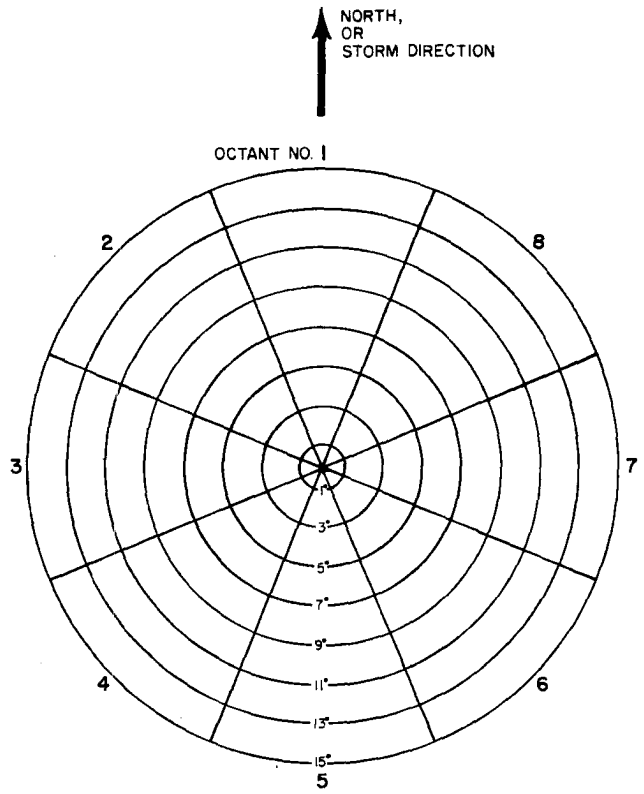

Fig. 1.3. Compositing grid. Arrow points north in NAT and MOT coordinate systems and in direction of storm motion in ROT and MOTROT systems. Coordinate systems are defined in section 1.4.

Dynamic Parameters	Thermodynamic Parameters
u (zonal wind)	T (temperature
v (meridional wind)	T_v (virtual temperature)
V_r (radial wind)	z (height)
V_θ (tangential wind)	q (specific humidity)
V (total wind speed)	RH (relative humidity)
V^2 (total wind speed squared)	θ (potential temperature)
$V_\theta \cdot r$ (relative angular momentum)	θ_v (virtual potential temperature)
$V_r \cdot f$ (radial transport of f)	θ_e (equivalent potential temperature)
$V_r \cdot s$ (radial transport of s)	θ_{es} (saturated equivalent temperature
$V_r \cdot h$ (radial transport of h)	s (static energy)

Dynamic Parameters (cont'd)

$V_r \cdot q$ (radial transport of q)

$V_r \cdot V^2$ (radial transport of V^2)

Thermodynamic Parameters (cont'd)

h (moist static energy)

Coordinate Systems. All data are composited in four separate cylindrical coordinate systems:

1) Stationary, aligned geographically with octant 1 pointing north (natural or NAT system)

2) Geographical coordinate system with the cyclone motion subtracted out of all the winds (motion or MOT system)

3) Stationary, octant no. 1 aligned with the direction in which the storm is moving (rotated or ROT system)

4) Octant No. 1 aligned with the direction in which the storm is moving with the cyclone motion subtracted out of all winds (motion rotated or MOTROT system).

Stratifications. The data set is sufficiently large to allow compositing of various subsets. Data may be grouped according to any characteristics observed in individual storms such as location, season, intensity, motion, or intensity tendency. By comparing the composites of different types of storms it is possible to quantitatively analyze the persistent differences between the groups. It is also possible to remove obviously atypical storms or time periods from a storm group to improve the quality of the data set. Although the greater part of this study is concerned with mean steady state typhoon data, several stratification analyses have been accomplished and are discussed in appropriate sections. Most of the storm structure information is taken from the mean steady state typhoon data set. This sample contains 7784 soundings around typhoons with central pressures $\leq$980 mb. Storms whose centers are north of 30^{o} latitude have been excluded. Examination

of the individual storms in this data set shows no significant bias toward deepening or filling storms. Therefore, steady state is assumed.

Balloon and Storm Position Corrections. The relative positions of the storm and the balloon change due to their respective motions during the balloon's ascent time. These motions are estimated from the data, and the following corrections are made.

A constant balloon ascent rate of 5 m/sec is assumed, and the ascent time to each pressure level is estimated. A storm speed vector is estimated for each storm time period from the storm direction and velocity at the time nearest balloon release. The storm's position is moved backward along its motion vector a distance equal to 30 minutes travel to account for early balloon release time. This is the estimated storm position for the surface observations. The storm is then moved along its storm motion vector according to the assumed ascent time to each level.

The balloon position is adjusted by using the mean ascent times and the observed winds at each level. As the balloon moves through a layer, the mean u and v wind components are estimated. The products of these winds and the ascent time give the balloon position correction for each level. The balloon and storm motion corrections have negligible influences at radii greater than $\sim 4^{\circ}$.

Computation of Eddy Fluxes. Budget studies require the accurate determination of horizontal fluxes of the quantities of interest. Historically, hurricane budget studies have dealt only with mean, large scale horizontal transports. In such studies mean 2-dimensional radial wind profiles are assumed, and fluxes are computed by determining the products of the mean radial winds and the observed quantities at

each level and then integrating vertically. A few studies have tried to estimate horizontal eddy fluxes by computing these fluxes as residuals in conservation budget equations.

The author believes that both of the above methods have serious shortcomings. The use of mean fluxes alone neglects the striking asymmetries observed in most storms, especially in the important outflow and boundary layers. In the mid-levels a weak mean radial wind component may be the result of strong but nearly equal observed inflow and outflow winds. Due to the extremely strong gradients of temperature, pressure, moisture, vorticity, etc. found in tropical cyclones, the resulting advective or eddy terms can be quite large. It will be shown that the eddy transports often play important roles in the dynamics and energetics of tropical cyclones.

Attempting to solve for horizontal eddy transports as a residual in a conservation budget equation using real data is rarely successful. Parameterization of surface to air fluxes of heat, momentum, moisture, etc. is difficult due to the uncertain nature of the surface winds and the state of the sea surface in the critical inner regions.

In this study horizontal eddy fluxes are estimated by compositing individual fluxes of quantities and comparing them to mean fluxes. The radial winds are initially composited and mass balanced from the surface to 100 mb by adding a small constant correction factor (ΔV_r) to each individual radial wind value in a given radial band. Changes in mass of the volume within the radial band are neglected. For each sounding the product of the corrected V_r and the quantity being analyzed is computed at each level. Such products for all of the soundings in an octant are then composited as before, giving a mean transport value for each octant

at each level, $\overline{V_r Q}$, where the bar denotes time and space averaging of the $V_r \cdot Q$ products. By subtracting the product of the mean $\overline{V_r}$ and the mean quantity ($\overline{Q}$) one can achieve a good estimate of horizontal eddy transport:

$$\overline{V_r' Q'} \approx \overline{V_r \cdot Q} - \overline{V_r} \cdot \overline{Q}$$

This technique is used in all of the budget studies in this paper.

2. THERMODYNAMIC FIELDS

Tropical cyclones cause impressive perturbations of the tropical temperature, height and humidity fields. The structure of the mean steady state typhoon with respect to these variables is discussed below. Soundings for the various regions from the center to 14^{o} radius are also presented.

2.1 Temperature

Tropical cyclones are warm core vortices throughout the troposphere. Figure 2.1 shows the mean 2-dimensional temperature anomaly (defined as $T - \overline{T}_{r=14^{o}}$), and plan views of temperature at 950, 500 and 300 mb are shown in Figs. 2.2 - 2.4. Boundary layer temperatures are relatively constant with radius despite decreasing pressure towards the center. This phenomenon, reported by Byers (1944), implies a strong sensible heat flux into the boundary layer from the sea and/or from above as discussed in Chapter 6. There is strong baroclinicity northwest of the storm probably reflecting the cold water around southern Japan. The maximum temperature anomaly occurs at about 250 mb. The innermost data shown are for $r = 0.7^{o}$. Flight data (Shea & Gray, 1973; Gray & Shea, 1973) shows that mean temperatures in the eye in the middle and upper troposphere may be $7^{o}C$ or more warmer than the corresponding temperatures at 0.7^{o} radius. Therefore, the mean maximum temperature anomaly may be $15^{o}C$ or more. Case studies such as Simpson (1952), Simpson and Starrett (1955) and Hawkins and Imbembo (1976) have verified temperature anomalies of this magnitude. The 500 mb and 300 mb plan views show substantial temperature gradients northwest of the storm. This probably results from a mean upper level westerly trough which also can be detected in the height fields.

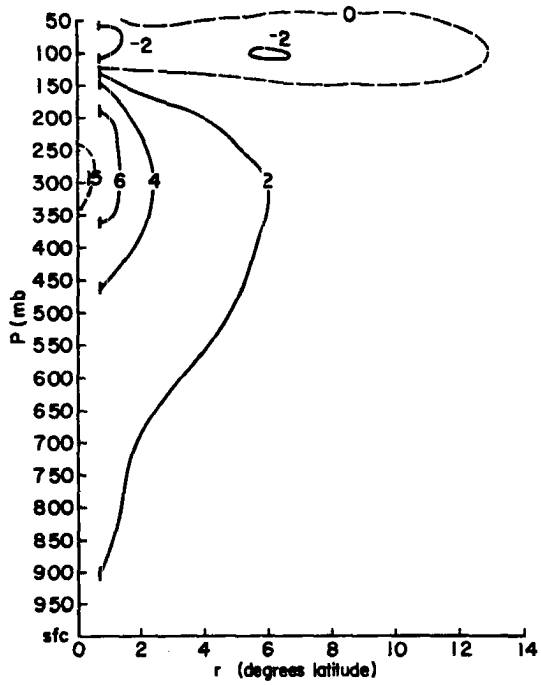

Fig. 2.1. Temperature anomaly ($T - T_{at\ 14^o}$) for mean steady state typhoon. Units ^oC.

Temperature gradients are small in the lower stratosphere with the storm displaying a weak cold core at those levels, probably the result of Cb overshoot cooling. This implies that height gradients in that region are very weak imposing a sort of dynamic lid on the storm circulation. This does not mean, however, that stratospheric/tropospheric interaction is insignificant. In the regions of intense convective activity, overshooting Cb tops appear to cause a downward flux of heat across the 100 mb surface. This is discussed in Chapter 6.

2.2 Height Field

The observed warm core temperature anomaly implies a low pressure system with the strongest height gradients near the surface. A 2-dimensional cross-section of D values is shown in Fig. 2.5. The height

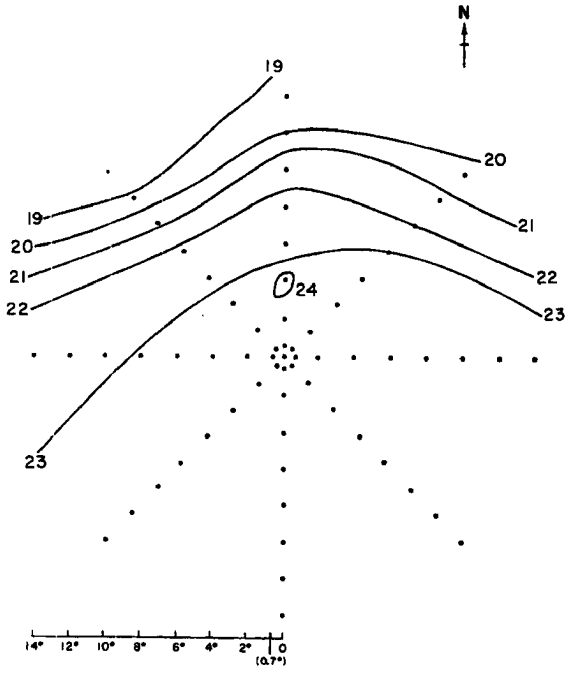

Fig. 2.2. Plan view of temperature in °C at 950 mb, in NAT coordinate system.

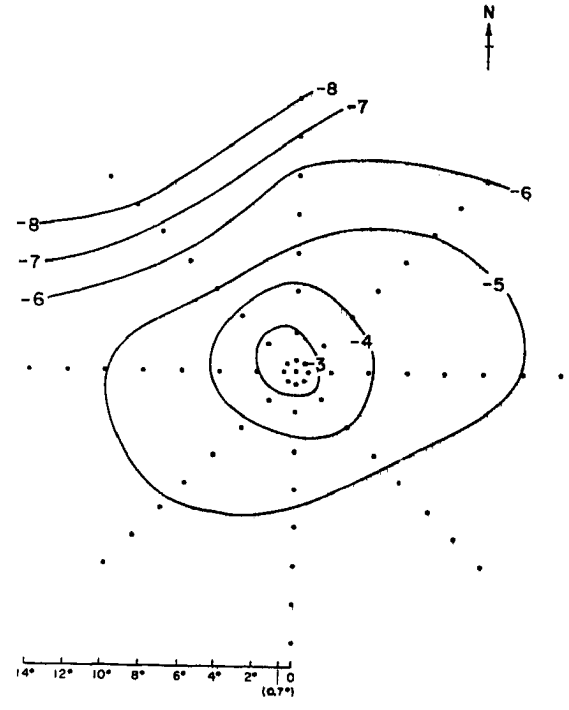

Fig. 2.3. Same as Fig. 2.2 for 500 mb.

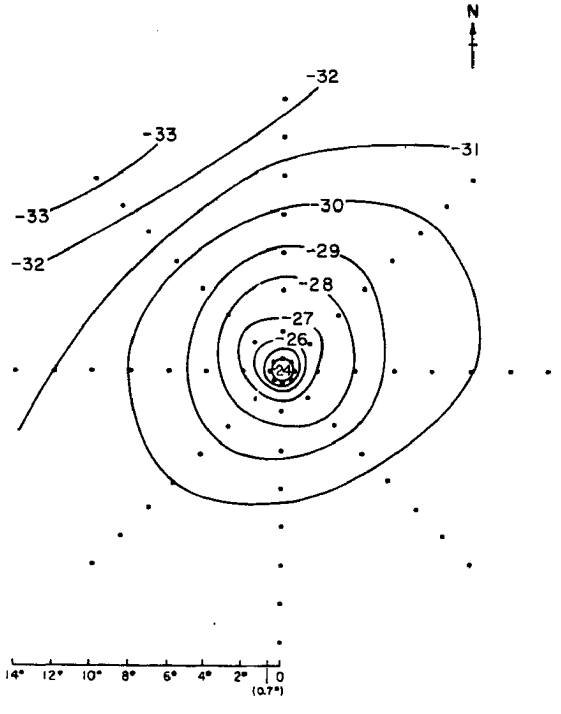

Fig. 2.4. Same as Fig. 2.2 for 300 mb.

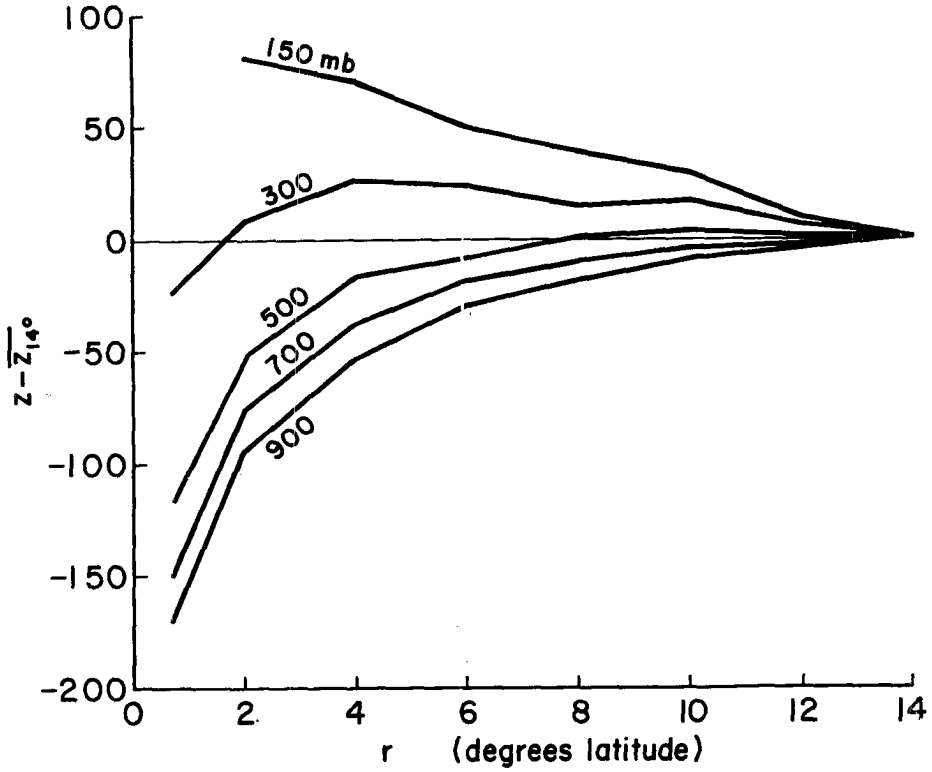

Fig. 2.5. D-values ($Z - \bar{Z}_{14^\circ}$) in meters for mean steady state typhoon at selected levels.

gradients increase with decreasing radius reaching a maximum at the radius of maximum winds (Shea & Gray, 1973). Temperature gradients are also maximum at this location. As expected, the height gradients decrease with altitude in the lower and middle troposphere. At 300 mb the gradients are almost zero, while above that level heights increase with decreasing radius. At 50 mb the gradients are near zero verifying the dynamic lid concept (not shown).

The temperature perturbations of Figs. 2.2-2.4 are nearly symmetrical except for the area northwest of the storm beyond 8° radius. This implies that the height perturbation of a typhoon upon its environment is also roughly symmetrical. The height fields themselves, however, are asymmetrical. The strongest gradients occur to the right

of the storm (looking downstream in the direction toward which the storm is moving). This is a natural result of the imposition of a symmetrical height perturbation upon a sloping environmental height field as is shown in more detail in Chapter 3. A more complete study of storm height and wind asymmetries and their relationships to storm motion using this data set is presented in a report by George (1975).

Plan view heights at 900 mb, 500 mb, and 150 mb are shown in Figs. 2.6 - 2.8. The low level (900 mb) height field is nearly axisymmetric with closed height contours extending to about 8^{o} radius. At the two higher levels, however, there is evidence of a mean trough to the northwest. Closed contours are not found as far from the center of the storm as they are at lower levels. The strong height gradient to the north and northwest of the storm at 150 mb is indicative of the mean outflow jet towards the northeast.

2.3 Relative Humidity

The strong convective regions of tropical cyclones ($0-4^{o}$) have much higher mean relative humidities than the surrounding tropical atmosphere. Figure 2.9 shows a mean 2-dimensional cross section of the 12Z relative humidities (about 2100-2200 local time). Nighttime humidities are used to avoid the instrument errors in humidity measurements caused by solar heating of the sensors which were common during the data period being used (Ruprecht, 1975). It is assumed that true diurnal variations in relative humidity are small. Diurnal variations of tropical cyclones are discussed later.

The most striking feature of the humidity profile is the extremely high humidity of the core region ($0-1^{o}$). It is assumed that few, if

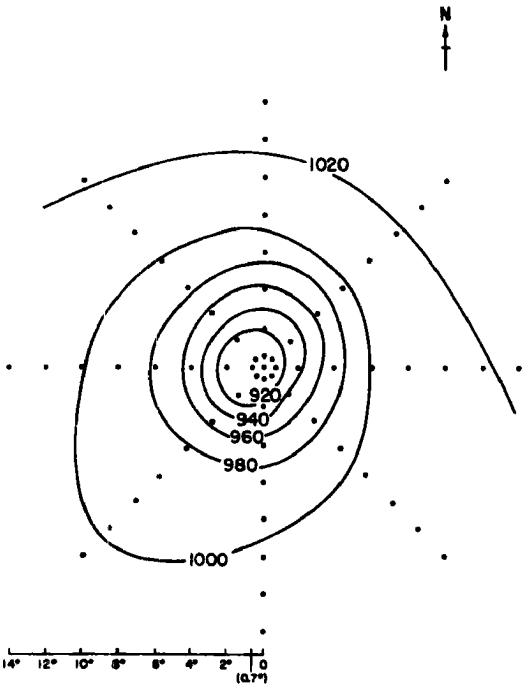

Fig. 2.6. Plan view of 900 mb heights in meters. NAT coordinate system.

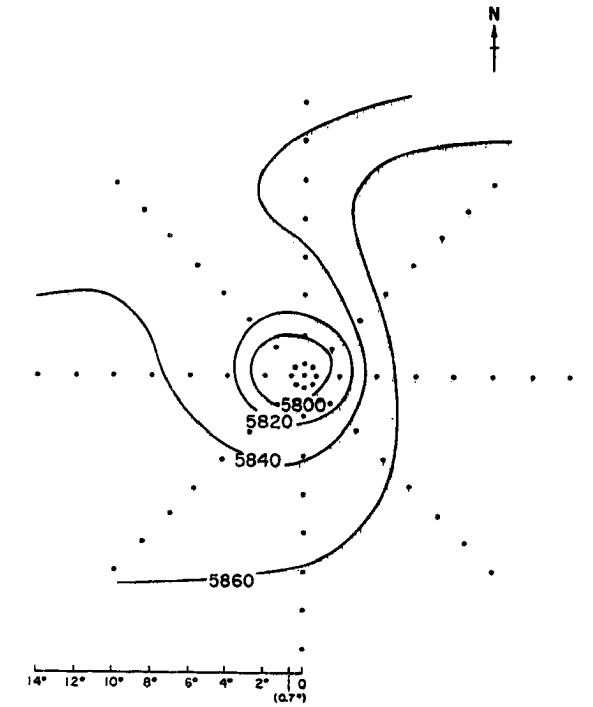

Fig. 2.7. Same as Fig. 2.6 for 500 mb.

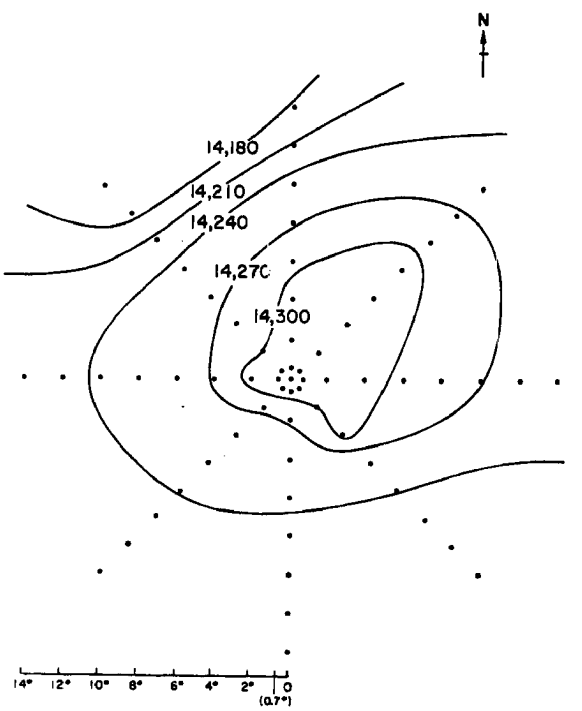

Fig. 2.8. Same as Fig. 2.6 for 150 mb.

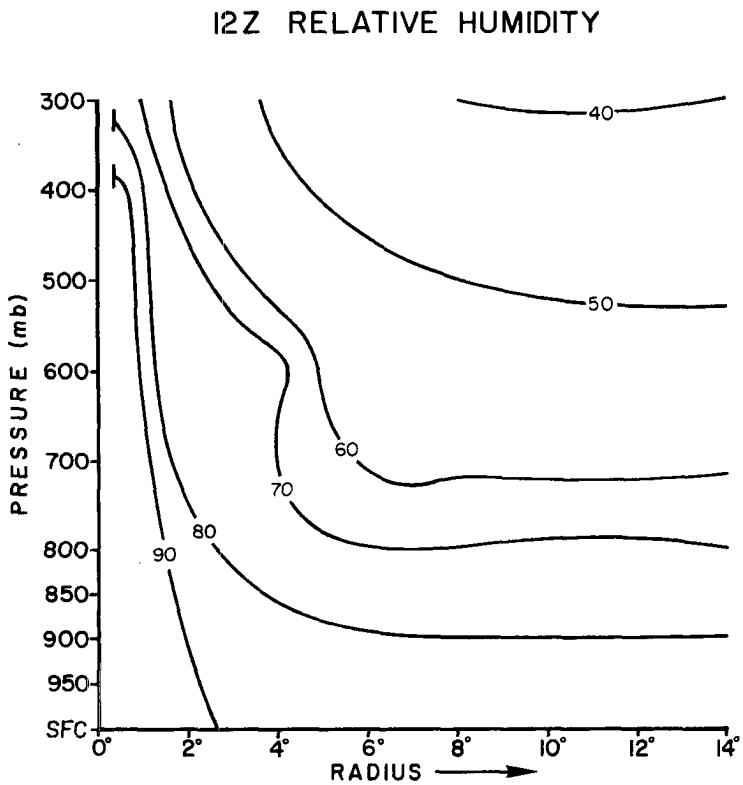

Fig. 2.9. Relative humidities of mean steady state typhoon at 12Z (∿ 2200 local time).

any, of the rawinsondes in that region ascended in rainbands or the eyewall. Nevertheless, mean humidities exceed 90% up through 400 mb. This implies that entrainment drying does not greatly hamper cumulonimbus convection in this inner region. The positive humidity anomaly extends outward through the active convective region (0-4°). The small positive anomaly at 6° may be due to the occurrence of a few very large storms in the data set rather than to above average humidities in the clear moat area which surrounds most storms.

Figures 2.10 and 2.11 show plan views of 12Z relative humidity at 900 mb and 500 mb. At the lower level the humidity field is virtually uniform except for slightly drier air to the northwest and the exceptionally high humidities in the core region. At 500 mb the central core is

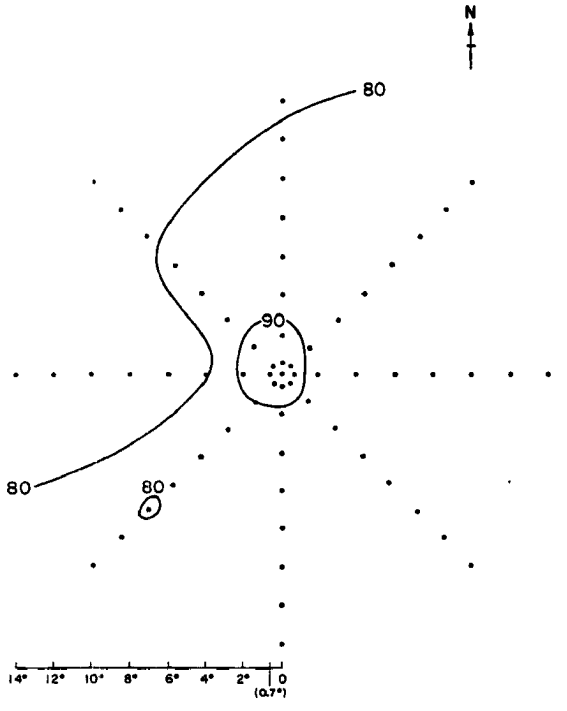

Fig. 2.10. Plan view of relative humidity at 900 mb, in NAT coordinate system.

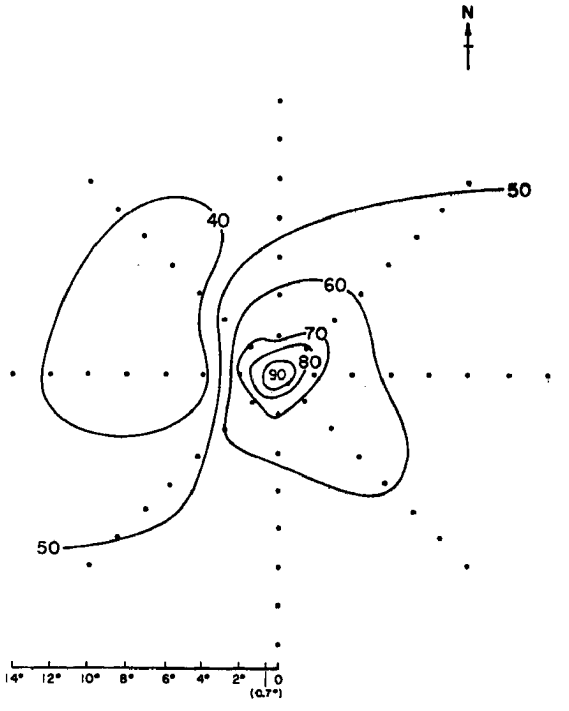

Fig. 2.11. Same as Fig. 2.10 for 500 mb.

still very humid, but the humidity drops off rapidly with radius. A minimum (less than 40%) is observed west and northwest of the storm center from 6-12° radius. This is probably indicative of a mean subsidence region. A clear region in the direction of storm motion is often observed in satellite photographs.

2.4 Soundings

Mean soundings for the steady state typhoon and its environment are shown in Table 2.1. Temperatures in the eye are based on temperature gradients from Shea & Gray, (1973) applied to the values at r = 0.7° observed in this study. Humidities in the eye are estimated from Jordan (1961) and Gray & Shea (1973). From 0.7° outward the

TABLE 2.1

Mean Soundings T(^{o}C) q ($\frac{g}{kg}$)

	Jordan (1958)			NW Pacific (Gray et al., 1975)													
				Cluster (12Z)		Clear Area		eye			$r = 0.7^{o}$			$r = 2^{o}$		
	T	q	RH	T	RH	T	RH	T	q	RH	T	q	RH	T	q	RH
sfc	26.3	18.2	84	26.1	88	26.5	85	--	--	--	24.5	19.4	95	25.7	19.4	90
950	23.0	15.3	81	23.2	87	23.7	86	24.8	19.2	90	23.8	18.4	94	23.7	17.3	89
900	19.8	13.0	79	20.7	82	20.7	82	22.1	17.1	89	21.1	16.8	94	20.8	15.7	89
850	17.3	11.0	74	18.2	78	18.1	76	20.3	15.3	88	18.8	15.3	94	18.4	13.8	87
800	14.6	8.4	68	15.4	77	15.4	68	18.7	13.8	86	16.7	14.0	93	16.1	12.1	83
700	8.6	5.8	57	9.4	75	9.9	54	14.3	10.4	80	11.3	11.2	92	10.7	9.1	78
600	1.4	3.6	50	2.0	80	2.3	56	10.0	7.8	64	5.0	8.2	89	4.1	6.5	76
500	-6.9	2.1	45	-5.7	77	-5.8	47	2.7	4.7	50	-2.3	6.0	91	-3.2	4.3	70
400	-17.7			-15.8	72	-16.0	31	-7.2	2.8	50	-11.2	3.5	85	-12.8	2.2	60
300	-33.2			-30.9		-31.3		-21.0	1.2	50	-24.0	1.5	77	-27.0	0.8	53
250	-43.3			-41.3		-41.4		-31.3	.6	50	-33.3			-36.4		
200	-55.2			-54.3		-53.5		-44.5			-46.0			-48.7		
150	-67.6			-69.1		-67.8		-59.8			-60.8			-63.6		
100	-73.5			-77.5		-78.9		-77.1			-77.1			-75.5		
80	-69.8			-72.9		-72.9								-73.6		
70	----													-67.7		
60	-63.9													-64.9		
50	-60.6													-60.9		

TABLE 2.1 (cont'd)

	r = 4°			r = 6°			r = 8°			r = 10°			r = 12°		
	T	q	RH	T	q	RH	T	q	RH	T	q	RH	T	q	RH
sfc	26.1	18.8	85	25.7	17.9	83	25.7	17.7	82	25.5	17.4	82	25.2	17.1	82
950	23.7	16.1	84	23.1	15.3	80	23.2	15.0	78	22.6	14.6	78	22.2	14.1	79
900	20.9	14.5	83	20.2	13.5	80	20.1	13.1	78	19.8	12.8	77	19.4	12.6	78
850	18.4	12.5	79	17.8	11.4	75	17.6	11.1	74	17.3	10.9	73	16.8	10.7	74
800	16.0	10.7	74	15.5	9.5	68	15.3	9.3	67	14.9	9.0	67	14.4	8.9	68
700	10.6	7.6	66	10.2	6.3	57	10.0	6.1	55	9.6	5.9	54	9.2	5.8	55
600	3.7	5.3	64	3.3	4.3	54	3.1	4.0	51	2.7	3.9	50	2.2	3.9	51
500	-3.9	3.3	58	-4.7	2.7	50	-5.1	2.4	46	-5.4	2.3	45	-5.9	2.2	44
400	-14.0	1.7	50	-14.9	1.3	43	-15.4	1.2	40	-15.8	1.1	40	-16.2	1.1	40
300	-28.2	0.6	46	-29.3	0.5	39	-29.9	0.4	35	-30.4	0.4	35	-30.9	0.4	36
250	-38.0			-39.1			-39.6			-40.1			-40.5		
200	-50.2			-51.0			-51.5			-51.8			-52.0		
150	-64.6			-65.0			-65.1			-65.1			-65.1		
100	-76.4			-76.4			-76.2			-75.7			-75.3		
80	-73.4			-74.1			-73.6			-73.1			-72.5		
70	-68.7			-68.6			-68.7			-68.5			-68.3		
60	-65.2			-65.4			-65.3			-65.1			-64.8		
50	-61.1			-61.8			-61.2			-61.3			-61.1		

temperatures and humidities shown are from the composited rawinsonde data. Also shown are Jordan's (1958) mean hurricane season sounding for the West Indies and the summertime 12Z West Pacific cloud cluster and clear region soundings as given by Gray, et al. (1975).

Vertical profiles of h and h* (h saturated) for each region are shown in Figs. 2.12 - 2.19. The usual 600-700 mb minimum in h is observed at all radii. The shapes of the h profiles are similar from 4-12° although the values are progressively higher with decreasing radius. The same is true for the h* profiles outside the eye. At 2° the increased temperatures and humidities in the middle and upper levels flatten out the curves somewhat. The 0.7° sounding is typical of the intense convective region just beyond the eyewall cloud. The h and h* profiles for this region are nearly vertical.

The potential buoyancy or conditional instability of an ascending parcel is approximately equal to h (parcel) minus h* (environment). Tropical clouds are usually observed to have nearly the same temperatures as the environment at cloud base (∿950 mb). In the energy budget analysis of Chapter 6, the clouds are assumed to be saturated at the temperature of the environment at 950 mb. The undilute ascent paths for parcels ascending from saturation and no temperature perturbation at 950 mb are shown by the vertical dashed lines. For the eye the line is drawn assuming that clouds in that region have the same values of h at 950 mb as clouds at r = 0.7°. The area between this line and the mean h* profile in each region is approximately equal to the total integrated potential buoyancy of the parcel. This area is a measure of the maximum possible generation of kinetic energy for the parcel ascent. It is interesting to note that this area is smaller for the most active convective region sounding (0.7°) than for

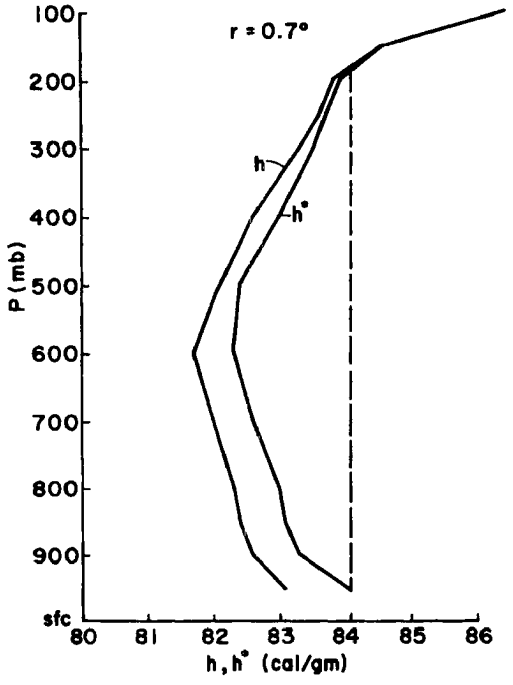

Fig. 2.12. Moist static energy (h) and saturated moist static energy (h^*) at r=0.7°. Vertical dashed line is path of undilute saturated ascent from 950 mb.

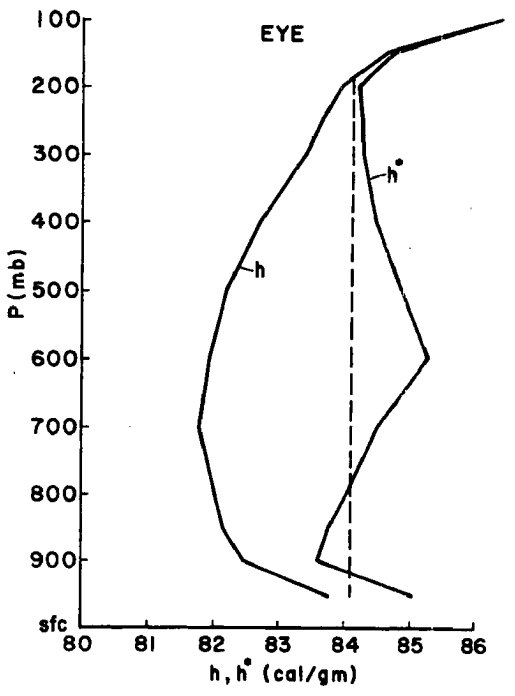

Fig. 2.13. Same as Fig. 2.12 for eye.

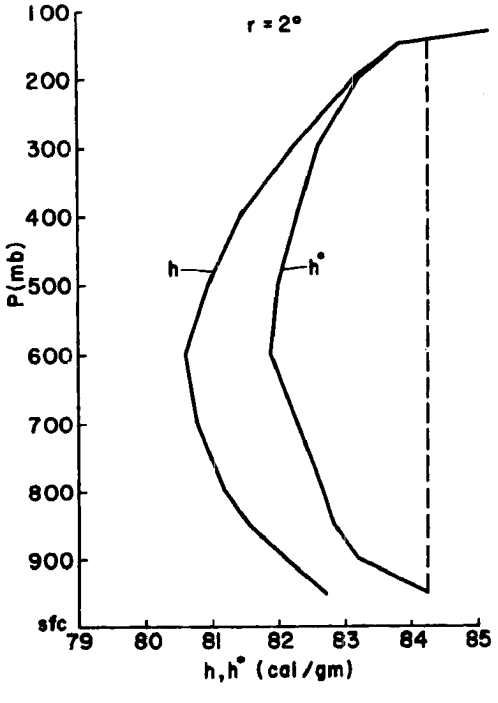

Fig. 2.14. Same as Fig. 2.12 for r=2°.

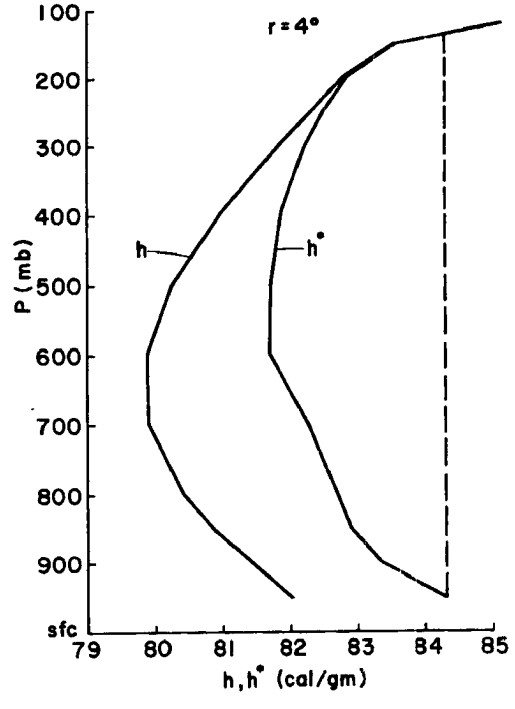

Fig. 2.15. Same as Fig. 2.12 for r=4°.

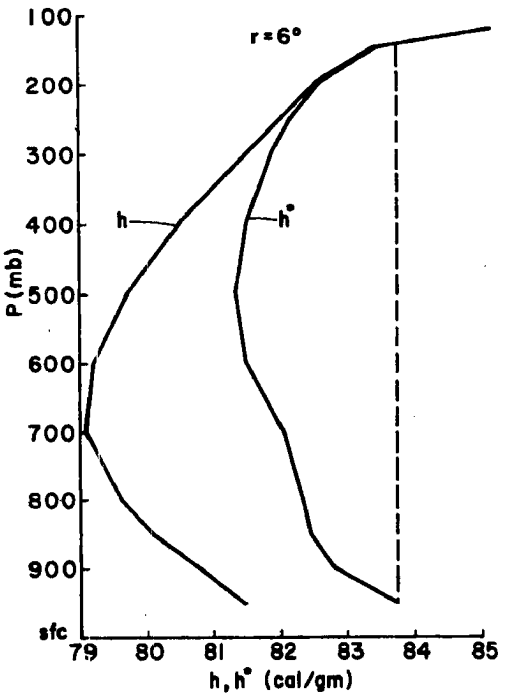

Fig. 2.16. Same as Fig. 2.12 for r=6°.

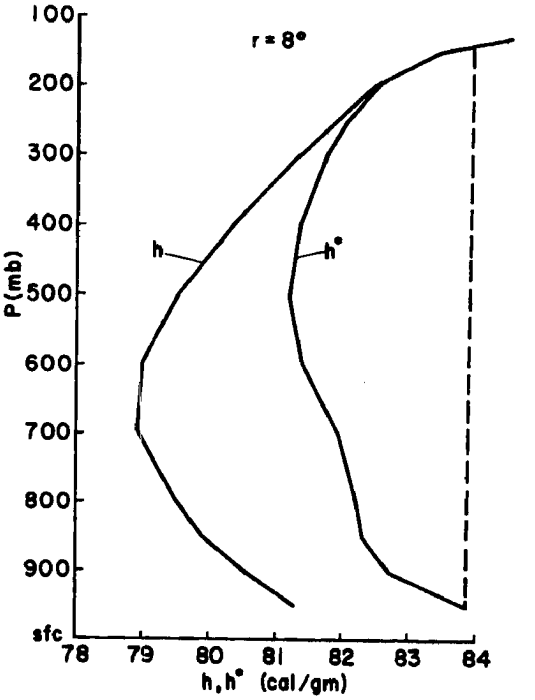

Fig. 2.17. Same as Fig. 2.12 for r=8°.

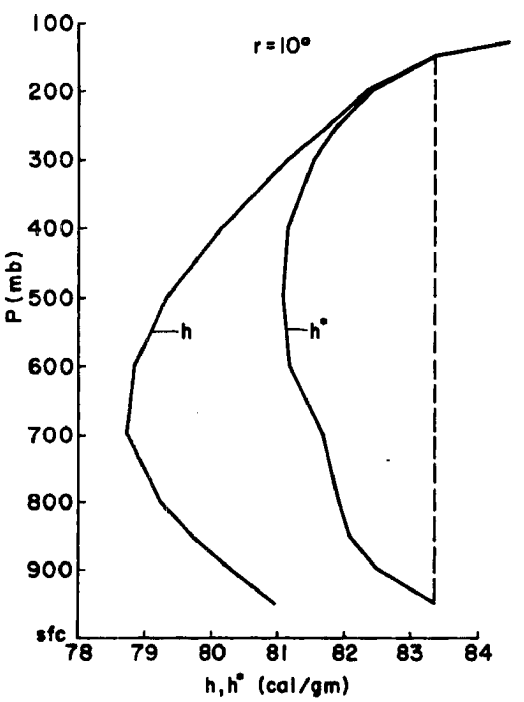

Fig. 2.18. Same as Fig. 2.12 for r=10°.

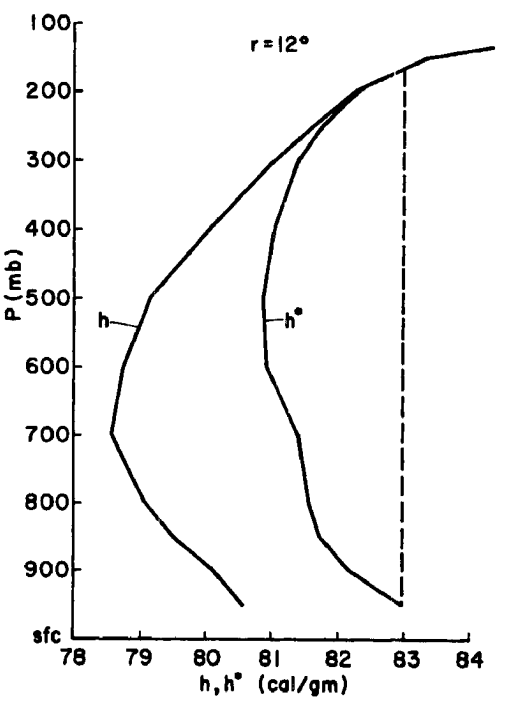

Fig. 2.19. Same as Fig. 2.12 for r=12°.

the outer radii soundings although there is still some mean conditional instability. The soundings indicate that there is no positive correlation between the amount of environmental conditional instability and the amount of deep convection. It does not seem likely that small changes in the environmental lapse rates are a controlling influence on the amount or nature of the convection.

The sounding for the eye is somewhat speculative. The h profile is nearly identical to the $r = 0.7^{o}$ profile. The eye, however, is warmer and drier than the air outside the eyewall due to the extreme subsidence there. The eye sounding is stable - only very shallow convection is possible. This seems reasonable since deep convection is never observed in the eye.

3. COMPOSITE WIND FIELDS

Although the mean wind fields of tropical cyclones and their environments have received much attention, only the relatively dominant tangential flow is well documented. Numerous case studies are in the literature, but none of these achieved sufficient data density to allow very accurate determination of the radial winds, divergence, vertical motion, or vorticity fields. Jordan (1952) and Hughes (1952) used composite data to analyze the upper and lower mean wind fields around tropical cyclones respectively. Miller (1958) updated these studies with increased amounts of data. All of these studies were done by hand computation using relatively small data sets. The most extensive of these studies (Miller) involved only 1047 soundings on a 24^{o} x 16^{o} latitude rectangular grid, and most of his data came from only 6 storms. Computational demands limited balloon motion corrections to the inner 2^{o}, and storm motion during the ascent was not corrected. In addition, radial winds were computed from grid square averaged winds rather than for each sounding. The above factors, inherent shortcomings of the precomputer age, cast a degree of doubt on the accuracy of these observed radial wind fields and the calculations derived from these values.

Izawa (1964) performed a computer composite of N.W. Pacific typhoon data. Once again the data set was small - 669 soundings from 12 storms on a 10^{o} radius cylindrical grid. Izawa did not correct for balloon or storm motion during ascent. He concluded that the radial winds and subsequently derived parameters presented in his paper were speculative.

Although the above studies give relatively accurate values of the mean tangential wind fields, none contain the necessary quantities of data or use the compositing techniques required to obtain accurate budget study analyses and vertical motion fields. The relatively small number of storms used prevented stratifications of the data into subsets. For instance, the Miller and Izawa studies included data for storms over land. The author does not wish to detract from the important scientific contributions of the above studies. Rather it is desired to expand the knowledge of the mean tropical cyclone wind structure through the use of advanced computational data handling processes. A comparison of some of the results of this study with those of the Miller and Izawa studies is included at the end of this section.

3.1 Environmental Flow

Tropical cyclones in the N.W. Pacific are embedded in southeasterly flow extending through most of the tropopause. Figure 3.1 shows the mean $\bar{u}$ component of the wind in stationary coordinates for the steady state typhoon. At 2^{o} radius the mean flow is easterly and nearly constant with height up to about 250 mb. In the lower stratosphere strong easterly flow prevails. At $r = 6^{o}$ the mean flow becomes slightly westerly above 700 mb due to the relatively strong middle latitude westerlies to the north of the storm. At greater distances from the center the mean westerly flow becomes still stronger and extends from the tropopause down to 800 mb as shown by the $r = 10^{o}$ curve. The mean $\bar{u}$ component of storm center motion is -2.0 m/s.

The mean $\bar{v}$ component is shown in Fig. 3.2. The storm is embedded in southerly flow at all radii with little vertical shear below about 200 mb. The magnitude of the southerly wind generally decreases with

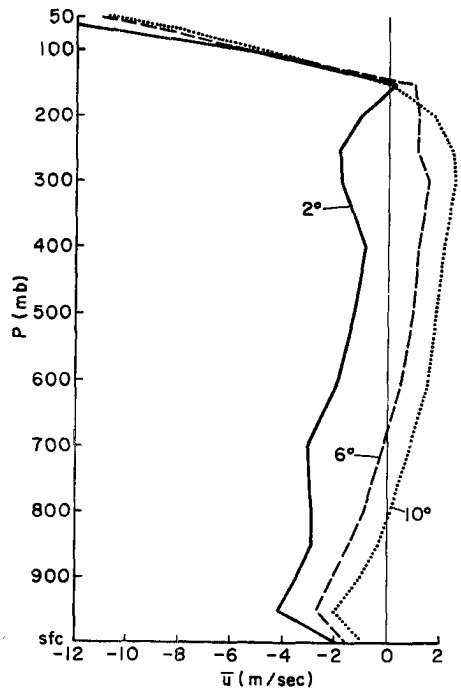

Fig. 3.1. Mean $\bar{u}$ in stationary coordinates at r=2°, 6° and 10° for the mean steady state typhoon.

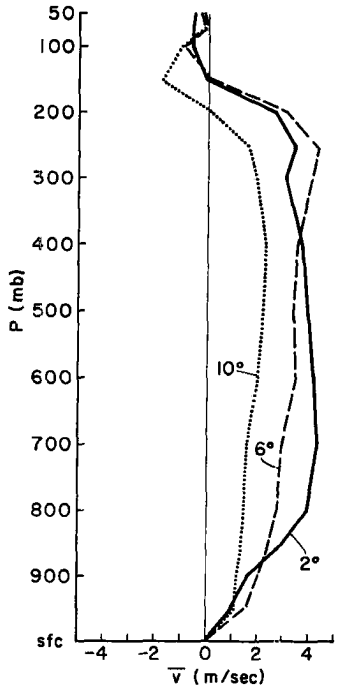

Fig. 3.2. Mean $\bar{v}$ in stationary coordinates at r=2°, 6° and 10° for the mean steady state typhoon.

radius. The mean $\bar{v}$ component of storm center motion is +2.9 m/s. A detailed analysis of the relationships between storm motion and the surrounding flow fields has been discussed in more detail in a report by George (1975).

3.2 Tangential Winds

The most striking feature of tropical cyclone structure is the intense tangential wind field. A broad lower tropospheric cyclone extends outward to 1000 km or more. Cyclonic flow increases in depth and intensity with decreasing radius. A large upper tropospheric anticyclone overlies the cyclone from about 2° radius outward. The anticyclone increases in depth and intensity with increasing radius. Above the tropopause stratospheric easterly flow prevails.

Mean tangential winds (V_θ) have been composited in all four coordinate systems. Figure 3.3 shows a 2-dimensional cross-section of the tangential wind field. There is a cyclonic maximum at 850-900 mb at the effective top of the frictional boundary layer. A strong anticyclonic maximum occurs at 150 mb, the maximum radial outflow level. This upper maximum reflects the approximate conservation of angular momentum of the outflowing air.

Lower tropospheric vertical wind shears are quite weak. In the upper troposphere, however, anticyclonic flow becomes stronger and deeper with increasing radius resulting in a mean tangential shear between 900 mb and 150 mb of about 15-20 m/sec. Cyclonic flow extends throughout the depth of the troposphere only in the inner core (0-2°) region as noted by Riehl (1954). This is probably due to vertical momentum transport by the intense cumulonimbus convection found there (Gray, 1967).

Vertical cross sections and plan views are shown in Figs. 3.4-3.23. No analysis is performed inside 1° radius due to the scarcity of data at inner radii. Figures 3.4 and 3.5 show north-south and east-west cross sections in stationary (NAT) coordinates (see section 1.4 for discussion of coordinate systems). The mean storm center location is 21.7°N, 136.4°E, and the mean velocity is 3.55 m/s toward 326°. Cyclonic flow is stronger to the north than to the south inside about 8° radius, and the anticyclone is stronger to the north at almost all radii reflecting the presence of the middle latitude westerlies. The storm is more symmetrical in the E-W direction. Both the cyclone and anticyclone are stronger to the east. The stronger cyclonic flow to the north and east is indicative of stronger flow to the right of the storm's direction of motion. This is shown in more detail later.

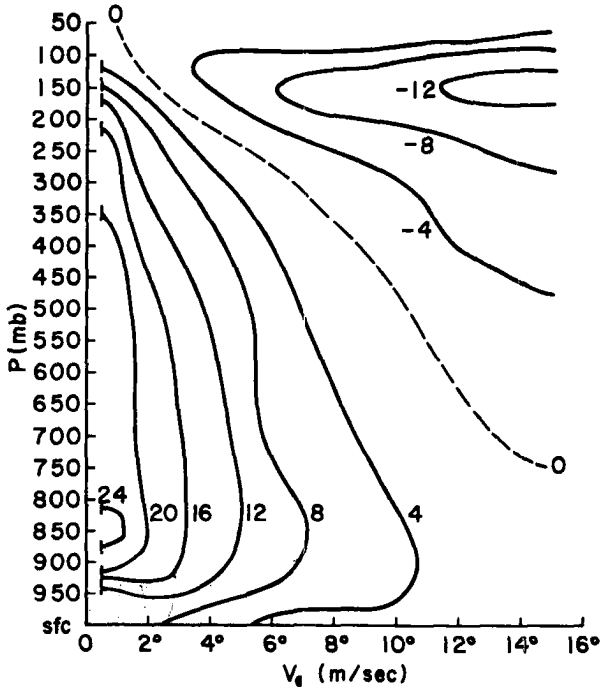

Fig. 3.3. 2-dimensional cross section of V_θ in stationary (NAT) coordinates.

Maximum cyclonic flow occurs at 850-900 mb on all sides. The anticyclonic maximum occurs near 150 mb, but it tends to decrease in height toward the north due to the decrease in the height of the tropopause. The boundary between cyclonic and anticyclonic flow ($V_\theta = 0$) occurs at approximately the same location for all classifications of storms. It is assumed that this shows that the broad scale of circulation of tropical cyclones in the northwest Pacific environment is independent of inner core characteristics.

Figures 3.6-3.8 show front-back and left-right cross sections of V_θ in stationary coordinates where the grid has been rotated so that the storm's direction of motion is toward octant No. 1 (ROT coordinates). Figures 3.7 and 3.8 are identical except for the vertical scale which is

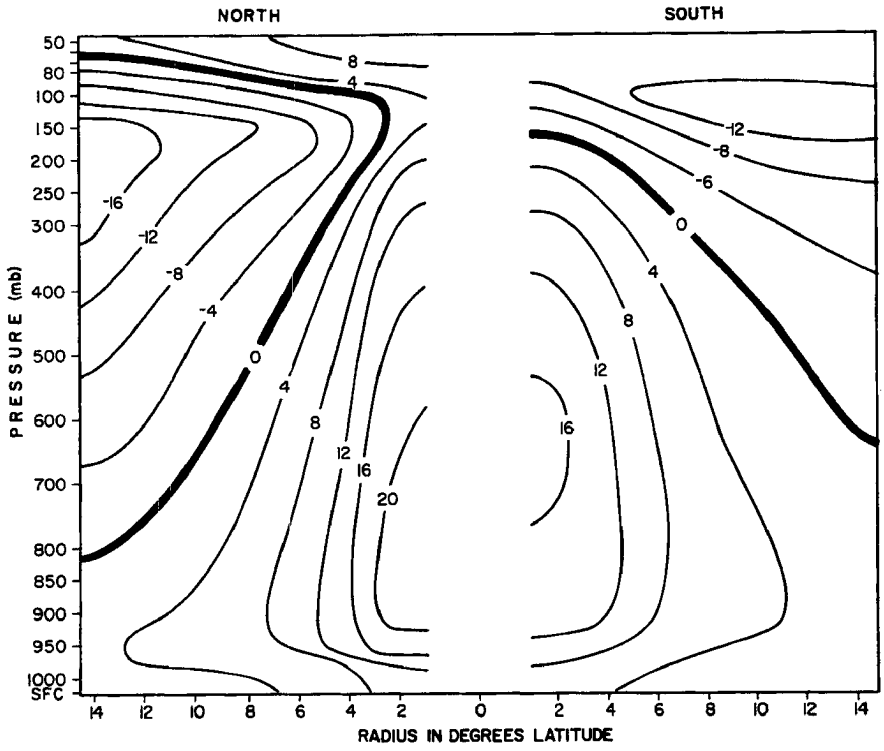

Fig. 3.4. North-South cross section of V_θ in stationary (NAT) coordinates, (m/sec).

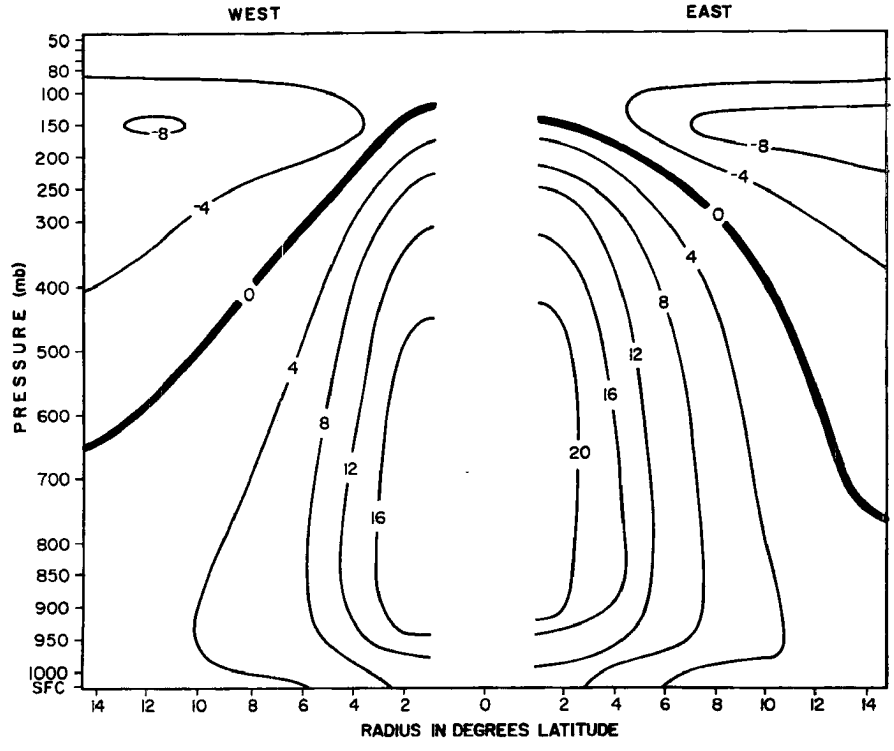

Fig. 3.5. West-East cross section of V_θ in stationary (NAT) coordinates, (m/sec).

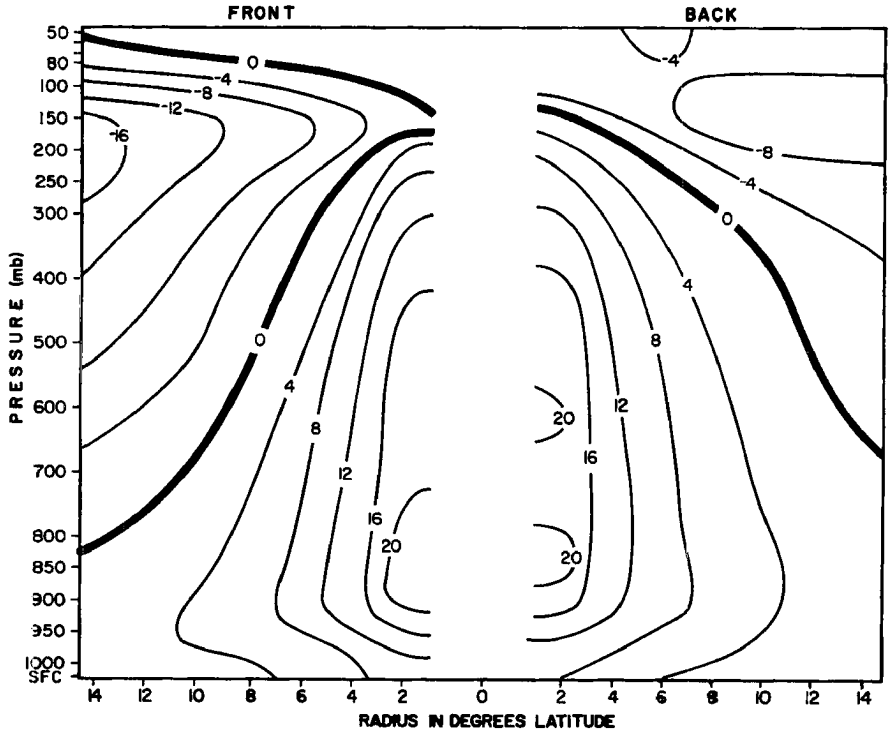

Fig. 3.6. Front-Back cross section of V_θ in stationary rotated (ROT) coordinates, (m/sec).

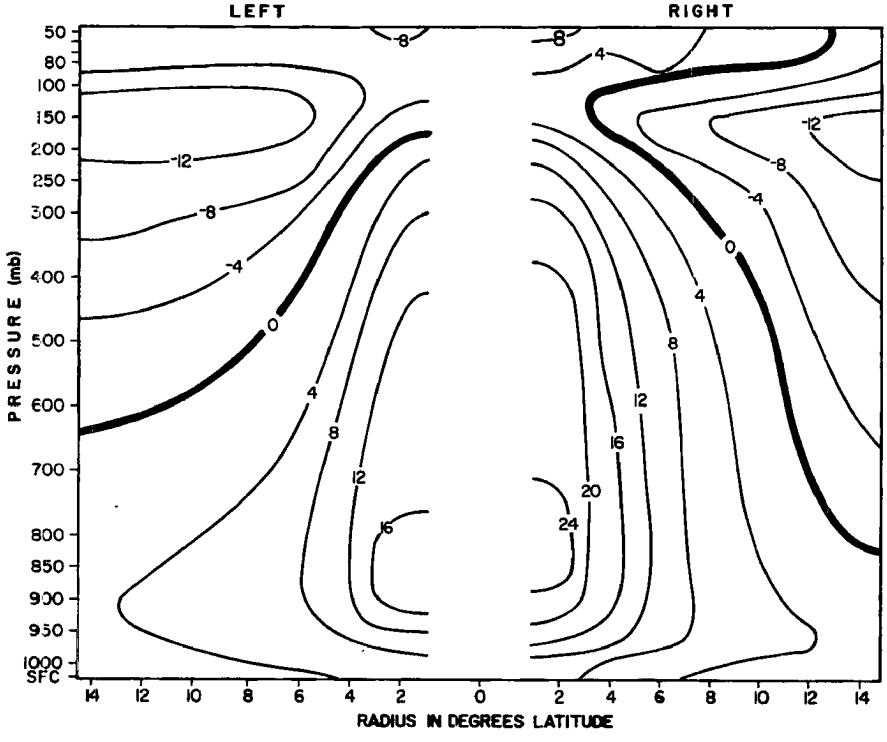

Fig. 3.7. Left-Right cross section of V_θ in stationary rotated (ROT) coordinates, (m/sec).

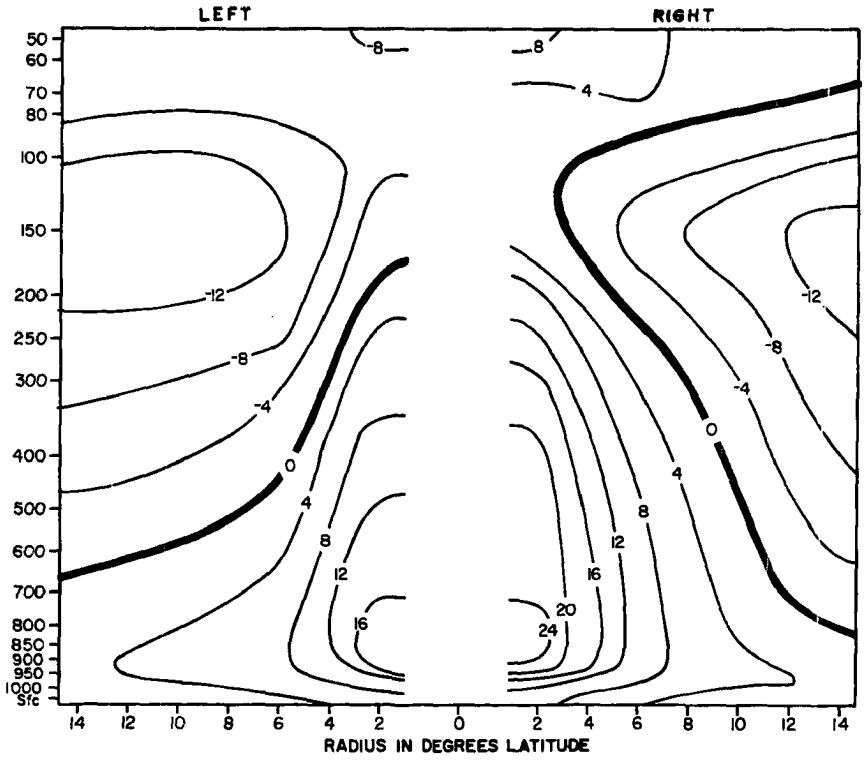

Fig. 3.8. Same as Fig. 3.7, but with vertical scale linear in height.

altered to allow increased perception of the depth of the circulation. The storm is moving into the paper in Fig. 3.7. Plan views of V_θ in this coordinate system are presented for 950, 500, and 150 mb in Figs. 3.9-3.11. The storm is nearly symmetrical front to back except for the stronger anticyclonic flow in front. In contrast the left-right cross section shows strong asymmetry with the flow being more cyclonic at all levels on the right side to 8-10^o radius. This is a result of imposing a nearly symmetrical storm height perturbation upon a large scale height gradient. The storm itself moves with the broadscale gradient or winds, but the storm perturbation causes increased cyclonic flow to the right of the storm and decreased flow to the left. This is

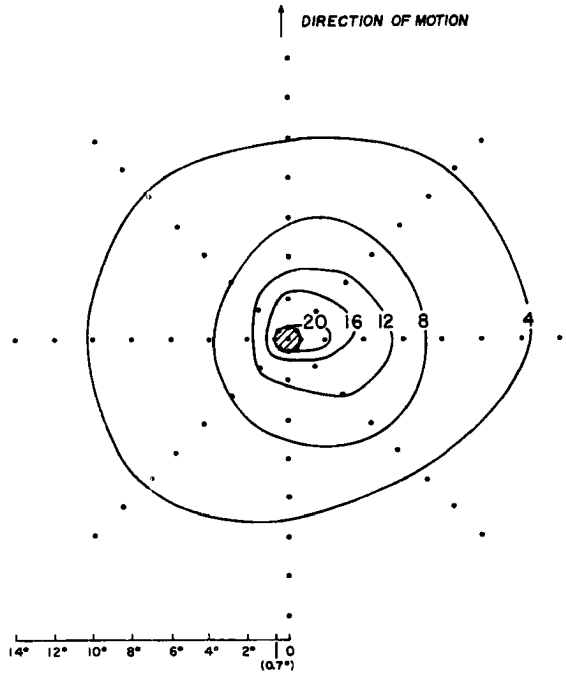

Fig. 3.9. Plan view of V_θ at 950 mb in ROT coordinates, (m/sec). Note that this is below the maximum wind level (850-900 mb).

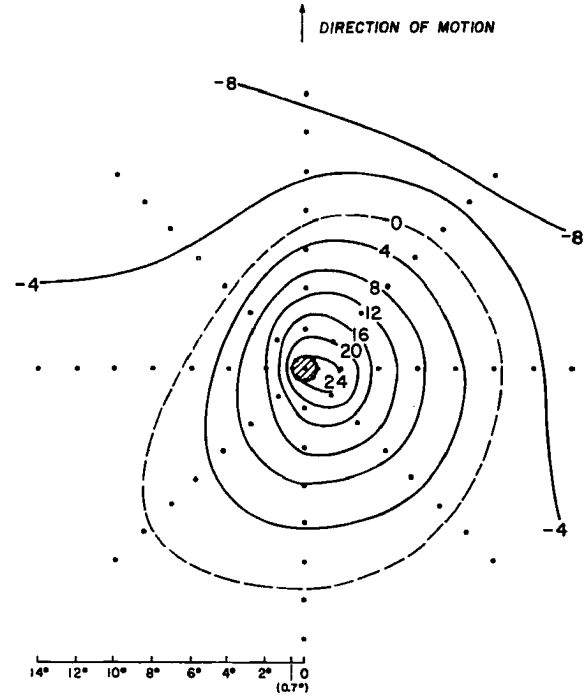

Fig. 3.10. Same as Fig. 3.9 for 500 mb.

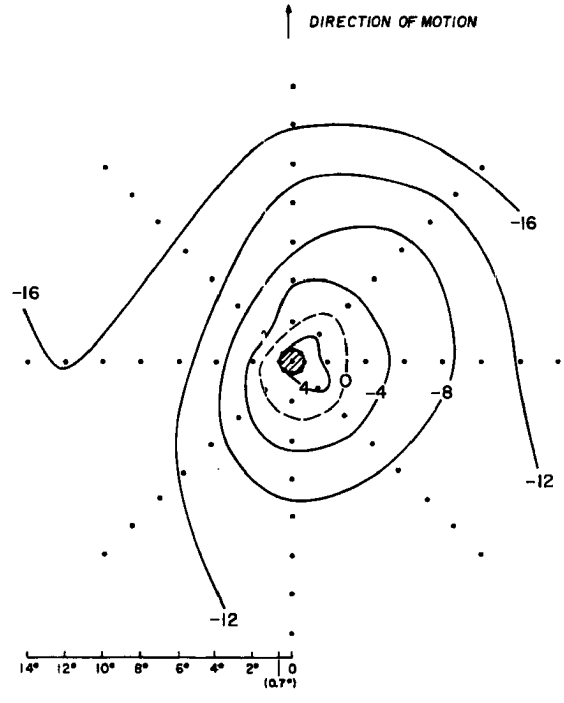

Fig. 3.11. Same as Fig. 3.9 for 150 mb.

shown schematically in Fig. 3.12. The anticyclone is nearly symmetrical in the left-right cross section.

Figures 3.13 - 3.14 show cross sections of V_θ with the appropriate storm motion vector subtracted from each sounding. These two figures are N-S and E-W cross sections (MOT system). The anticyclone has become much more asymmetric with strongest flow to the north and east. The cyclone is now nearly symmetrical out to about 6°. At larger radii the cyclonic flow is stronger to the south and west. The storm motion is related most closely to the $0\text{-}6^\circ$ environmental height and wind fields as shown by George (1975). Subtraction of the storm vectors leaves nearly symmetrical flow at inner radii. This is not true near the radius of maximum winds, however, where a right side maximum remains in moving coordinates (Shea, 1972). At greater radii the environmental

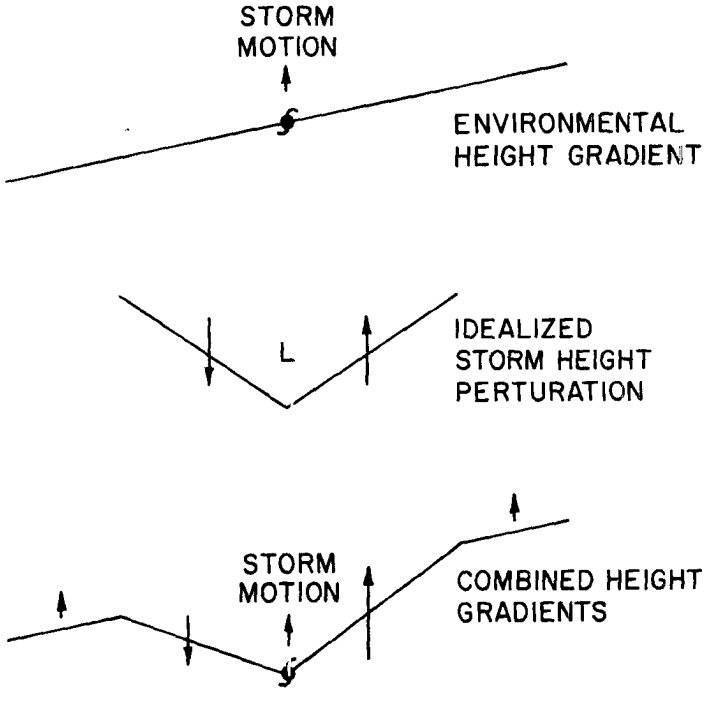

Fig. 3.12. Schematic view of symmetrical tropical storm height perturbation imposed on an environmental height gradient resulting in observed asymmetrical height gradients.

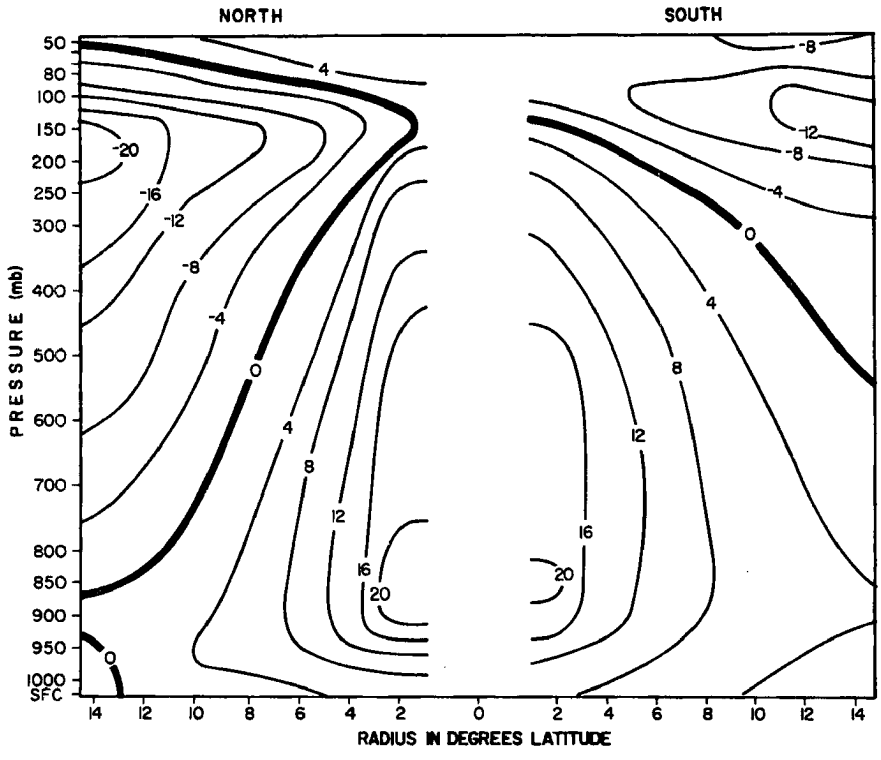

Fig. 3.13. North-South cross section of V_θ with storm motion vectors subtracted from winds (MOT), (m/sec).

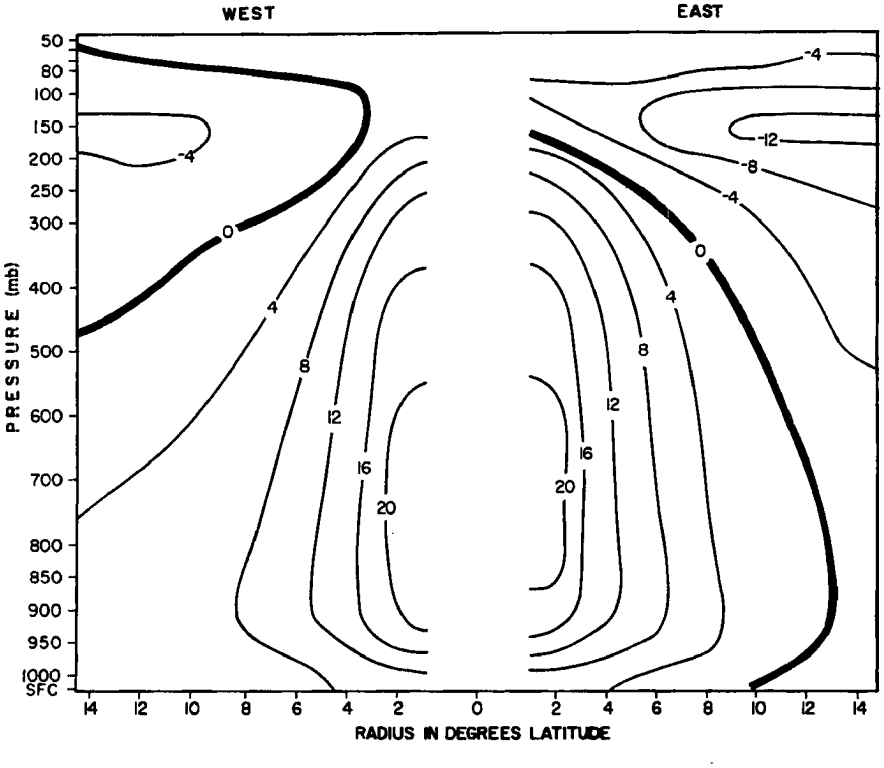

Fig. 3.14. West-East cross section of V_θ with storm motion vectors subtracted from winds (MOT), (m/sec).

gradients are weaker. The storms are moving faster than the winds at large radii, and subtraction of the storm motion vectors increases cyclonic flow to the south and west and decreases it to the north and east. In the rotated moving coordinate system (MOTROT) these results are accentuated as shown in the cross sections of Figs. 3.15-3.16 and the plan views of Figs. 3.17-3.19. The front to back cross section is the same as in the stationary rotated coordinate system by definition. The left-right cross section and plan views show near symmetry from 0-6^{o} in the cyclone but increased cyclonic flow to the left and increased anticyclonic flow to the right at all levels from 8^{o} radius outward.

It should not be inferred from the above figures that the tangential wind field is relatively smooth. The winds around tropical storms are notoriously variable, particularly in the outflow layer where one or more intense anticyclonic jets exist. The composite data smooths over the variability of individual storms, but the effects of these asymmetries are largely compensated for in the budget studies of Chapters 5-8.

The satellite-observed cloud masses associated with tropical cyclones are typically no more than 3-4^{o} radius. The enhanced convection and resultant warming are concentrated in that inner region. Therefore, it is somewhat surprising that the cyclonic and anticyclonic circulations extend outward to at least 15^{o} radius - the edge of the compositing grid. Part of the broad-scale circulation patterns shown in Figs. 3.3-3.19 may be reflections of the mean environmental flow field described by Newell et al. (1972) and Sadler (1975). However, it

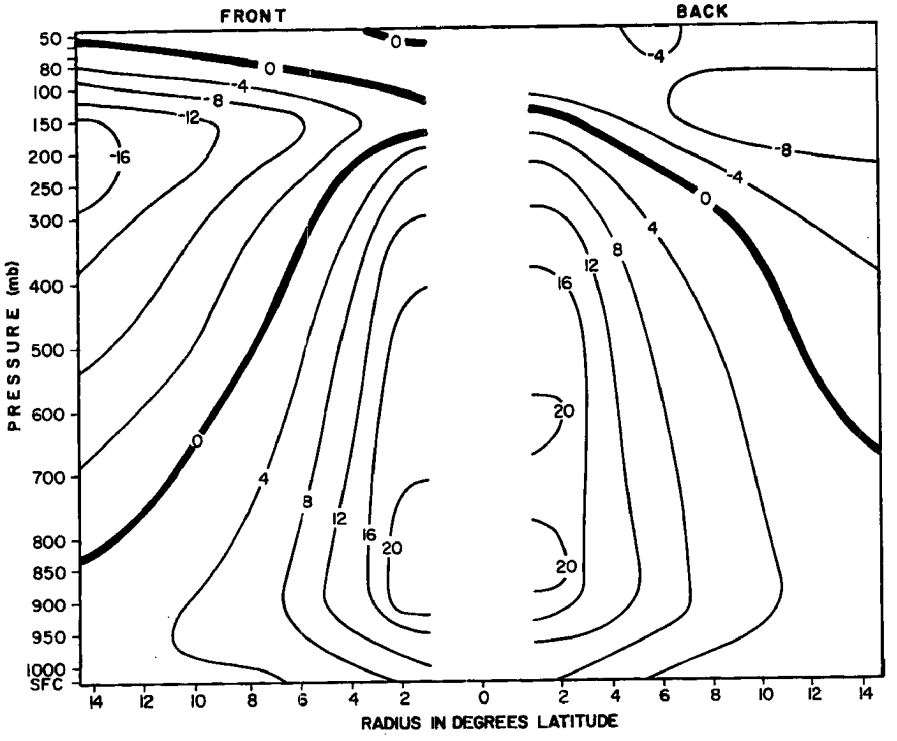

Fig. 3.15. Front-Back cross section of V_θ in rotated coordinates with storm motion vectors subtracted from winds (MOTROT), (m/sec).

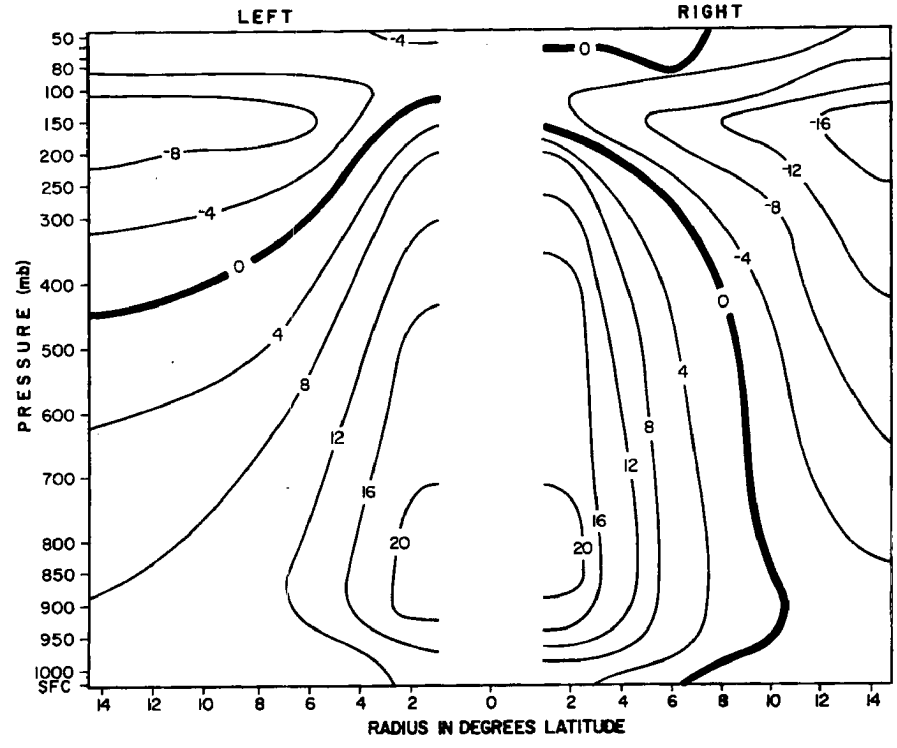

Fig. 3.16. Left-Right cross section of V_θ in rotated coordinates with storm motion vectors subtracted from winds (MOTROT), (m/sec).

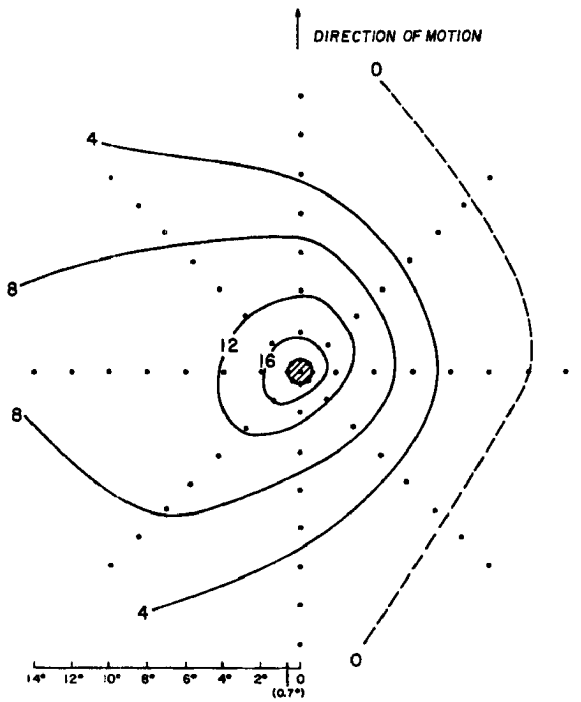

Fig. 3.17. Plan view of V_θ at 950 mb (below maximum wind level) in MOTROT system, (m/sec).

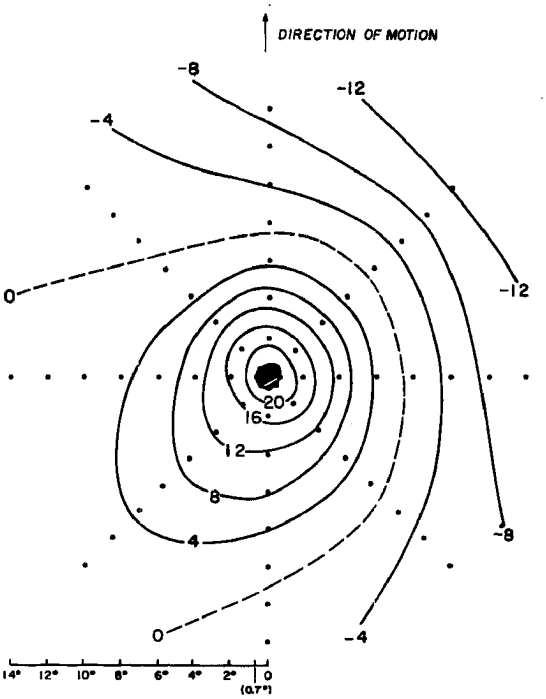

Fig. 3.18. Same as Fig. 3.17 for 500 mb.

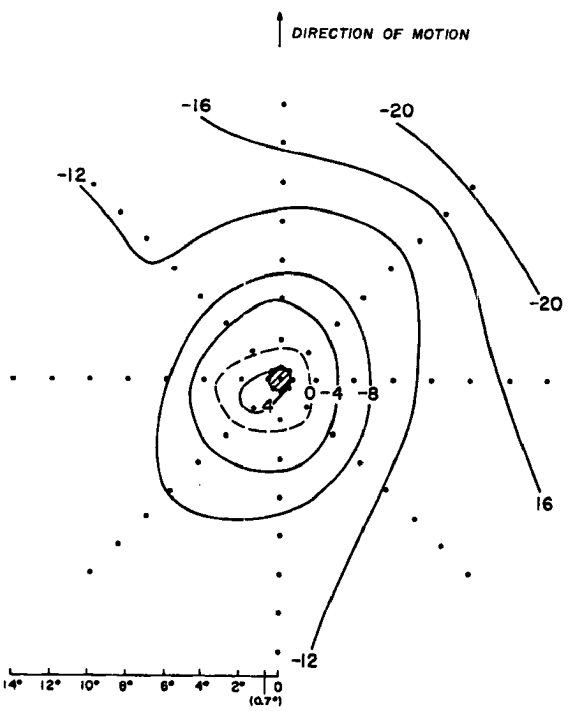

Fig. 3.19. Same as Fig. 3.17 for 150 mb.

does not seem likely that all of the outer radii circulation is climatological. Figures 3.20-3.23 show left-right cross sections of V_θ in rotated stationary coordinates for 4 different intensity classes of storms. Figure 3.20 is for tropical depressions (central pressure (P_c) >1000 mb), and Figs. 3.21-3.23 are for storms with $980<P_c \leq 1000$, $950< P_c \leq 980$, and $P_c \leq 950$ mb, respectively. The average locations of the 3 storm groups with $P_c \leq 1000$ mb are within 2^o latitude of each other with the weaker storms being slightly farther south. It is clear that the scales of the circulations of these different storms are nearly identical. The relative depths and horizontal extents of the cyclonic and anticyclonic flow regions are similar except for the region south of the weakest disturbances. However, the intensity of the broad-scale tangential circulation increases with decreasing central pressure. It seems clear that the average tropical cyclone circulation extends over an extremely large area and is not a relatively small closed circulation.

3.3 Radial Winds

Accurate radial wind (v_r) values are essential for computations of the dynamics and energetics of tropical cyclones. Unfortunately, it is very difficult to obtain enough data around a single storm to construct reliable vertical profiles of this parameter. Compositing provides the necessary amounts of data although careful handling of the data is crucial to prevent biases from systematic balloon and storm motions as discussed previously.

Mean 2-dimensional radial wind profiles in stationary (NAT) coordinates are shown in Figs. 3.24-3.26 for $2-6^o$, and in Fig. 3.27

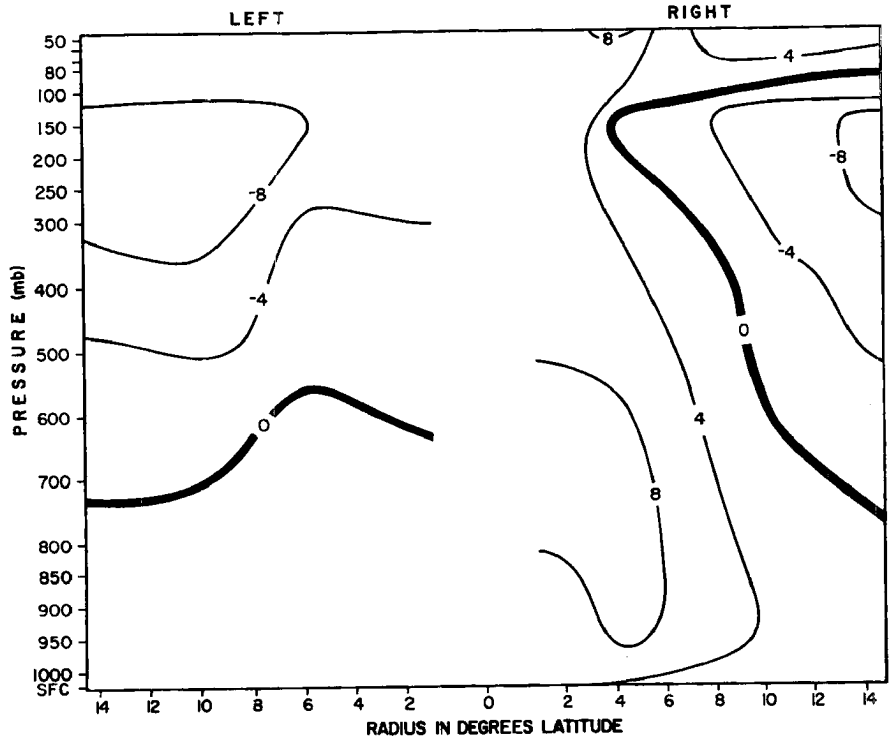

Fig. 3.20. Left-Right cross section of V_θ in rotated coordinates (ROT) for storms with central pressures (P_c) > 1000 mb, (m/sec).

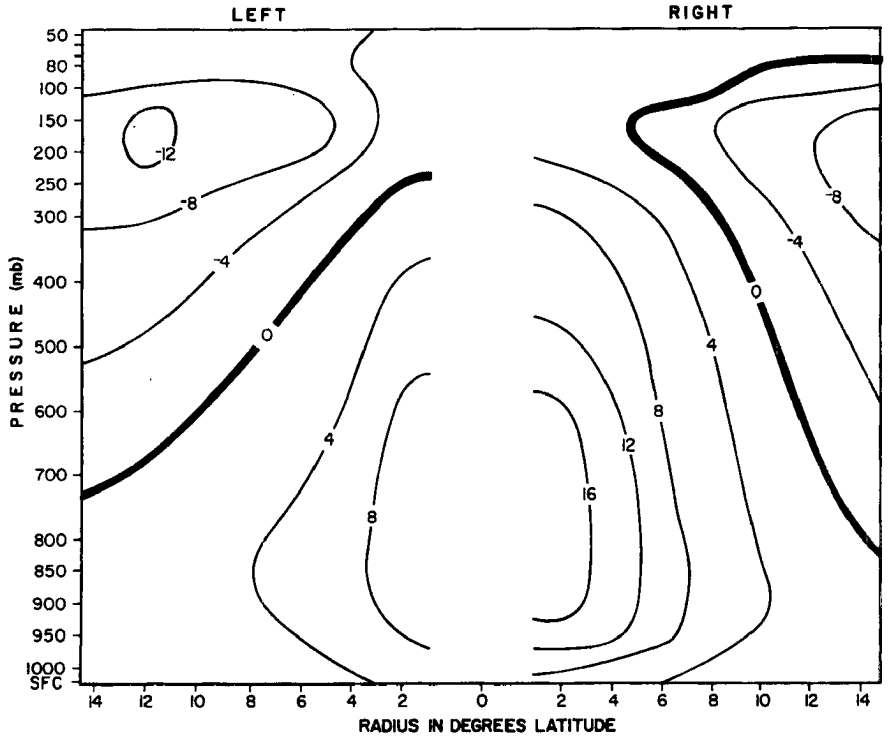

Fig. 3.21. Same as Fig. 3.20 for storms with $980 < P_c \leq 1000$ mb.

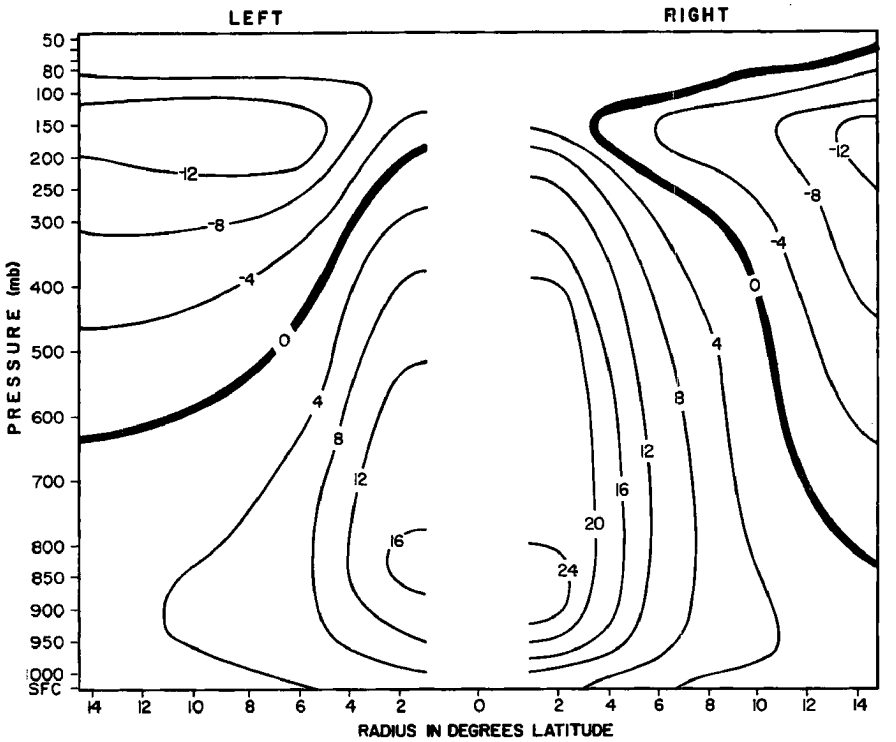

Fig. 3.22. Same as Fig. 3.20 for storms with $950 < P_c \leq 980$ mb.

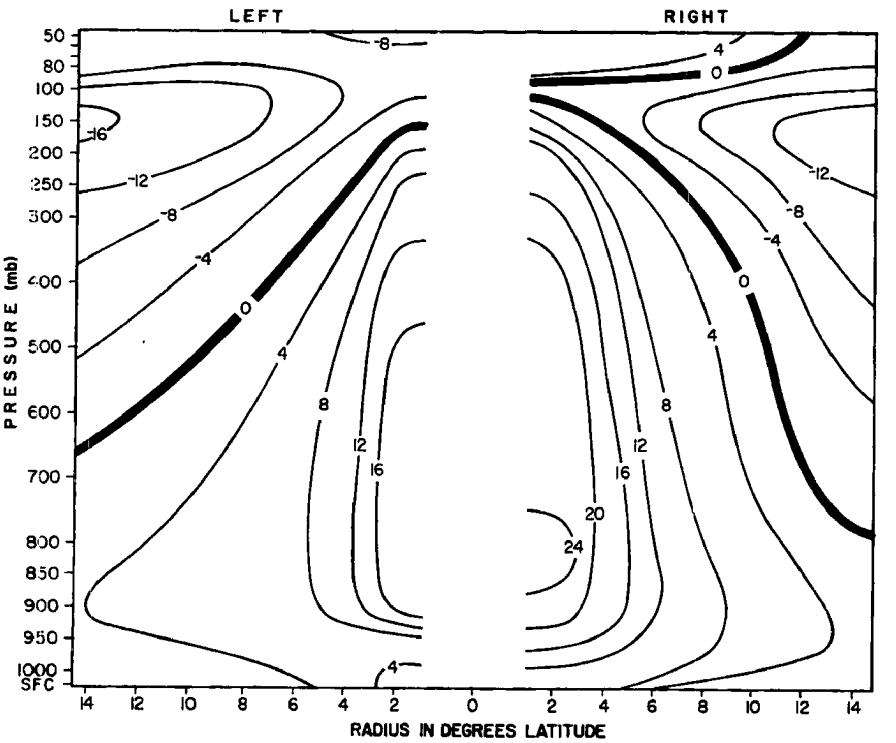

Fig. 3.23. Same as Fig. 3.20 for storms with $P_c \leq 950$ mb.

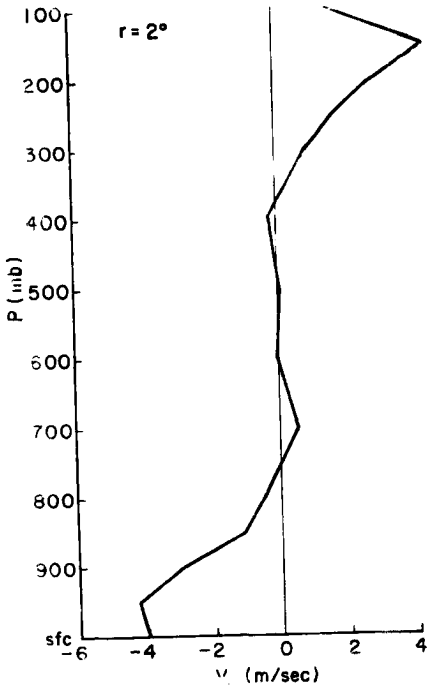

Fig. 3.24. 2-dimensional vertical profile of radial winds (V_r) in m/sec at $r=2^o$.

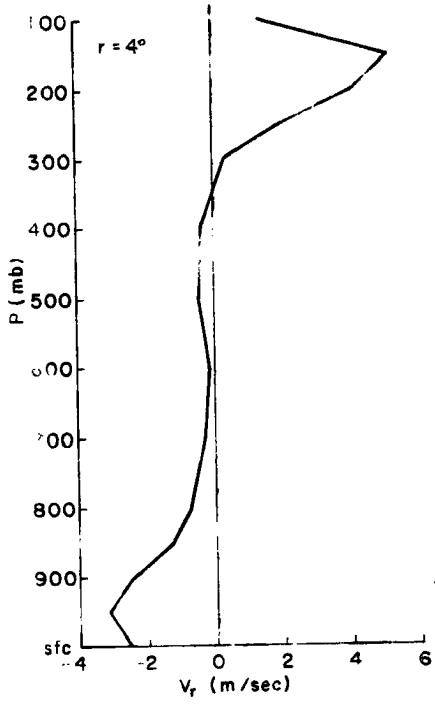

Fig. 3.25. Same as Fig. 3.24 for $r=4^o$.

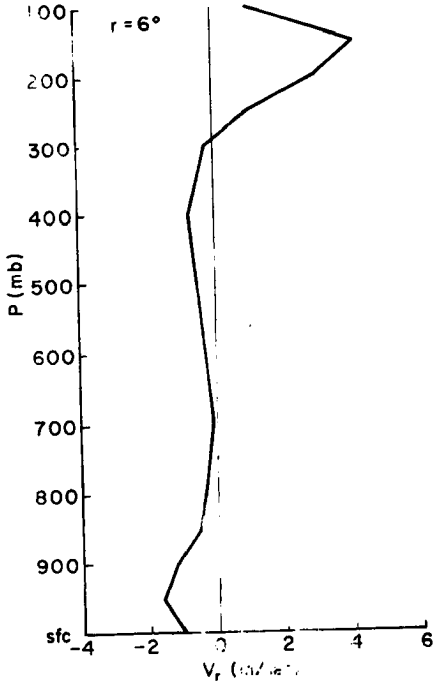

Fig. 3.26. Same as Fig. 3.24 for $r=6^o$.

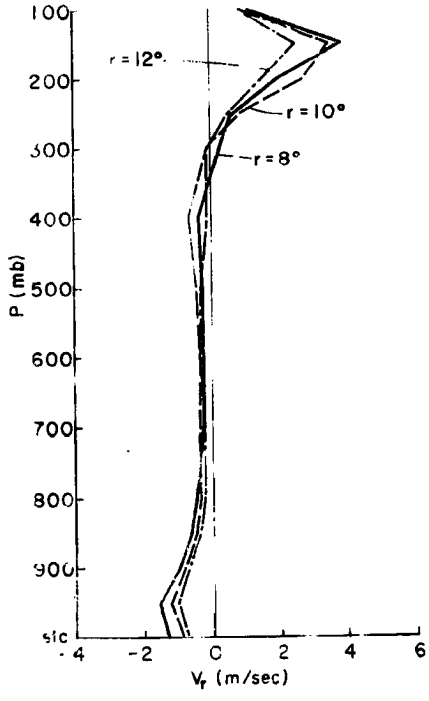

Fig. 3.27. Same as Fig. 3.24 for $r=8^o$, 10^o and 12^o.

for 8-12°. The profiles are adjusted slightly by constant correction factors to achieve mass balance. Several features are immediately apparent. The maximum inflow (subject to the vertical resolution of the data) occurs at 950 mb. The outflow is maximum at 150 mb, higher than is usually assumed. At 2° radius the inflow and outflow are confined to relatively thin vertical levels, sfc-800 mb and 300-100 mb respectively. This fits conventional theory quite well. However, from 4° outward middle level inflow becomes increasingly important as the role of the low level frictional convergence diminishes. This has important implications which are shown in the budget analyses of Chapters 5-8. It is possible that the mid-level inflow results from an upward extension of frictional convergence by cloud momentum fluxes or from net entrainment into deep clouds, but the apparent lack of such inflow at 2° radius where convection is strong indicates that these mechanisms are not dominant. It is possible that the 2° radial wind profile is slightly in error since it represents the smallest data set of the 6 profiles. Alternatively, the middle level inflow at larger radii may result from radiationally driven forcing as discussed in Jacobson and Gray (1976). The effects of this middle level inflow upon the divergence and vertical motion fields are shown in the next two sections.

Small but persistent features of the radial wind profiles are a slight inflow maximum at 400 or 500 mb and a minimum at 700 mb. These have also been observed in N.W. Pacific steady state cloud clusters by Zehr (1976).

Vertical cross sections and plan views of the radial wind are shown in Figs. 3.28-3.48 for each of the four coordinate systems to

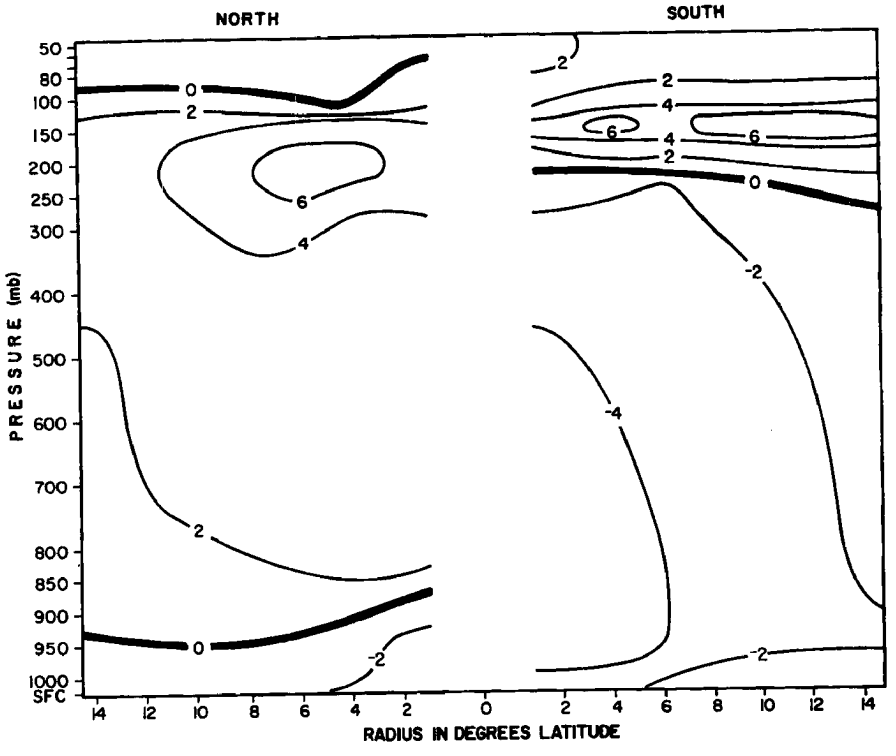

Fig. 3.28. North-South cross section of V_r in stationary coordinates (NAT) for mean steady state typhoon, (m/sec).

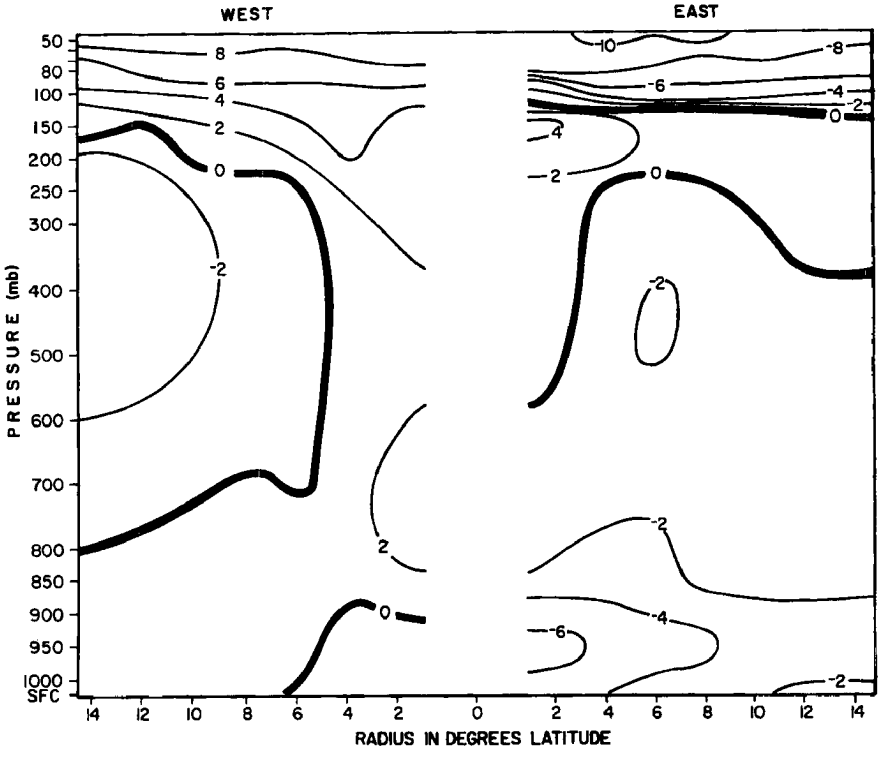

Fig. 3.29. West-East cross section of V_r in stationary coordinates (NAT), (m/sec).

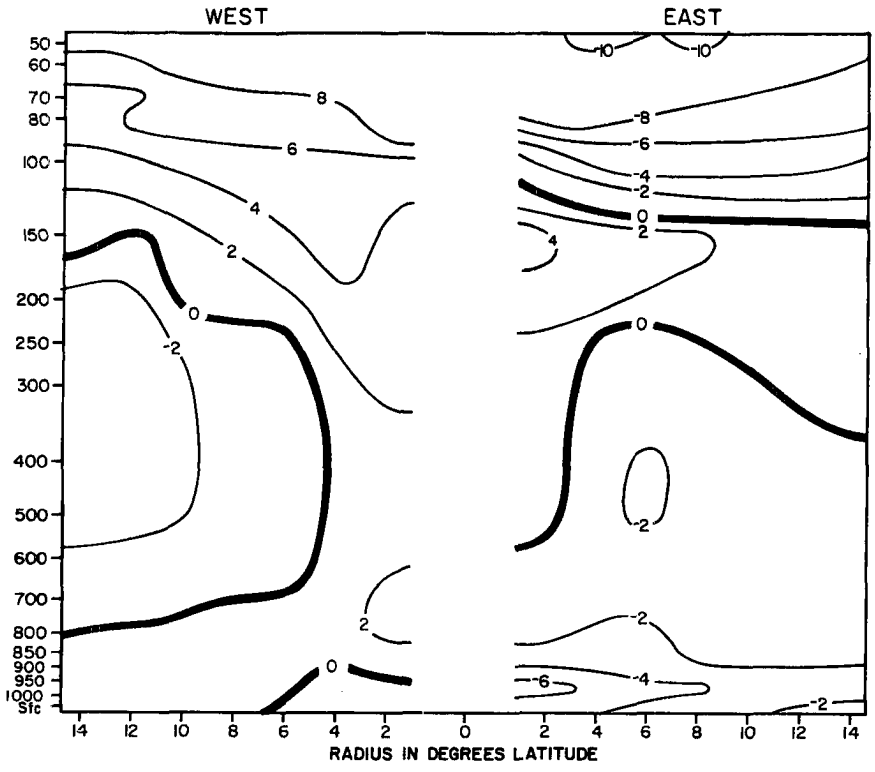

Fig. 3.30. Same as Fig. 3.29 but with vertical scale linear in height.

show persistent asymmetries in the flow field. The first 6 figures are in stationary geographical coordinates (NAT). Figures 3.29 and 3.30 are identical except for the vertical scale. Outflow in the 300-100 mb layer is directed almost equally north and south with the level of maximum outflow dropping to the north with decreasing tropopause height. The outflow is strongly concentrated in 2 mean outflow jets northeast and southwest of the storm center. There is evidence of a mean trough to the north-northwest. Mean outflow to the east and west is weak. Above 100 mb the stratospheric easterlies are relatively unperturbed and show a small southerly component. Low level inflow occurs on all sides from 4^{o} inward, but it shows a pronounced maximum to

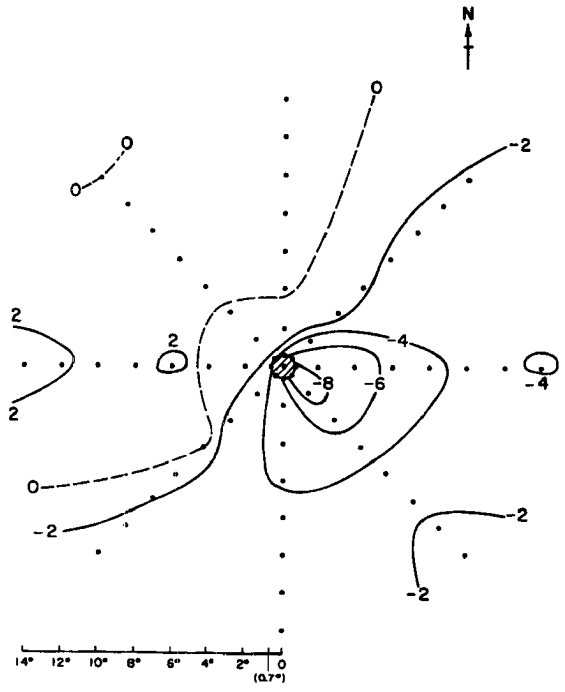

Fig. 3.31. Plan view of V_r in stationary geographical coordinates (NAT) at 950 mb, (m/sec).

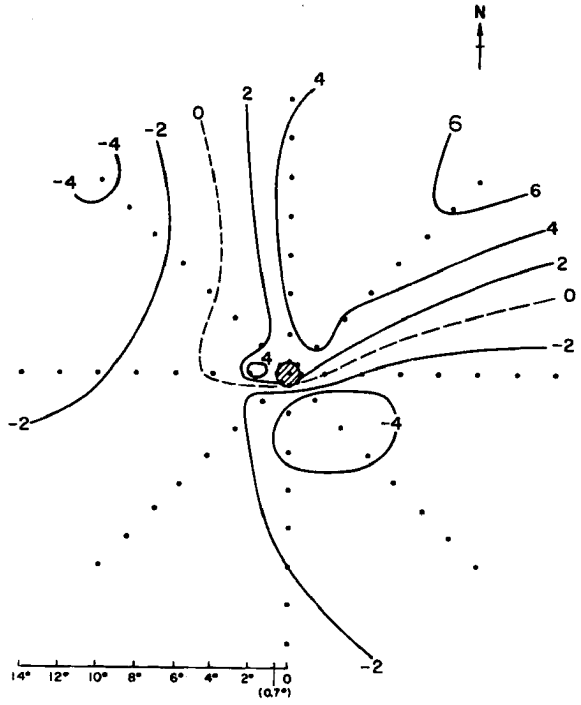

Fig. 3.32. Same as Fig. 3.31 for 500 mb.

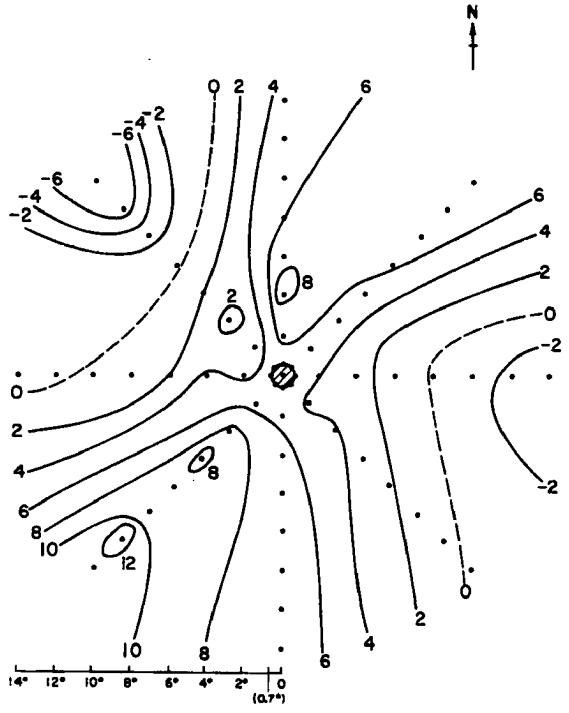

Fig. 3.33. Same as Fig. 3.31 for 150 mb.

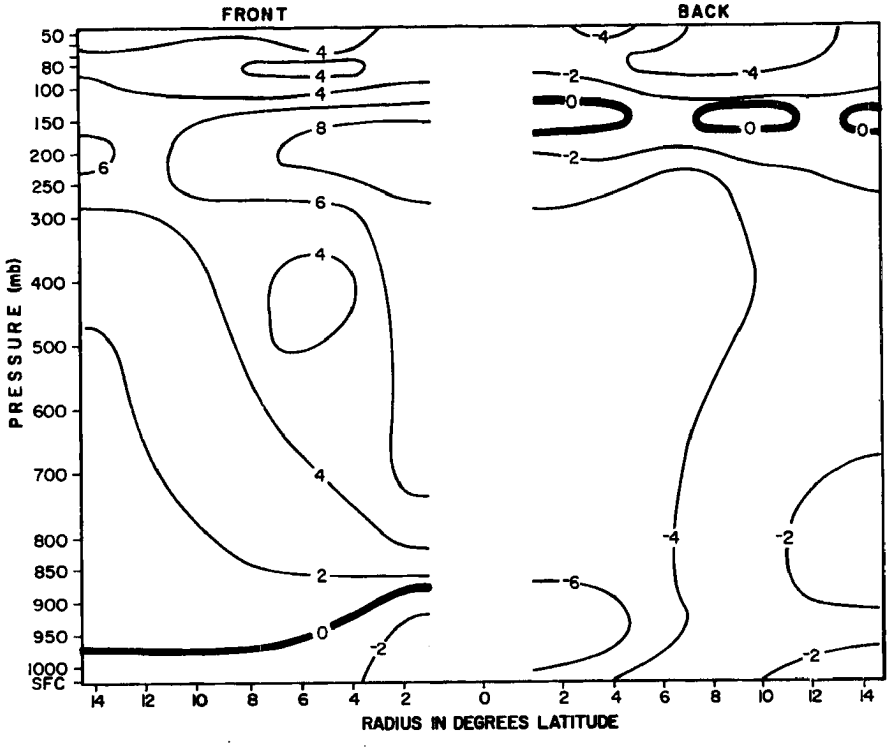

Fig. 3.34. Front-Back cross section of V_r in stationary rotated (ROT) coordinates, (m/sec).

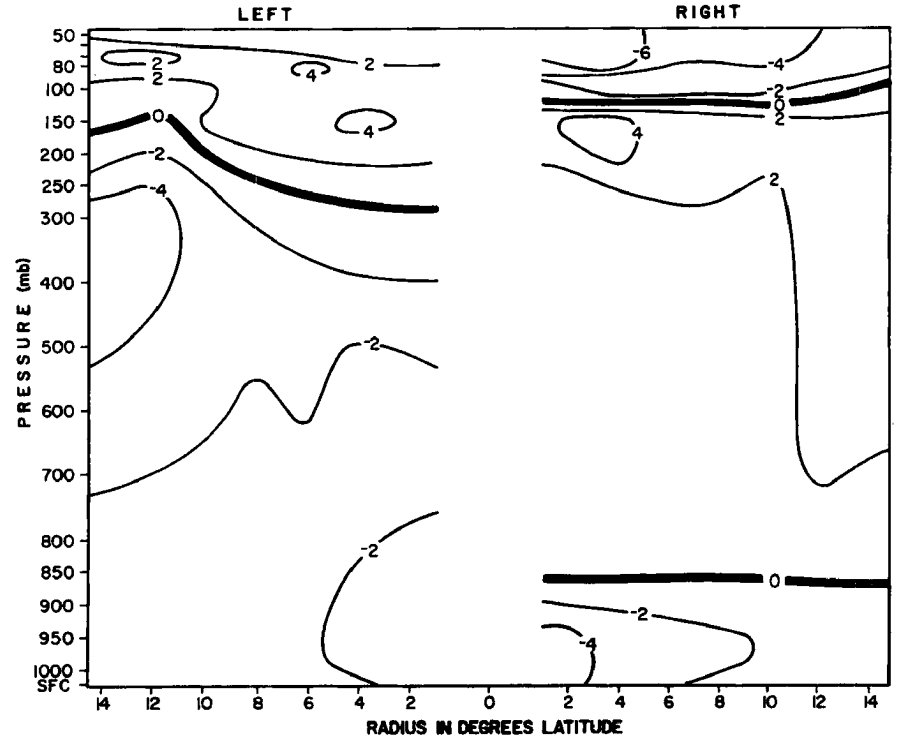

Fig. 3.35. Left-Right cross section of V_r in ROT coordinates, (m/sec).

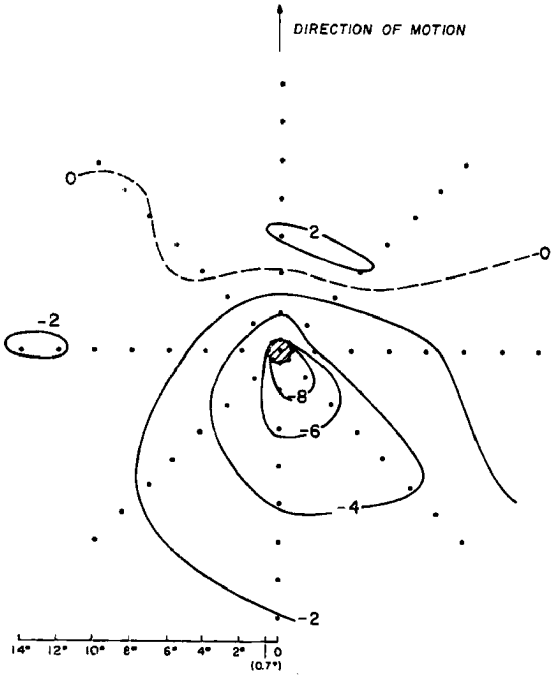

Fig. 3.36. Plan view of V_r in ROT coordinates at 950 mb, (m/sec).

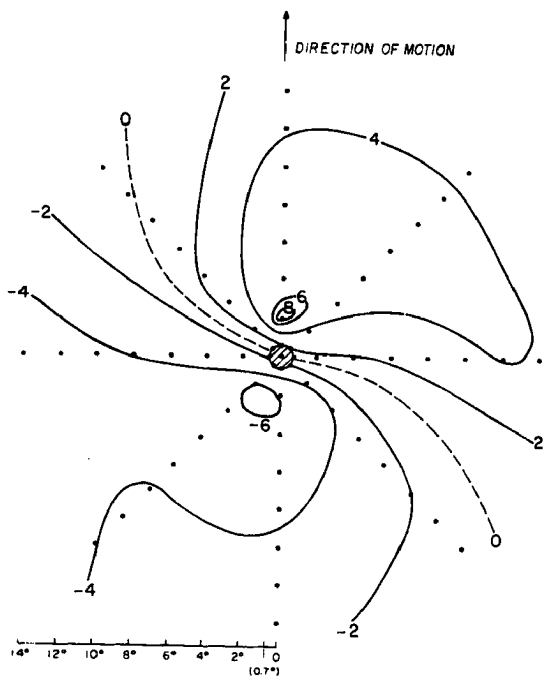

Fig. 3.37. Same as Fig. 3.36 for 500 mb.

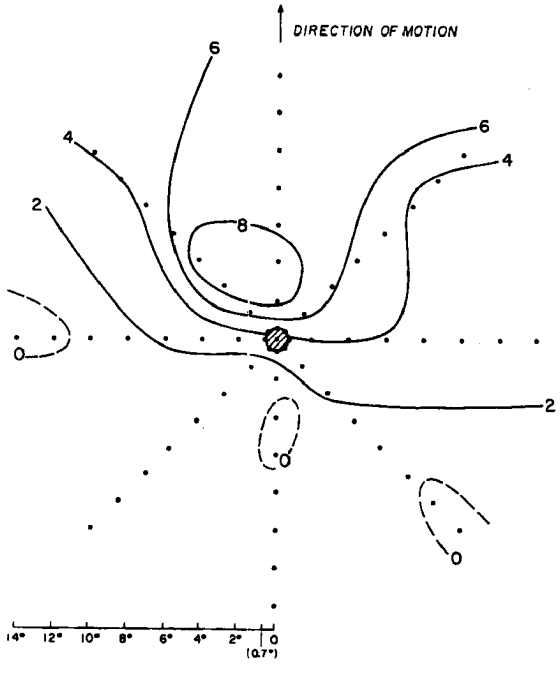

Fig. 3.38. Same as Fig. 3.36 for 150 mb.

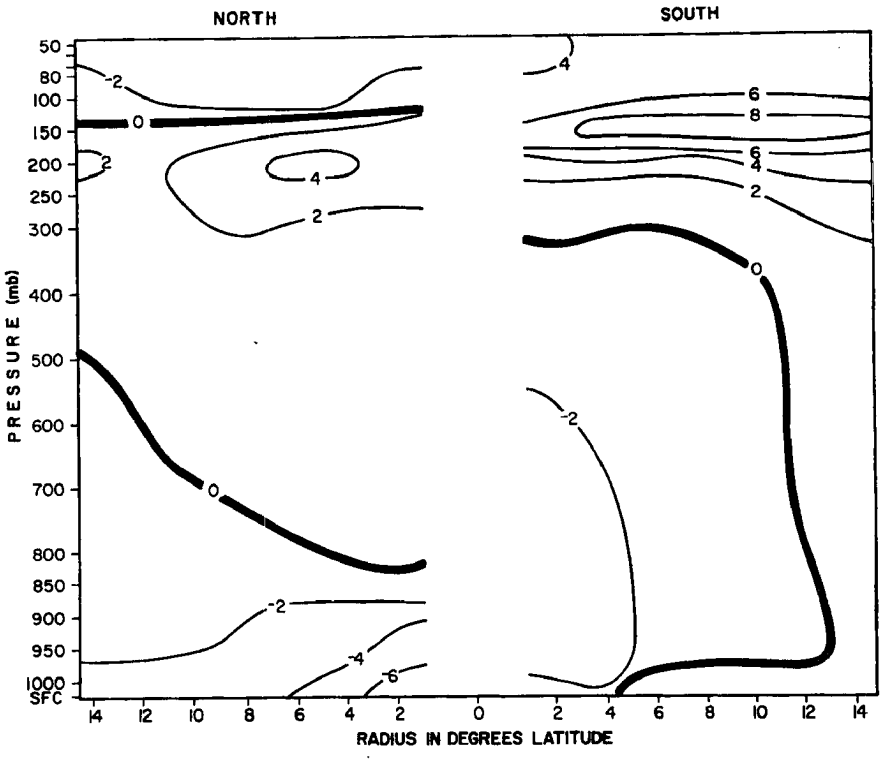

Fig. 3.39. North-South cross section of V_r with storm motion vectors subtracted from winds (MOT), (m/sec).

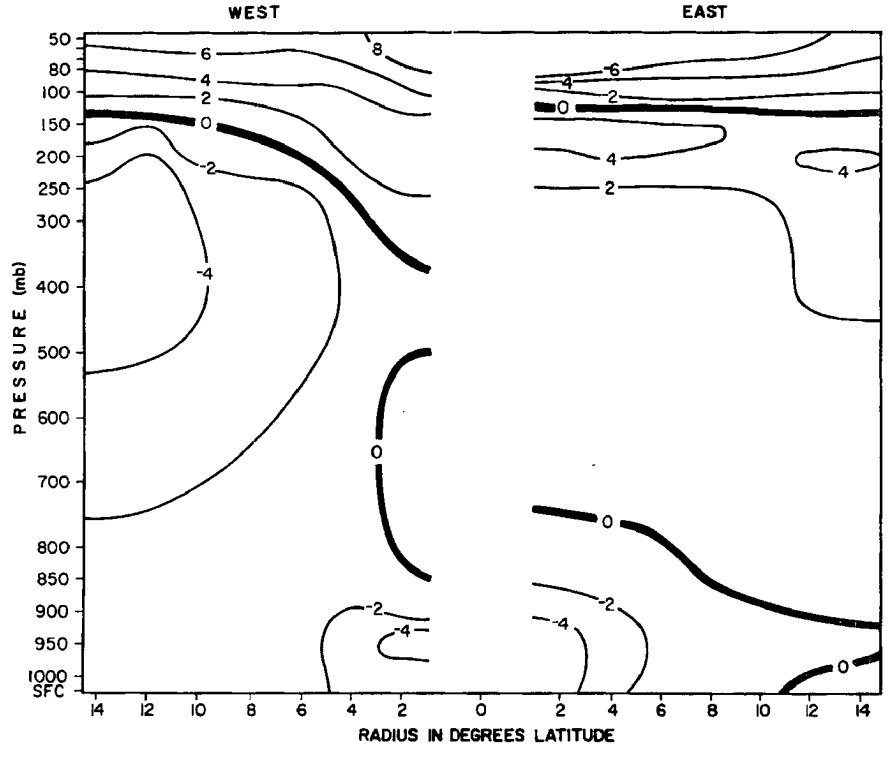

Fig. 3.40. West-East cross section of V_r with storm motion subtracted from winds (MOT), (m/sec).

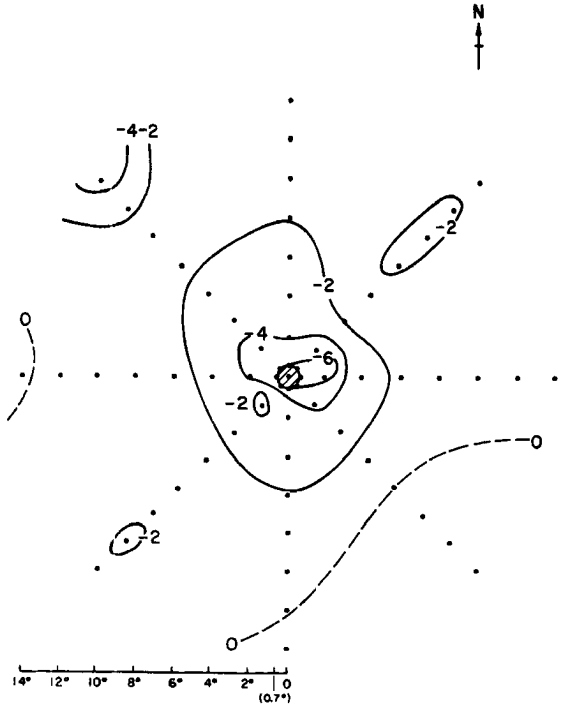

Fig. 3.41. Plan view of V_r in MOT coordinates at 950 mb, (m/sec).

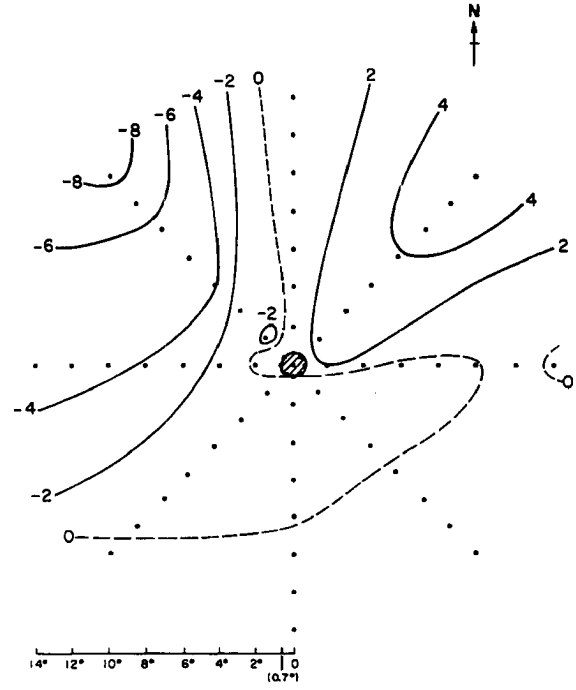

Fig. 3.42. Same as Fig. 3.41 for 500 mb.

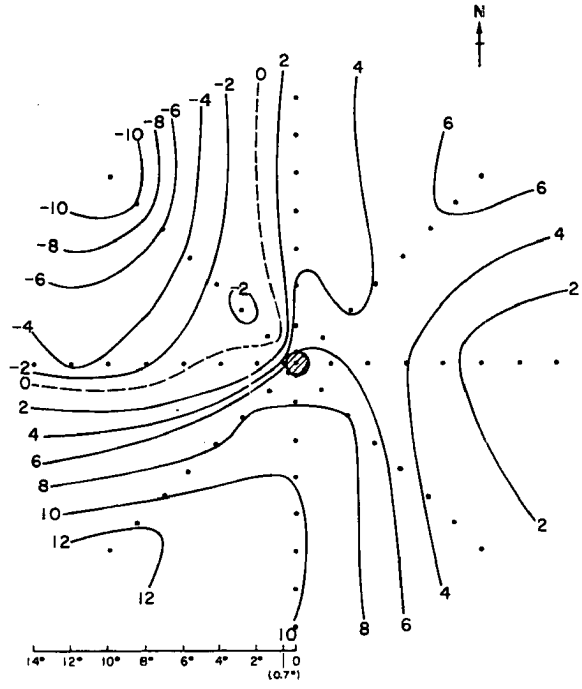

Fig. 3.43. Same as Fig. 3.41 for 150 mb,

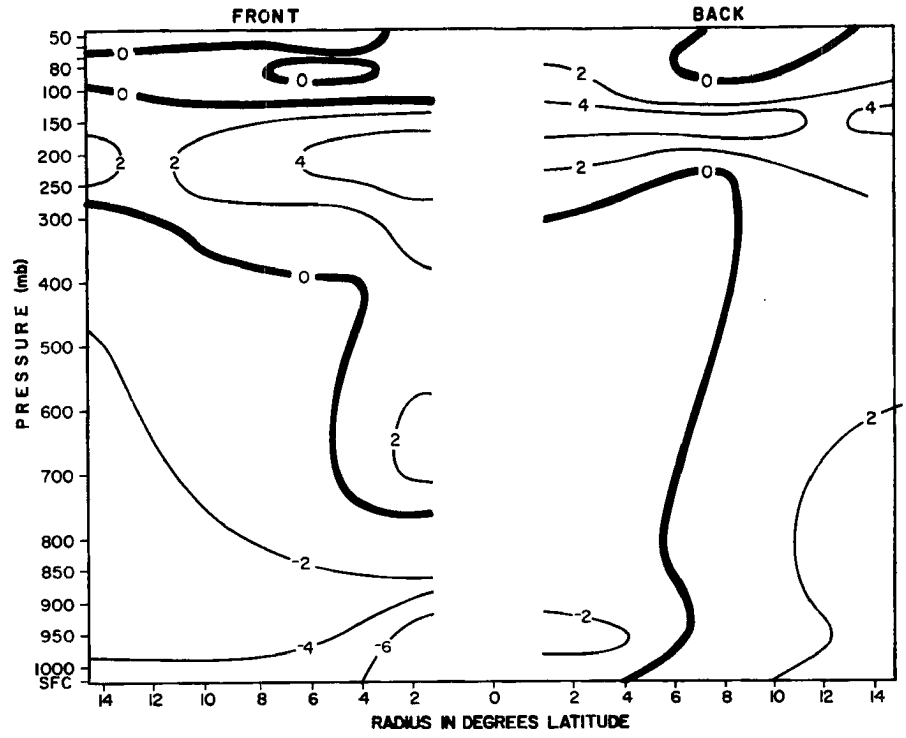

Fig. 3.44. Front-Back cross section of V_r in rotated coordinates with storm motion vectors subtracted from winds (MOTROT), (m/sec).

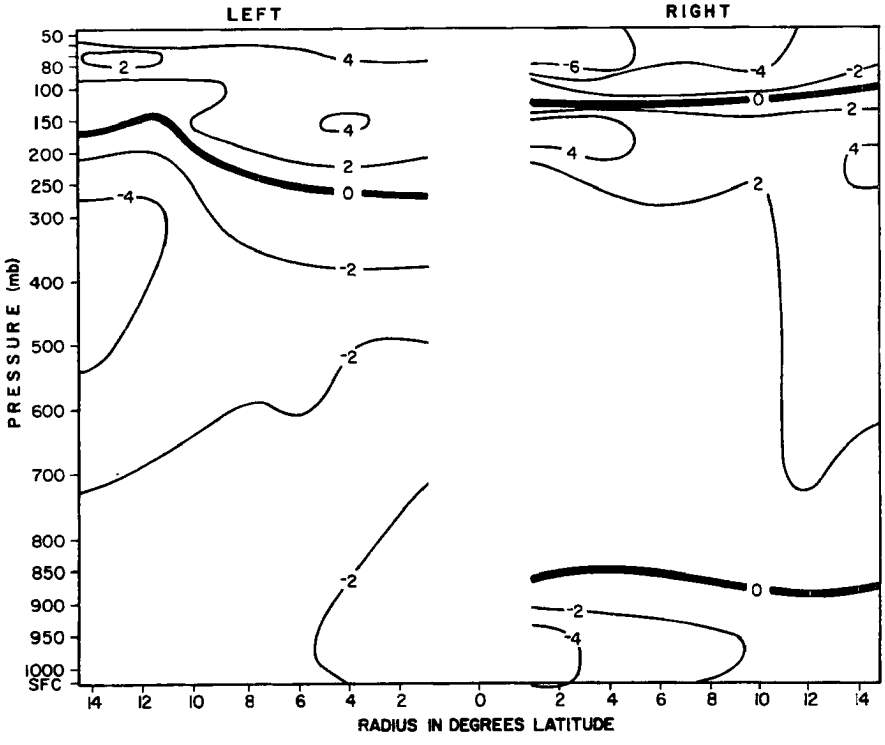

Fig. 3.45. Left-Right cross section of V_r in MOTROT coordinates, (m/sec).

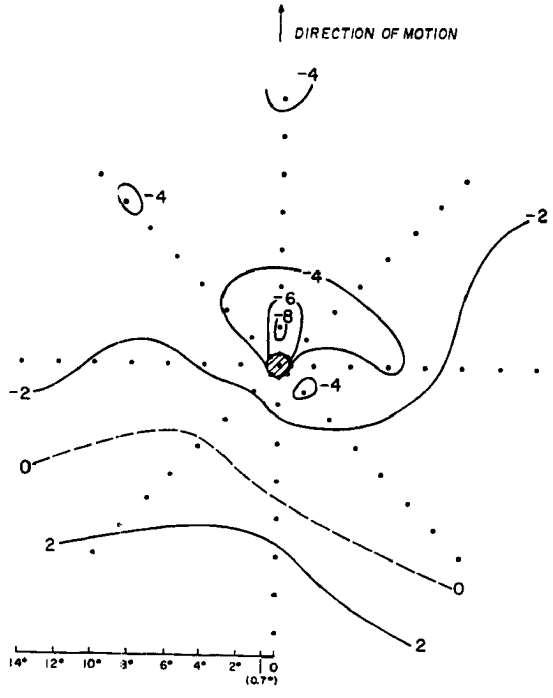

Fig. 3.46. Plan view of V_r in MOTROT coordinates at 950 mb, (m/sec).

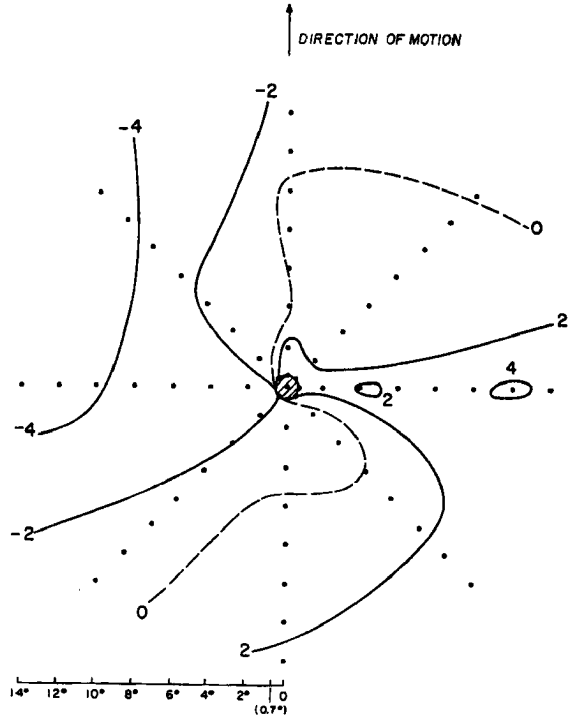

Fig. 3.47. Same as Fig. 3.46 for 500 mb.

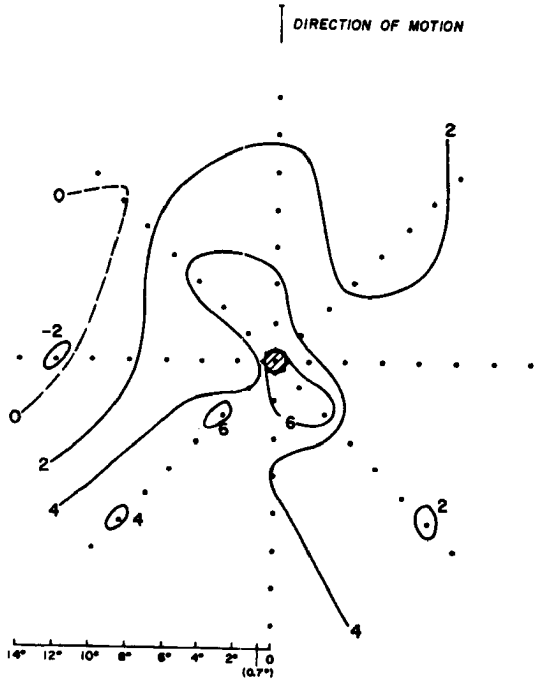

Fig. 3.48. Same as Fig. 3.46 for 150 mb.

the east and south. There is substantial southwest to northeast flow in the middle levels.

When the compositing grid is aligned with the direction of storm motion (ROT system, Figs. 3.34-3.38), the flow is predominantly inward to the rear and left of the storm and outward to the front and right, a feature also noted in early hurricane flights (Gray, 1962). Low level inflow is more symmetrical than in the NAT case, but there is an inflow maximum to the rear and a minimum in front of the storm. It is noteworthy that there is no significant outflow between 100 and 300 mb to the rear of the storm. The composite of storms moving in various directions has destroyed the resolution of the outflow jets. These jets apparently have preferred geographical locations independent of the direction of storm motion.

The storm motion vectors are subtracted from the winds in Figs. 3.39-3.48 (MOT and MOT-ROT systems). The N-S and E-W cross sections of Figs. 3.39-3.40 and the plan views of Figs. 3.41-3.43 (MOT) now show stronger upper level outflow to the south and east of the storm relative to the stationary (NAT) coordinate system. Upper outflow is correspondingly diminished to the north and west. There is a west to east flow-through in the moving system at higher levels reflecting the upper level trough NNW of the storm. Large scale low level inflow is roughly symmetrical in the east-west direction in moving coordinates, but there is maximum inflow from the north and a minimum from the south.

The rotated moving system (MOTROT) shows substantial variations from the stationary rotated system (ROT). There is little radial flow-through in the middle levels in the MOTROT system, although there

is some weak left to right flow. This indicates that middle-level ventilation of the moving storm is probably weak. Low level inflow occurs from all sides and is maximum from the front. Upper level outflow is rather symmetrical with a weak minimum to the left, as the outflow jets are again obscured by the rotation of the coordinate system for each storm.

The combined V_r and V_θ values yield mean inflow angles. Ausman (1959) found a mean surface inflow angle of 16^o for the $2\text{-}6^o$ radius region based on ship reports around 6 hurricanes. Inflow angles at 2^o, 4^o and 6^o for the present study are shown in Fig. 3.49. The values at 950 mb are about those reported by Ausman for the surface. It is not clear whether the higher surface inflow angles of the present study are genuine or merely a reflection of the island locations of the stations. The angles are essentially constant from $2\text{-}6^o$ below 950 mb, while the mean inflow angle increases with radius from 700-950 mb reflecting the deep inflow at 4^o and 6^o.

3.4 Total Winds

The total wind fields at various levels are shown in Figs. 3.50-3.57. The first five figures are in stationary geographical (NAT) coordinates, and the latter three in moving geographical (MOT) coordinates. Wind barbs are in knots. No analysis is presented inside 2^o radius. Most of the features evident in these figures have been noted in the V_θ and V_r sections above. The rather strong 150 mb radial shear between the west and southwest octants is interesting. This shear region, almost directly to the left of the mean storm motion, indicates that the outflow jets to the west of the storm primarily occur well south of the storm latitude. The upper level outflow to the north

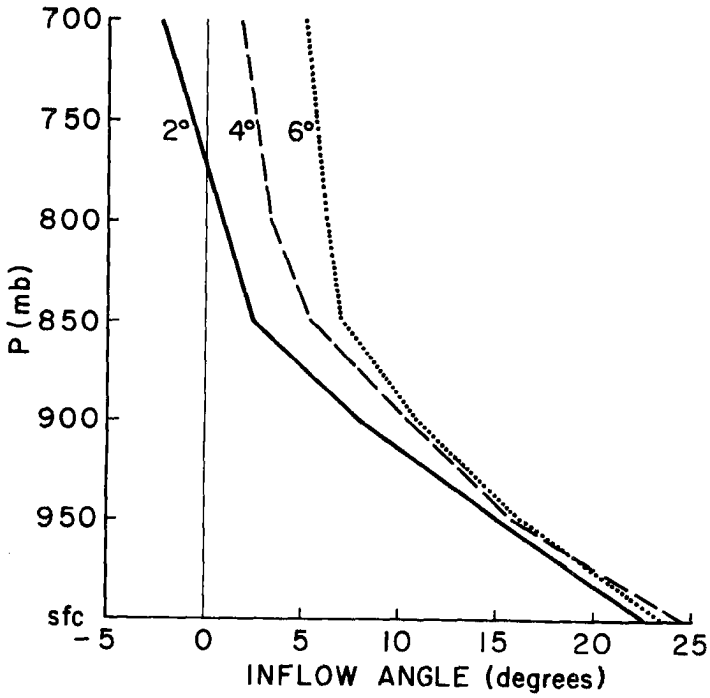

Fig. 3.49. Inflow angles at r=2°, 4° and 6°.

and east of the storm is less well defined indicating more variability in the location of the outflow jets in this region. The top of the storm occurs between 100 mb and 70 mb with undisturbed easterlies prevailing at the latter level (Fig. 3.54).

3.5 Divergence

Mean divergence profiles computed from radial wind values are shown in Figs. 3.58-3.61. The 0-2° region (Fig. 3.58) shows distinct low level inflow and upper level outflow levels. Note that 0-2° divergence is plotted on a different scale than the 2-12° profiles. The 2-4° band divergence profile shows deep convergence up through 300 mb (Fig. 3.59). There is no strong boundary layer convergence maximum.

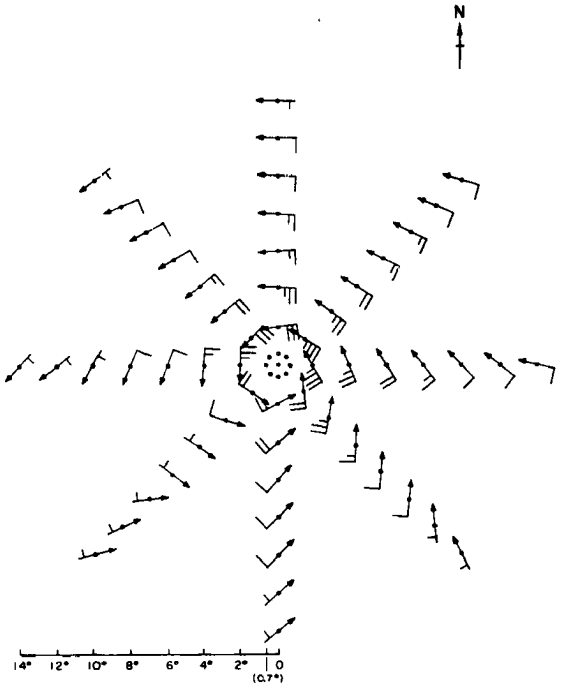

Fig. 3.50. Total winds at 950 mb in stationary geographical coordinates (NAT), (knots).

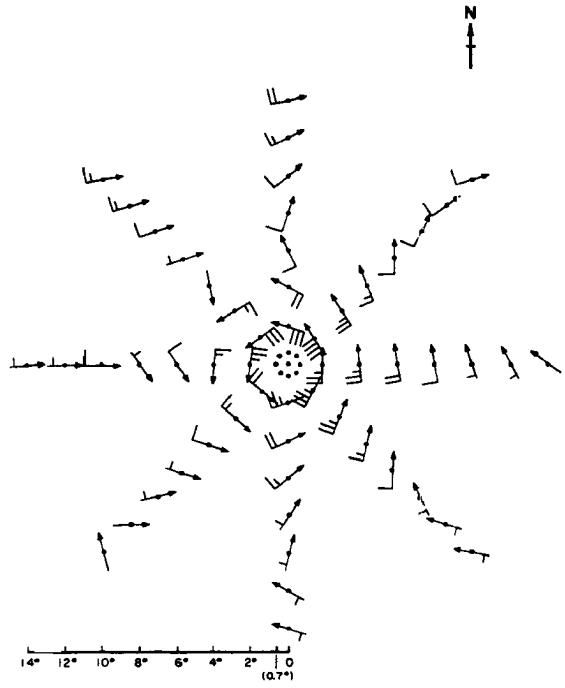

Fig. 3.51. Same as Fig. 3.50 for 500 mb.

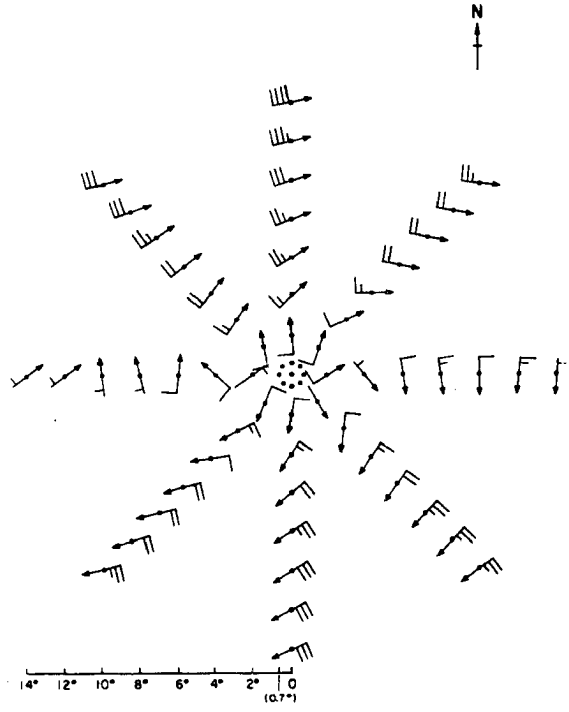

Fig. 3.52. Same as Fig. 3.50 for 150 mb.

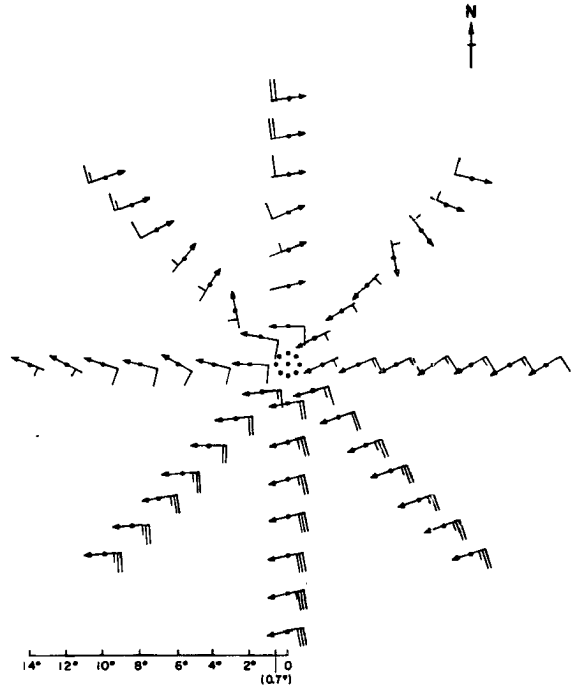

Fig. 3.53. Same as Fig. 3.50 for 100 mb.

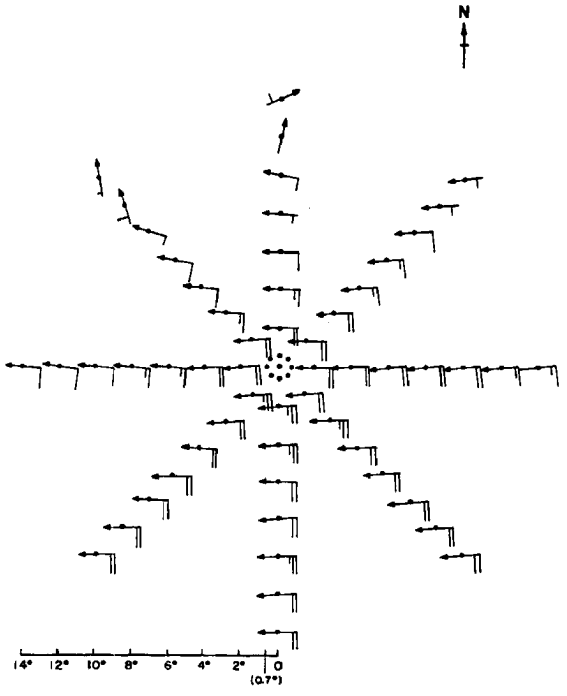

Fig. 3.54. Same as Fig. 3.50 for 70 mb.

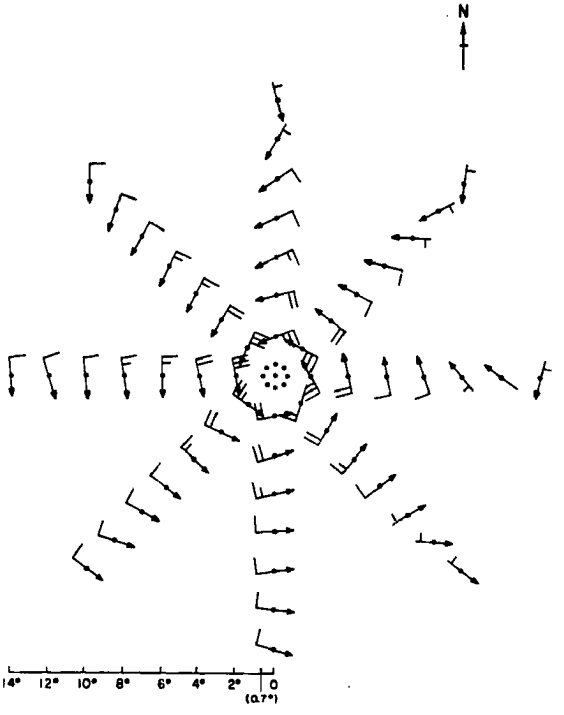

Fig. 3.55. Total winds at 950 mb in moving geographical coordinates (MOT), (knots).

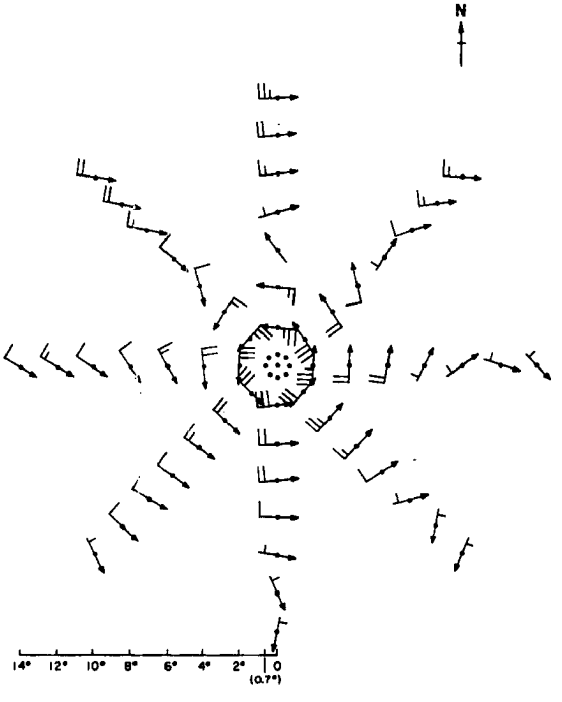

Fig. 3.56. Same as Fig. 3.55 for 500 mb.

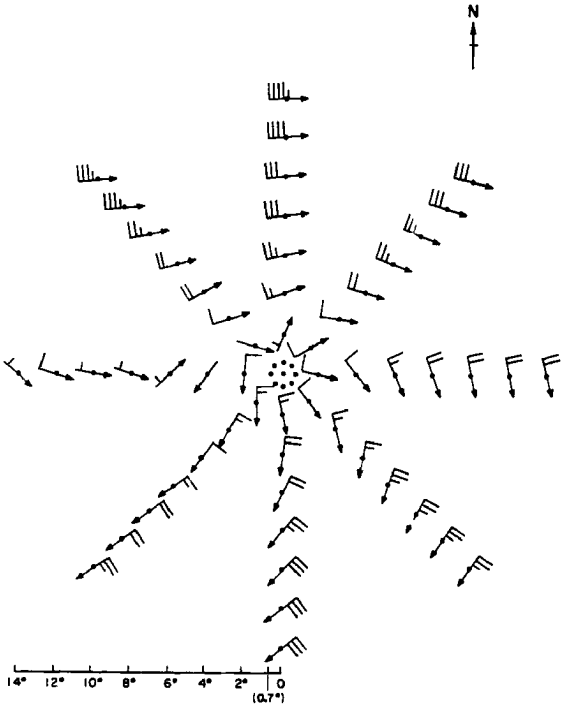

Fig. 3.57. Same as Fig. 3.55 for 150 mb.

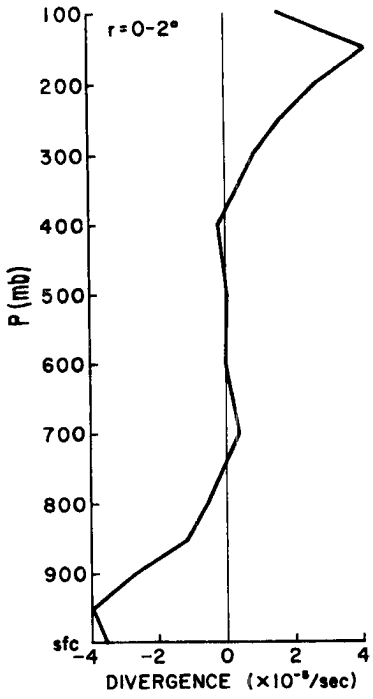

Fig. 3.58. Divergence (0-2°) for mean steady state typhoon.

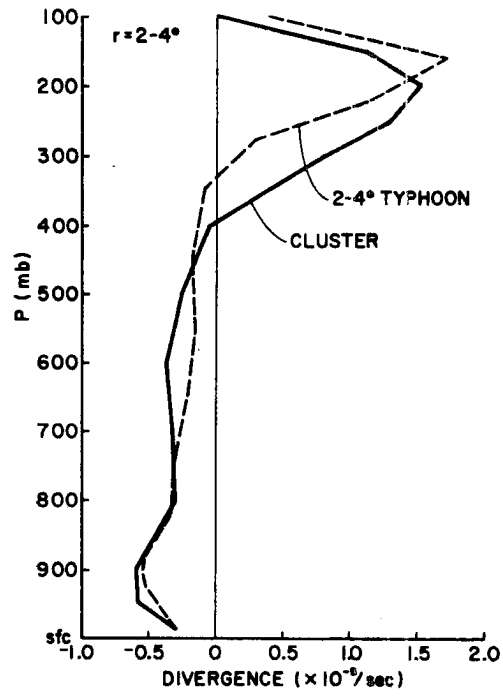

Fig. 3.59. Divergence for 2-4° region of typhoon and 0-2° region of steady state cloud cluster (Ruprecht & Gray, 1974).

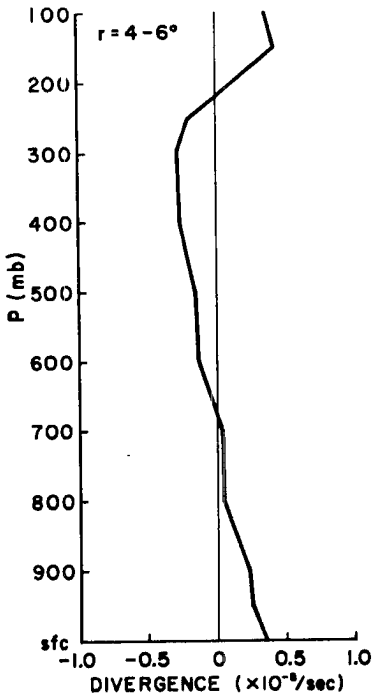

Fig. 3.60. Divergence (4-6°) for typhoons.

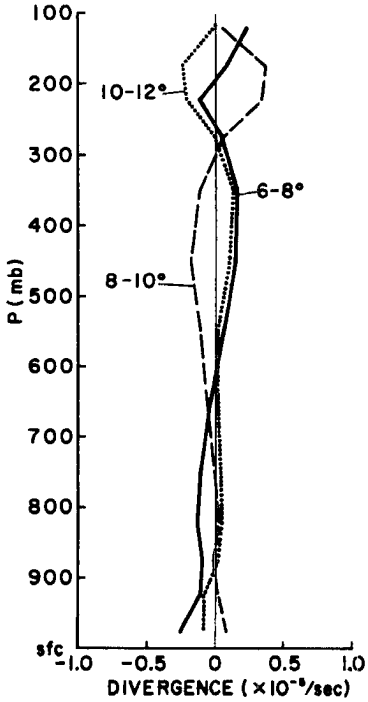

Fig. 3.61. Same as Fig. 3.60 for 6-8°, 8-10° and 10-12°.

Strong divergence occurs in the 300-100 mb outflow layer. This profile is remarkably similar to the composite divergence profile of N.W. Pacific cloud clusters (Ruprecht & Gray, 1974), which is also shown. The only significant difference is the higher level of maximum divergence associated with the hurricane. Similar divergence profiles have been observed for cloud clusters in the Pacific by Williams & Gray (1973), in the Atlantic (Ruprecht & Gray op. cit.), and for Pacific easterly wave troughs (Reed & Recker, 1971). The relationships between convection and large scale vertical motion fields are discussed in detail in the moist static energy analysis of Chapter 6.

The 4-6^{o} radial band shows mean divergence below 800 mb with convergence from 700-250 mb (Fig. 3.60). Divergence is indicated above 250 mb. The values are not large, but they do indicate a region of general subsidence through most of the troposphere. This radial band is the approximate location of the clear moat area which typically surrounds tropical cyclones.

Beyond 6^{o} radius divergence is quite weak and no clear patterns are evident (Fig. 3.61). Most of the variations from zero in these curves are probably the result of small errors in the radial wind field. An average over the 6-12^{o} region would show virtually no divergence at any level. It seems that the region beyond 6^{o} radius is relatively typical of undisturbed tropical conditions.

3.6 Vertical Motion

A 2-dimensional cross section of the 0.7-12^{o} vertical motion field is shown in Fig. 3.62. Analysis of the inner core region is excluded. (The vertical motion in each radial band is discussed in more detail

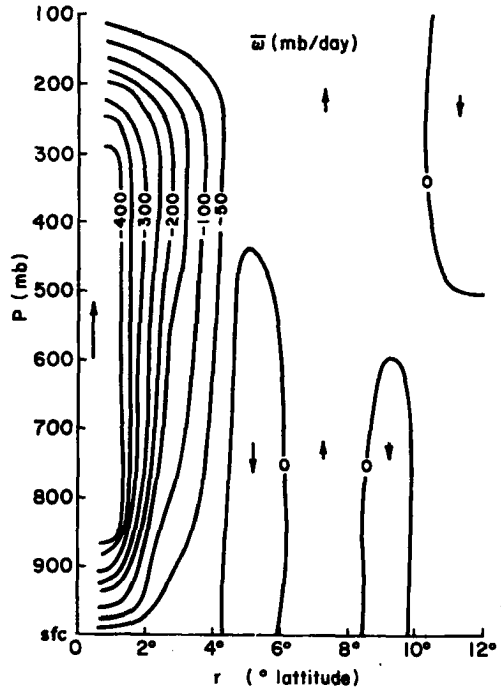

Fig. 3.62. Vertical motion from 0.7-12° for mean steady state typhoon, (mb/day).

in the energy budget analyses.) Strong upward vertical motion exists inside about 4° radius. From 4-6° there is moderate subsidence below 400 mb indicating the mean location of the moat region. Beyond 6° radius vertical motions are weak as evidenced from the divergence profiles. There is no evidence of the mean subsidence at these outer radii reported by Izawa (1964). The average vertical motion for the 6-12° band is nearly zero at all levels.

3.7 Vorticity

Relative vorticity (ζ) is determined from:

$$\zeta = \frac{V_\theta}{r} + \frac{\partial V_\theta}{\partial r} \qquad (3.1)$$

In regions of cyclonic flow, the curvature term is positive. The shear term is negative outside the radius of maximum winds. Since vorticity is defined by both the curvature and shear of the wind, it cannot be determined from individual soundings. Therefore, ζ is computed from the mean wind field.

Vertical profiles of relative vorticity at 2-10° radii for the mean steady state typhoons are shown in Fig. 3.63. The 2° profile is only an estimate. There is insufficient data inside 2° radius to allow accurate determination of the shear of the tangential wind, so inner radius flight data from Gray & Shea (1973) is used. Their data for the radius of maximum winds + 25 mi. is also shown. It is apparent that vorticity decreases with height at all radii. Vorticity also decreases with

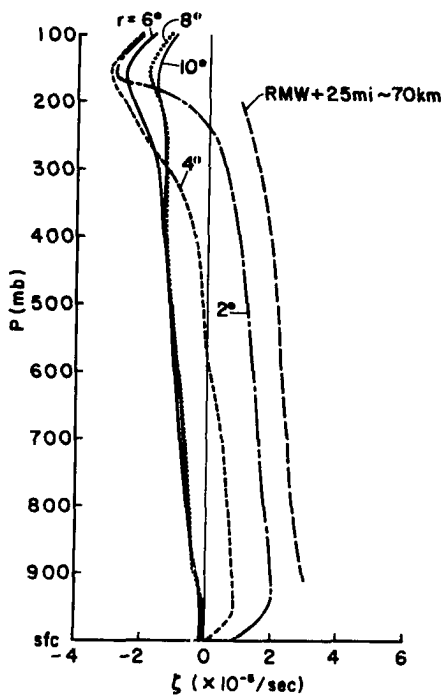

Fig. 3.63. Relative vorticity at r=2°, 4°, 6°, 8° and 10°. Also shown are values for radius of maximum winds (RMW) + 25 miles from Gray & Shea (1973), (x 10^{-5}/sec).

increasing radius except in the outflow layer where the reverse is usually true. By way of comparison the vorticity profile for the eyewall region found by Gray & Shea is shown in Fig. 3.64. They found that vorticity decreased only slightly with height and that it decreased with radius at all levels outside the radius of maximum winds. However, since they used only aircraft data, their upper level wind resolution was poor.

It is interesting to note the negative relative vorticity field at all levels from 6-10° radius which surrounds the strong positive vorticity region at the center. It appears that the cyclone acts to concentrate synoptic scale vorticity at its center.

The relationship of low level vorticity to boundary layer convergence is of interest in light of the CISK hypothesis. That theory proposes a direct correlation between frictional convergence and positive

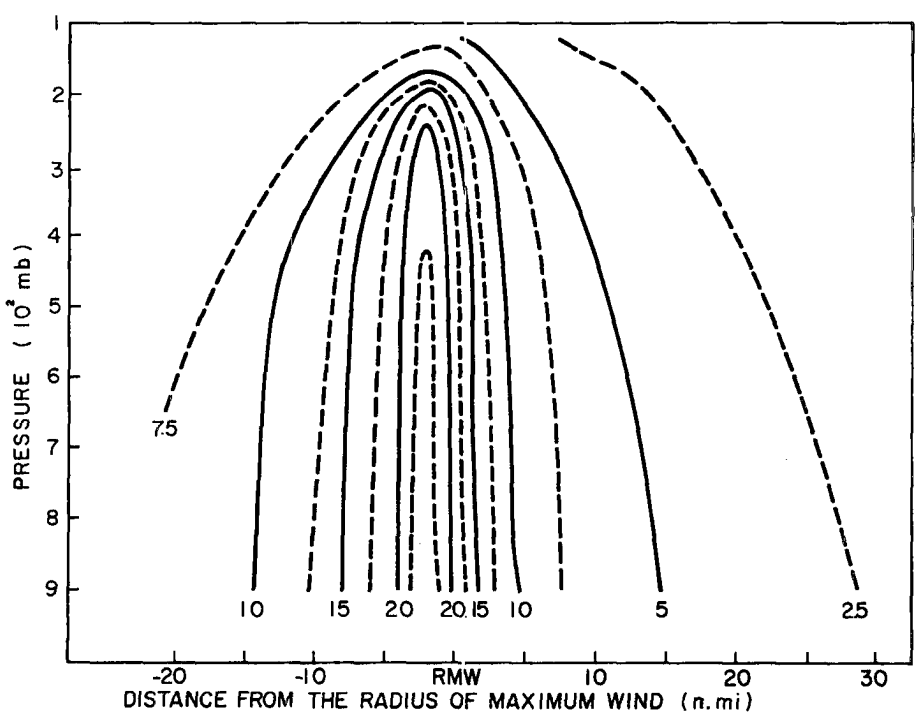

Fig. 3.64. Relative vorticity in eye/eyewall region from Gray & Shea (1973), (x 10^{-5}/sec).

low level relative vorticity. Table 3.1 shows the mean surface to 950 mb relative vorticity and convergence for each radial band from 0.7-8° radius. Positive relative vorticity and convergence are well correlated from 0.7-4°, but from 4-10° they are negatively correlated (although the values are small). It is possible that the major convective activity in the outer regions occurs in localized regions of positive low level vorticity while the large scale exhibits negative vorticity. CISK may well be applicable in such regions. Since the feedbacks between convection and low level convergence are probably substantial, the mean vorticity and convergence values over a large area containing several convective and non-convective regions may not show good agreement. Whether or not low level vorticity and convergence are applicable on the large scale to which CISK is usually applied is an open question. The crucial unsolved problem is to determine how a large vorticity field can organize itself into the small intense regions of boundary layer convergence required for Cb and squall line scale convection.

TABLE 3.1

Boundary Layer (Surface - 950 mb) Relative Vorticity and Convergence
Units = 10^{-5}/sec

	0.7-2°	2-4°	4-6°	6-8°	8-10°
$\overline{\zeta_r}$	∿2.50	1.50	.20	-.11	-.12
$-\overline{DIV}$	4.22	.39	-.27	.25	.10

(positive values denote convergence)

3.8 Comparison With Earlier Studies

A summary of the more important differences between the wind fields observed in this study and those of the earlier and smaller Jordan (1952), Hughes (1952), Miller (1958b) and Izawa (1964) studies follows. Miller studied Atlantic hurricanes while Izawa composited N.W. Pacific typhoon data, and Jordan and Hughes used data from both regions. Hughes presents data only for the 1000 ft. level.

Tangential Winds. The studies are in rather good agreement regarding the low level cyclonic flow. The largest discrepencies lie in the structure of the upper level anticyclone. The anticyclonic flow of this study is generally stronger and deeper than those reported by Izawa and Miller. The strongest anticyclonic winds occur in relatively small but intense outflow jets. Since the earlier studies had fewer soundings per unit area than the present one, they may have smoothed over some of the strongest winds considering them to be anomalous values.

Radial Winds. As previously stated, none of the previous studies were able to achieve accurate multilevel radial wind profiles. As a result, differences between the present and the previously reported radial wind fields are substantial.

In addition to the well documented back to front flow-through in the middle and lower troposphere (front to back when storm motion is subtracted), there is a left to right flow-through averaging 1½-2 m/s in the middle troposphere (800-300 mb). This is not shown in the Miller or Jordan data and is much weaker in Izawa's data.

The mean outflow jets are notheast and southwest of the storm center and are readily seen in geographical coordinates. They are not well defined when computed with respect to the direction of storm

motion. Since all of the previous studies composited in the latter reference frame, they do not show the strong persistent assymetries in the outflow velocities.

The most important radial wind feature discovered in the present study is the deep inflow. In general most previous works have neglected inflow above the boundary layer. This study shows substantial middle-level inflow occurring below 300 mb from 4-10° radius.

Divergence. Since the two dimensional divergence is derived from the radial winds, there are substantial differences between the various observed divergence profiles. Vertical motion differences are obvious reflections of the divergence fields and are not discussed here. The present study shows strong low level convergence and upper level divergence inside 2° and is in fair qualitative agreement with the Izawa study for that region. From 2-4°, however, a deep level of nearly constant convergence and an intense upper level divergence layer are indicated here while Izawa showed only a weak convergent layer near the surface and deep divergence aloft.

Beyond 6° Izawa shows divergence at nearly every grid point (his data is not mass balanced). The current data set shows a mean moat region from 4-6° with low level divergence, middle level convergence and some upper level divergence. No clear patterns are discernible beyond 6° radius.

The Miller divergence fields are presented only in plan views and are not directly comparable. Hughes shows convergence only inside about 2° radius at the 1000 ft. level.

Relative Vorticity. From 4° outward the 2-dimensional vorticity field agrees well with the findings of Izawa and Miller. However, their

vorticities inside 2^{o} seem much too high. Izawa's 1^{o} values are about the same as eyewall cloud vorticities reported by Gray and Shea (1973). Miller's 1^{o} values are only about half of Izawa's but still substantially higher than reported by Gray and Shea. Jordan's vorticity field is in good agreement at inner radii but shows positive vorticity in the boundary layer out through 6^{o} radius. Hughes shows positive 1000 ft. level vorticity through 5^{o}. The present study shows negative relative vorticity in the boundary layer at 6^{o} and outward.

4. DIURNAL VARIATIONS

The diurnal variations in deep cumulus convection and precipitation over the tropical oceans are well documented as summarized in Jacobson and Gray (1976). There are early morning maxima of these two quantities and late afternoon or early evening minima. Most deep convection over the tropical oceans occurs in organized cloud clusters which exhibit strong diurnal variations in their convergence/divergence profiles in agreement and phase with the convective variations (Williams & Gray, 1973; Ruprecht & Gray, 1974).

It is assumed that diurnal changes in the net radiational cooling differences between the cloud clusters and their relatively clear environments force the enhanced lower and middle tropospheric convergence and upper level divergence in the morning relative to early evening (Jacobson & Gray, op.cit.). Since tropical cyclones are covered with a thick cirrus cloud deck surrounded by a relatively clear area, it is probable that a diurnal radiational forcing function of similar magnitude acts upon these fully developed storms. One would expect the diurnal response of the storm to the forcing to be less dramatic than the response of the cluster due to the much more intense dynamics and energetics occurring in the tropical cyclone. This proves to be the case. Nevertheless, a few differences between 00Z soundings ($\sim$ 1000 local time - L.T.) and 12Z soundings ($\sim$ 2200 L.T.) are observed for the mean N.W. Pacific typhoon.

4.1 Central Pressure and Winds

No significant diurnal variations in the central pressure or maximum reported winds occur. The data does show slightly greater mean

wind speeds from 1-5° radius in both the inflow and outflow layers at 00Z, but the differences are only about 5-15% (∿ 1 m/sec) and are not statistically significant. No diurnal wind speed variations are observed in the middle troposphere. No significant diurnal variations in the radial wind profiles are observed. The total mass flux through the active storm region (0-4°) is about the same at 00Z and 12Z.

4.2 Precipitation

Due to the very large diurnal rainfall variations found in cloud clusters, up to 21 years of hourly rainfall data from 9 island stations (circled in Fig. 1.2) were analyzed for diurnal variations in typhoon precipitation. This data set is discussed in more detail in the water budget study of Chapter 5. As a storm tracked within 4° of an island station, the rainfall at the station was recorded on a grid with the storm at its center. The data was composited. Figure 4.1 shows the diurnal values of the total rainfall rate - defined as the total rainfall divided by the total number of hours that storms were on the 0-4° grid. A small but noticeable maximum occurs at 1000-1200 local time with a minimum at about 1800 local. This is in agreement with observed N.W. Pacific cloud cluster variations which show much stronger precipitation at 00Z (∿ 10LT) than at 12Z (∿ 22 LT) (Ruprecht & Gray, op.cit.). The variations in typhoon rainfall are much smaller, as expected.

Figure 4.2 shows the diurnal variations of total recorded rainfall which occurred during light rain episodes (< 0.2 in/hour) and during heavier rain episodes (≥ 0.2 in/hours). It is clear that the diurnal rainfall variation is due almost entirely to increased amounts of heavy rain falling in the late morning hours. Virtually no diurnal variation

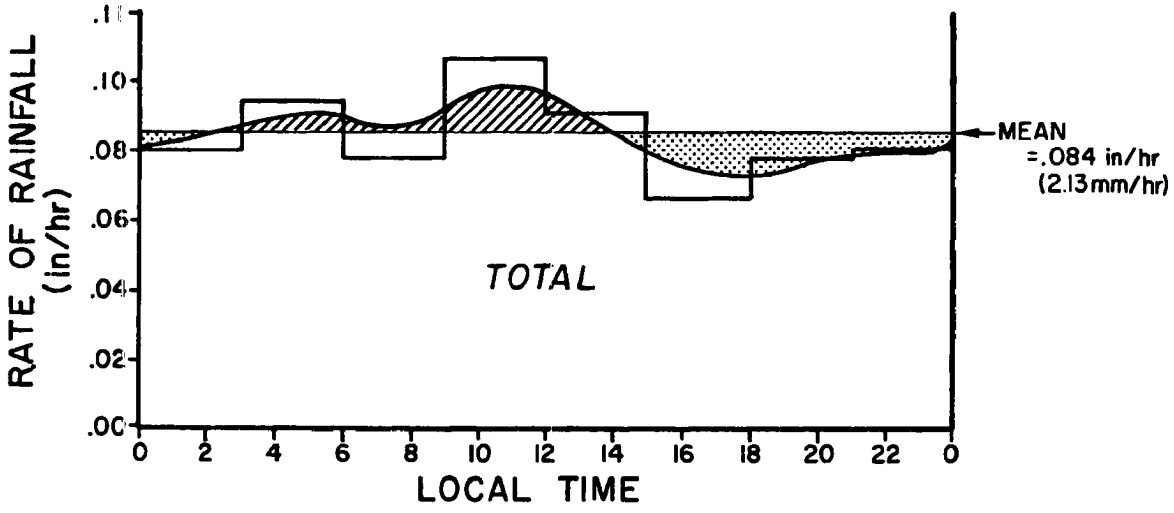

Fig. 4.1. Diurnal variation of total rate of rainfall (total rainfall divided by time that storm was within 4° latitude of station) for 9 Pacific island stations. Units = in/hour.

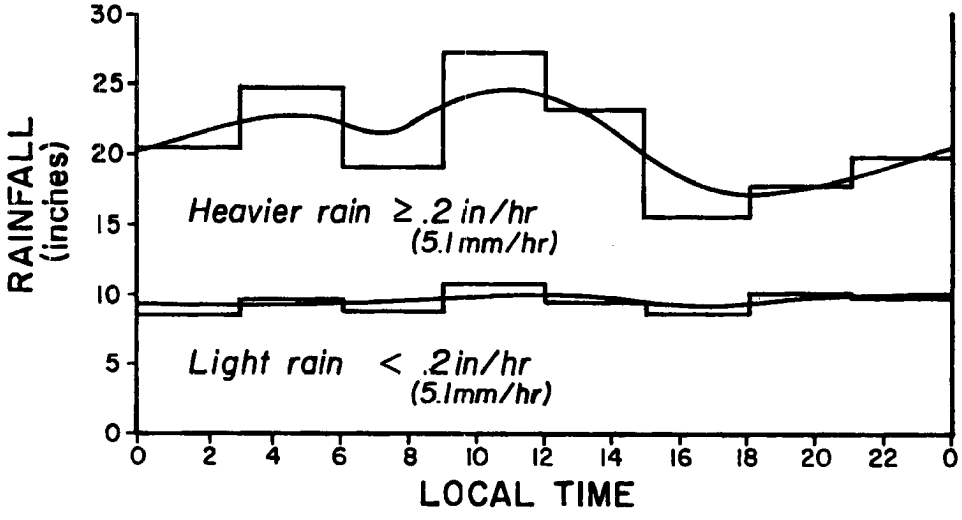

Fig. 4.2. Diurnal variations of total rainfall during heavier rain episodes (≥ 0.2 in/hour) and during light rain episodes (< 0.2 in/hour) for 9 Pacific islands. Units = inches.

in light rainfall is observed. This is in close qualitative agreement with the results of previous precipitation studies.

Figure 4.3 shows the diurnal variations of the percentages of the total time during which various rainfall rates were recorded. Once again, it can be seen that the 1000-1200 LT precipitation maximum results from increased frequencies of heavy rainfall episodes. Similarly, the late afternoon minimum appears to result from decreased numbers of heavy rainfall episodes.

It appears that typhoons have a small diurnal rainfall variation with a maximum in the late morning (1000-1200 local) and a minimum in the late afternoon (1800 local). The variation is due almost entirely to differences in the amounts of heavy rainfall recorded at these times.

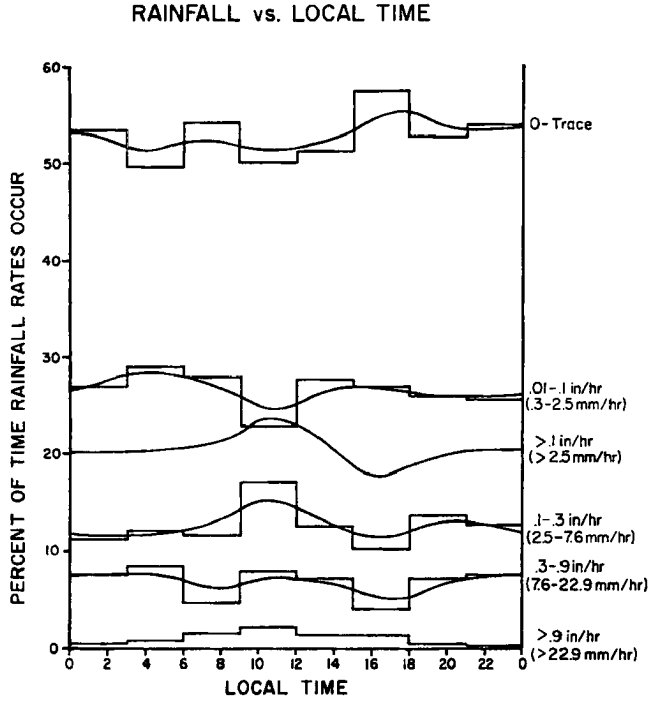

Fig. 4.3. Diurnal variations of the percentage of the total time during which various rainfall rates were recorded for 9 island stations.

These findings are in close qualitative agreement with various studies of N.W. Pacific cloud cluster rainfall.

4.3 Temperature

Observed diurnal temperature differences ($T_{00Z}-T_{12Z}$) are shown in Fig. 4.4 for 2^{o} and 6^{o} radius. The 2^{o} data are well within the active convective region, and most of these soundings are underneath a dense cirrus shield (mean top ∿150 mb). The 6^{o} data are representative of soundings well beyond the active convective storm region. Neither radial band shows any significant diurnal variation from the surface through 600 mb (the surface variation at 6^{o} is a heat island effect). Upper tropospheric data (above 300 mb) are subject to increasingly large instrument errors with height. The observed daytime temperatures at these heights are too high due to overheating of the instrument package in the rarified air (Foltz, 1976). Thus, the observed temperature variations above 300 mb or so may not be very reliable. The 2^{o} region, however, shows a morning minus evening temperature anomaly of 0.5-1.0°C from 500 mb to 300 mb. Since most of the soundings in this region are beneath the dense cirrus shield, the measurement errors should be minimal. Note that the 2^{o} anomaly is much larger than the 6^{o} anomaly which occurs in a relatively clear region.

It appears that tropical cyclones may experience a diurnal temperature variation from about 500 mb to a least 300 mb. Temperatures are greater at 00Z (∿ 10 LT) than 12Z (∿ 22 LT). The higher temperatures coincide with the observed rainfall maximum near 00Z and may be related directly to the amount of deep convective activity or extra solar absorption. Several studies have concluded that the maximum large scale warming resulting from deep tropical convection occurs near 300-400 mb

(Lopez, 1968; Yanai, 1963, 1969; Zipser, 1964; Zehr, 1976).

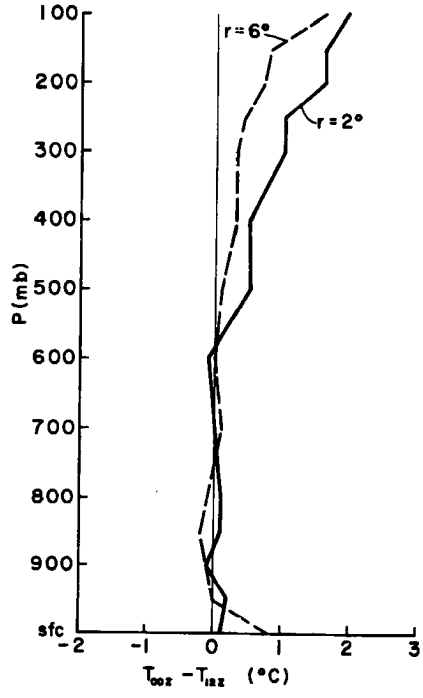

Fig. 4.4. Diurnal temperature differences (T_{00Z} minus T_{12Z}) at r = 2^{o} and 6^{o}.

5. WATER BUDGET

Tropical cyclones have long been known for the intense precipitation associated with their inner convective regions. Rainfall above seasonal norms occurs over a large area, and tropical storms can be an important source of precipitation in some parts of the world (Cry, 1967). Due to the basic pattern of lower and middle tropospheric inflow and upper tropospheric outflow, tropical cyclones converge large quantities of water vapor. This phenomenon is enhanced by above average surface evaporation of sea water due to high surface winds. A small part of this water vapor convergence goes into increased humidity levels in the inner storm (see Section 2.3), but most falls out as precipitation.

5.1 Vertically Integrated Water Budget

Neglecting horizontal transports of liquid water and vertical flux of q at the upper boundary, the equation for conservation of water integrated over a cylindrical volume extending from the surface to 100 mb is:

$$\int_{VOL} \frac{\partial \overline{\rho q}}{\partial t} = \int_{VOL} \overline{\nabla \cdot \rho \, \mathbf{V} q} + (E-P) \qquad (5.1)$$

E = evaporation from sea surface

P = precipitation

Steady state is assumed for this analysis (all soundings with storm central pressures $\leq$980 mb). Hence, the term on the left of Eq. 5.1 is zero. The first term on the right is the total horizontal transport of water vapor into the volume. Sample total transports ($\overline{V_r q}$) and mean circulation transports ($\overline{V_r} \cdot \overline{q}$) are shown in Figs. 5.1-5.3 for r =

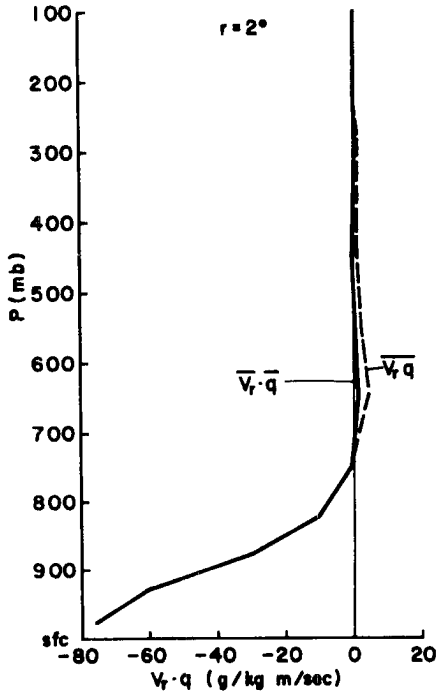

Fig. 5.1. Total horizontal transport of water vapor ($\overline{V_r\ q}$) and transport by the mean circulation ($\overline{V_r}\ \overline{q}$) at r= 2^{o}.

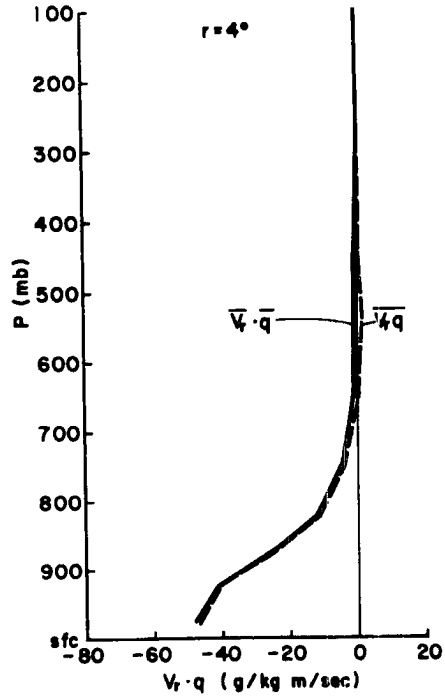

Fig. 5.2. Same as Fig. 5.1 for r = 4^{o}.

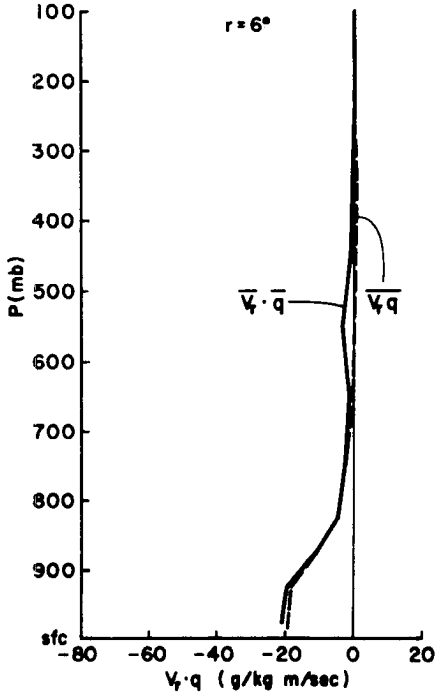

Fig. 5.3. Same as Fig. 5.1 for r = 6^{o}.

2^{o}, 4^{o} and 6^{o}, respectively. The areas between the curves represent the eddy fluxes of q. These eddy fluxes do not appear large, but they amount to about 5-15% of the total mean circulation influxes at most radii. The horizontal fluxes of q lead to observed convergences of water vapor in the radial bands as shown in Table 5.1.

TABLE 5.1

Convergence of Water Vapor due to Horizontal Fluxes ($\frac{gm}{cm^2 day}$)

Radius	$0-2^{o}$	$2-4^{o}$	$4-6^{o}$	$6-8^{o}$	$8-10^{o}$	$10-12^{o}$
Convergence of q	6.66	1.20	-.68	.08	-.13	-.14

The second and third terms on the right side of Eq. 5.1 are the evaporation from the sea surface and the precipitation. Either can be estimated to yield the other as a residual. Evaporation is a difficult term to estimate accurately due to uncertainties concerning surface wind values, sea surface temperatures, and drag coefficients. Evaporation estimates based on moist static energy budget analyses are discussed in the next section. In this water budget study precipitation measurements from Miller (1958a) and an unpublished CSU study are used.

Precipitation data over Florida for 16 hurricanes are shown in Fig. 5.4 (Miller, 1958a). Observed precipitation amounts are assumed to exhibit only very small orographic effects due to the flat nature of the Florida terrain. Values are corrected for measurement errors caused by high winds. Also shown in Fig. 5.4 are rainfall amounts around N.W. Pacific typhoons as observed in an unpublished Colorado State University report to NOAA by Gray, Frank and George (1975). These

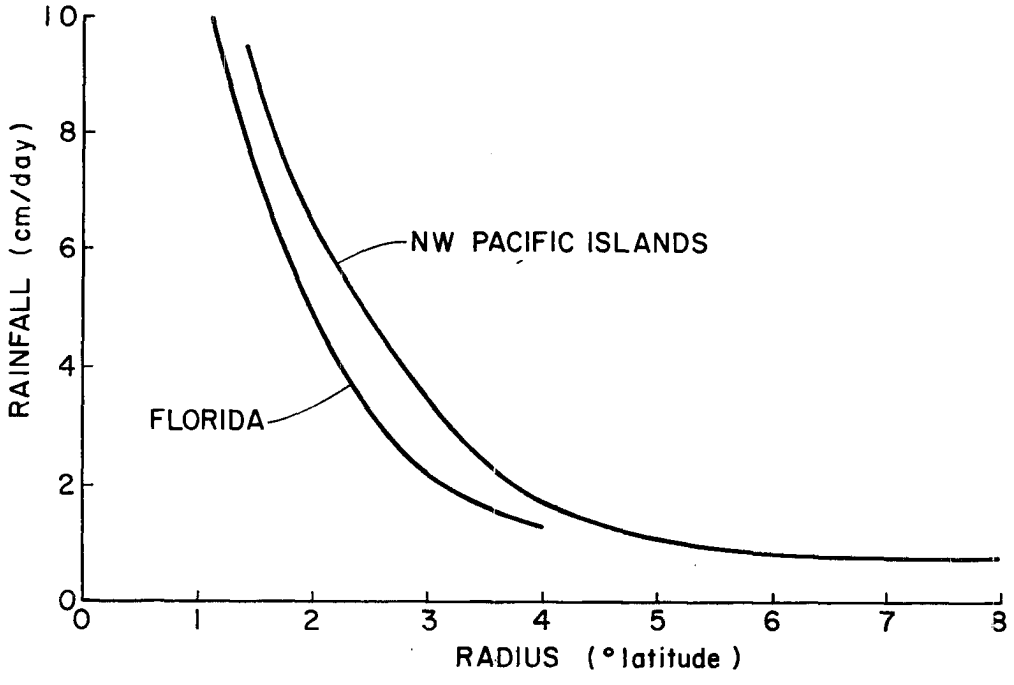

Fig. 5.4. Observed precipitation around tropical cyclones from Florida (Miller, 1958a) and from N.W. Pacific Islands (CSU study, 1975).

Pacific observations are based on up to 21 years of hourly data from 9 small island stations and 12 years of 12-hourly data from 4 small Japanese island stations. For these latter stations the duration of rainfall within the 12 hour period is also recorded to allow estimates of rainfall rates. The stations used in the Pacific study are shown in Tables 5.2 and 5.3 with the periods of data availability. These stations are circled on the data network map of Fig. 1.2. Unlike the Florida data, the Pacific island rainfall observations probably exhibit significant local orographic influences due to the elevated terrain on some of the islands, and they are not corrected for high wind measurement errors. However, the data sets agree rather well. It is unclear how much of the

higher precipitation observed in the Pacific is orographic and how much results from the greater mean sizes and intensities of storms found there.

TABLE 5.2

Hourly Rainfall Data Stations

Station	Period For Which Data Were Available	Location
Guam	Feb 1957 - Mar 1974	13°N, 145°E
Wake	Jul 1957 - Mar 1974	19°N, 167°E
Koror	Spt 1959 - Mar 1974	7°N, 134°E
Yap	Apr 1960 - Mar 1974	10°N, 138°E
Truk	Jul 1959 - Mar 1974	7°N, 152°E
Majuro	Apr 1958 - Mar 1974	7°N, 171°E
Ponape	May 1958 - Mar 1974	7°N, 158°E
Marcus	Oct 1963 - Jun 1968	24°N, 154°E
Eniwetok	Mar 1961 - Oct 1963	11°N, 162°E

TABLE 5.3

12-Hourly Rainfall Stations

Station	Data Period	Location
Minamidaitojima	1962-1973	26°N, 131°E
Miyakojima	1962-1973	25°N, 125°E
Hachijojima	1962-1973	33°N, 140°E
Tanegoshima	1962-1973	31°N, 131°E

The Florida data is assumed to be the more reliable data set for mean rainfall amounts inside 4^{o}. It is also assumed that from $4\text{-}12^{o}$ the storms do not increase oceanic precipitation significantly from seasonal norms, so a smoothed figure of 0.70 cm/day is used based on analysis of the Pacific data at large radii. The resulting precipitation amounts are shown in Table 5.4.

TABLE 5.4

Radius:	$0\text{-}2^{o}$	$2\text{-}4^{o}$	$4\text{-}6^{o}$	$6\text{-}8^{o}$	$8\text{-}10^{o}$	$10\text{-}12^{o}$
Precipitation (cm/day)	9.00	2.30	.70	.70	.70	.70

Assumed Precipitation Based on Data From Miller (1958a) and Unpublished N.W. Pacific Data.

When the smoothed precipitation values of Table 5.4 are combined with the water vapor convergence values of Table 5.1, the resulting required evaporation may be determined (Fig. 5.5). These values seem realistic except for an apparent overestimate of evaporation from $4\text{-}6^{o}$ and an underestimate from $6\text{-}8^{o}$, probably due to a small error in the observed radial wind profile at 6^{o}. This may have lead to slightly too much low level divergence of q from $4\text{-}6^{o}$ and slightly too much convergence from $6\text{-}8^{o}$.

It is interesting to note that while about 75% of the observed $0\text{-}2^{o}$ precipitation results from inward water vapor advection, nearly 65% of the $0\text{-}6^{o}$ precipitation may be attributed to evaporation within that area. The area weighted evaporation from $0\text{-}6^{o}$ is about 1.4 cm/day, although this may be .2-.3 cm too high due to the probable overestimate

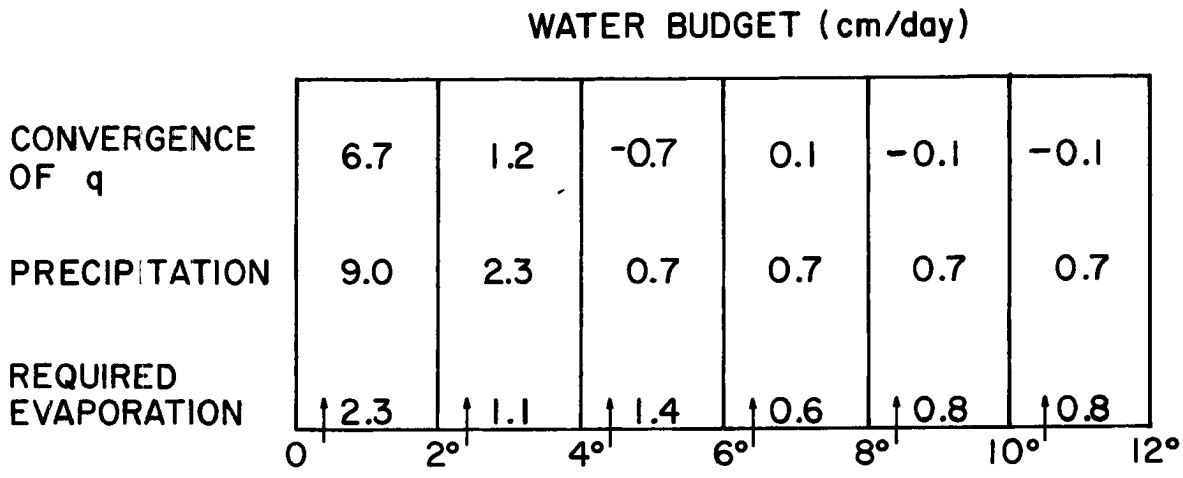

Fig. 5.5. Water budget for 0-12° region. Evaporation values shown are the amounts required to achieve balance.

of the 4-6° evaporation. Since mean typhoon season evaporation is about equal to the seasonal precipitation (∿.7 cm/day), approximately 50% of the total 0-6° evaporation may be assumed to result from the increased wind speeds associated with tropical cyclones. About 1/3 of the 0-6° storm precipitation is due to this anomalous sea surface evaporation. The important role of the sea surface in the storm's water budget and hence in its energetics is obvious. This phenomenon helps explain the rapid decay of tropical cyclones as they move over substantial land areas.

5.2 Computation of Evaporation Coefficient (C_E)

The computed evaporation values of Fig. 5.5 are plotted in Fig. 5.6. The mean 900 mb wind is also plotted (right hand scale). The

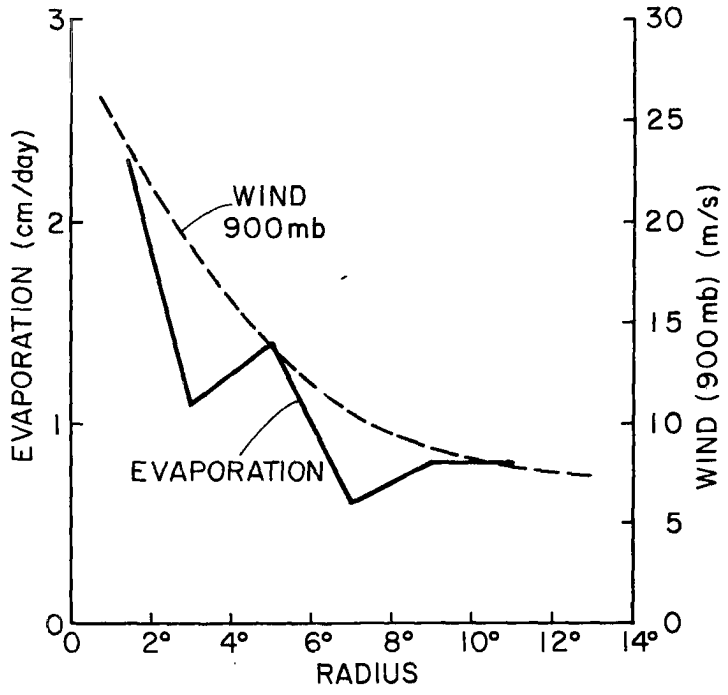

Fig. 5.6. Evaporation from Fig. 5.4 (cm/day) and 900 mb wind speeds (right hand scale, m/sec).

agreement in shape between the two curves is fairly good. Assuming a linear relationship between wind and evaporation, such as the classical bulk aerodynamic formula

$$E = \rho C_E \bar{V} \quad (q_s - q)$$

E = evaporation
ρ = density
C_E = evaporation coefficient
V = 10 meter wind speed
q_s = saturated specific humidity of sea surface
q = specific humidity of air at the surface

and assuming the 900 mb winds to be roughly proportional to 10 meter winds over the open sea, Fig. 5.6 implies that C_E $(q_s - q)$ is relatively constant.

Although the specific humidity of the air at each radius can be determined from the data composites, information concerning sea surface temperatures in and around typhoons is understandably scarce. Analysis of climatological sea surface temperature data (Robinson and Bauer, 1971) and composited surface temperatures indicates that as a first approximation $(q_s - q)$ can be considered constant inside 6^o radius. A value of $(q_s - q) \sim 4.8 \times 10^{-3}$ is chosen. This figure is probably reasonable except in regions of significant upwelling and in the extreme inner core where the surface relative humidities appear to approach 95-100%.

Outside 6^o radius the sea surface temperatures are assumed to be 1^oC warmer than the measured air temperatures, and $(q_s - q)$ values are computed accordingly. Values of $(q_s - q)$ are shown in Table 5.5.

TABLE 5.5

$q_s - q$ ($\times 10^{-3}$)

	0-2°	2-4°	4-6°	6-8°	8-10°	10-12°
$(q_s - q)$ $\times 10^{-3}$	4.8	4.8	4.8	5.0	5.0	5.0

Values of the evaporation coefficient computed for each radial band are shown in Fig. 5.7. The approximate mean C_E for 900 mb winds is 1.7×10^{-3}. There is no clear evidence of a variation in C_E with wind speed. Ooyama (1969) found that a constant value of C_E of 1.5×10^{-3} applied to the gradient level winds gives a realistic simulation of tropical cyclone development in his model.

A second technique can be used to evaluate surface evaporation in typhoons. Using a method outlined by Yanai et al. (1973), the

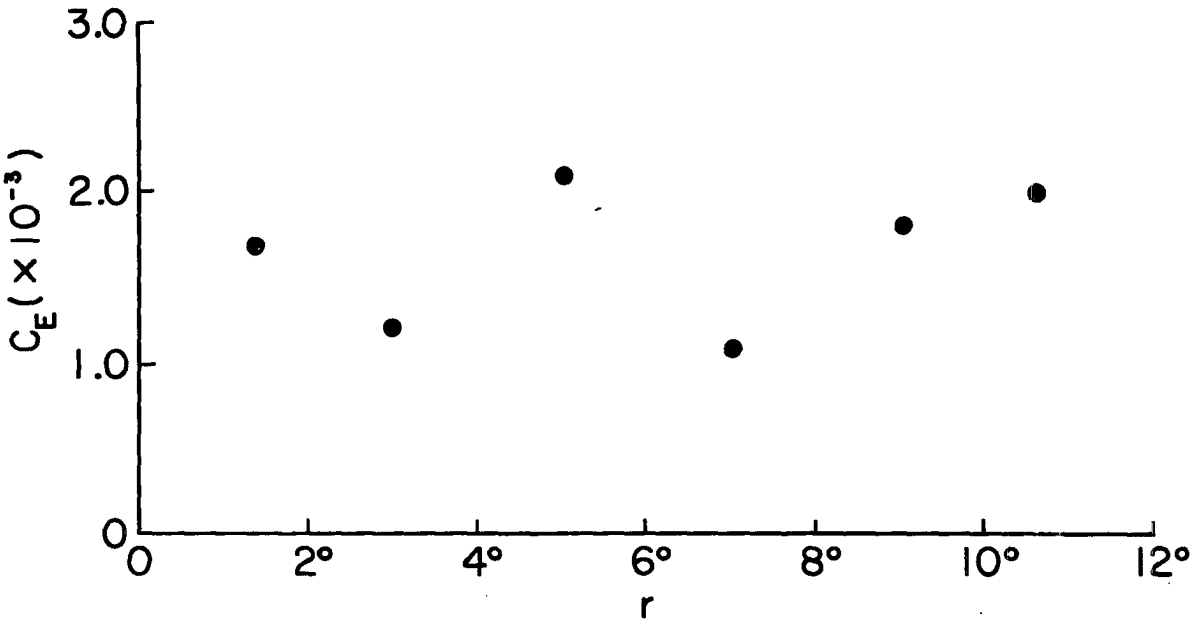

Fig. 5.7. Evaporation coefficients (C_E) computed from Eq. 5.2.

horizontal fluxes of moist static energy are computed. Using assumptions of the radiative energy flux, the transfer of sensible plus latent heat energy from the sea to the air can be determined as a residual. By making assumptions concerning conditions at the air-sea interface one can assume a Bowen ratio and thereby estimate the amount of total sea to air energy flux which occurs as sensible heat flux and the amount which is due to evaporation. Surface fluxes derived from these moist static energy budget considerations are in satisfactory agreement with the fluxes derived in this section and are discussed later.

5.3 Other Characteristics of Typhoon Rainfall

The previously discussed N.W. Pacific rainfall data are further analyzed to determine the mean rainfall rates by quadrant for the 0-4° radius area. Although the total amounts of rainfall from this data set are probably less accurate than those in the Miller study due to local orographic effects, the horizontal distribution is probably better. Orographic anomalies are all positive for small island stations while the orographic influence of Florida upon precipitation may result in persistent maxima and minima which largely cancel in the mean. The combined 9 island hourly data and Japanese island data are shown in Fig. 5.8. No corrections are made for orographic effects or measurement errors. The values shown are for the 0-2° band and the 2-4° band for the four quadrants (the grid is aligned with the direction of storm motion toward the top of the page). Also shown are the radial band averages for all four quadrants. No striking asymmetries are observed, but rainfall does seem to be highest in the right rear quadrant. This finding contradicts earlier estimates of strong rainfall maxima in the right front quadrant (Cline, 1962; Shoner, 1957). Since most previous tropical cyclone rainfall studies have been performed for storms at or near continental landfall, it is possible that the previously observed right front quadrant maximum is orographic in origin due to onshore flow. Under such conditions supressed convection would be expected in the front left quadrant where off-shore flow prevails. Dunn and Miller (1964), have proposed that the precipitation pattern of low latitude storms is symmetrical with a right front quadrant maximum developing as the storms move poleward.

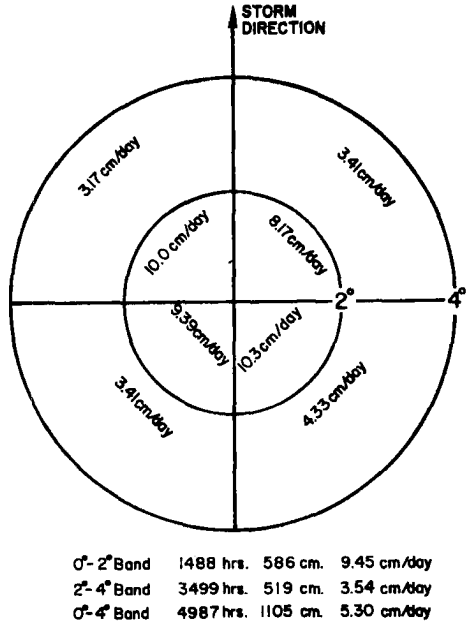

Fig. 5.8. Mean precipitation around tropical cyclone based on hourly data from 9 island stations and 12 hourly-data from 4 Japanese island stations.

The hourly rainfall data are also used to determine the frequency and intensity of rainfall occurrences during typhoon passage near an island station. Table 5.6 shows the percentage of the total time in which each rainfall rate is recorded for each radial band.

It is interesting to note the relatively small percentage of the time that moderate to heavy rains ($\geq$ .1 in/hour) fall. Such rainfall rates are recorded only 35% of the time in the highly active 0-2^{o} region and but 17% of the time in the 2-4^{o} band. Outside of 4^{o} radius rainfalls of this intensity are not often recorded (3-6% of the time). Substantial amounts of light rain (.01-.10 in/hour are recorded inside 6^{o}. It is possible that some of this rain is due to orographic effects resulting from elevated terrain, strong winds, and very high humidities. The above average rainfall recorded in the 4-6^{o} band seems to result

TABLE 5.6

Rainfall Rates

Rainfall Rate in/hour)	Percent of Total Storm Passage Time						
	0-2°	2-4°	4-6°	6-8°	8-10°	10-12°	12-14°
0-trace	30	59	80	87	89	89	90
.01-.1	35	24	14	10	7	7	7
.1-.3	19	11	4	2	3	2	2
.3-.9	13	5	2	1	1	2	1
>.9	3	1	<1	<1	<1	<1	<1

primarily from an above normal incidence of light rainfall and slightly above average moderate rainfall (.1-.3 in/hour). Since this area is observed to be relatively cloud free, except for occasional outer rainbands, at least part of the observed positive anomaly in precipitation may be orographic in origin.

The results of this rainfall study indicate that typhoon precipitation is primarily concentrated in localized heavy convective regions. The incidence of 2-4° band rainfall is only slightly greater than was found for N.W. Pacific cloud clusters by Ruprecht and Gray (1974). The inner core (0-2°) area shows a much larger incidence of rainy episodes than is found in cloud clusters as expected. The frequencies of moderate to heavy rainfall (>.1 in/hr) agree relatively well with the convective cloud covers inside 200 miles of ∿5% Cb and ∿25% total cumulus cloud cover reported by Malkus et al. (1961) and Gentry (1964). Diurnal variations in precipitation amounts and frequencies are discussed in Chapter 4.

6. MOIST STATIC ENERGY BUDGET

6.1 Introduction

Analysis of the moist static energy budget of a convective tropical weather system is a valuable technique for determining fluxes of sensible heat, moisture, and mass within the system (Gray, 1973; Yanai, et al., 1973). By using a spectral cloud model it is possible to analyze the cloud populations as well (Arakawa and Schubert, 1974; Nitta, 1975; Ogura and Cho, 1973; Cho and Ogura, 1974 and Yanai et al., 1976). This section analyzes the large scale fluxes of heat, moisture and mass together with radiational heating profiles and vertical boundary energy transports to solve for the required vertical eddy fluxes of moist static energy within different regimes of a mean, steady state typhoon. A simple spectral cloud model incorporating overshoot cooling, moist downdrafts, multi-level detrainment, and ice phase transitions is employed to analyze the cloud populations of these regimes.

Budgets of moist static energy are performed for 5 typhoon regions: 0-0.7° radius (eye and eyewall region), 0.7-2° (inner rainband area), 2-4° (outer convective area), 4-6° (approximate moat region), and 6-8° (assumed typical of outer regions). Due to the variations in typhoon sizes these radial bands correspond only approximately to the regimes described in parenthesis.

6.2 Method

Moist static energy (h) is defined:

$$h = C_p T + gz + Lq = s + Lq \qquad (6.1)$$

where T = temperature,

z = height

L = latent heat of condensation,

q = specific humidity, and

s = dry static energy.

For a large scale area containing an ensemble of clouds the equations of mass, heat energy and moisture continuity averaged over the area are:

$$\overline{\nabla \cdot V} + \frac{\partial \omega}{\partial p} = 0 \tag{6.2}$$

$$\frac{\partial \bar{s}}{\partial t} + \overline{\nabla \cdot sV} + \frac{\partial \overline{s\omega}}{\partial p} = Q_R + L\,(c-e) \tag{6.3}$$

$$\frac{\partial \bar{q}}{\partial t} + \overline{\nabla \cdot qV} + \frac{\partial \overline{q\omega}}{\partial p} = (e-c) \tag{6.4}$$

where V = horizontal velocity

ω = dp/dt,

Q_R = radiational heating rate,

c = condensation rate, and

e = evaporation rate.

The bar denotes time and space averaging.

Assuming that the cloud ensemble occupies only a fraction of the area being studied, the apparent heating (Q_1) and apparent moisture sink (Q_2) resulting from large scale processes may be determined following Yanai et al., (1973).

$$Q_1 = \frac{\partial \bar{s}}{\partial t} + \overline{\nabla \cdot sV} + \frac{\partial \bar{s}\,\bar{\omega}}{\partial p} = Q_R + L\,(c-e) - \frac{\partial \overline{s'\omega'}}{\partial p} \tag{6.5}$$

$$Q_2 = L\left[\frac{\partial \bar{q}}{\partial t} + \overline{\nabla \cdot qV} + \frac{\partial \bar{q}\,\bar{\omega}}{\partial p}\right] = L\,(c-e) + L\,\frac{\partial \overline{q'\omega'}}{\partial p} \tag{6.6}$$

The terms on the left sides of Equations 6.5 and 6.6 are observable quantities. For this mean steady state typhoon study $\frac{\partial \bar{s}}{\partial t}$ and $\frac{\partial \bar{q}}{\partial t}$ are almost zero. There is only very slight warming in the 100-150 mb layer and cooling in the lower troposphere (sfc-700 mb) due to the mean northward movement of the storm. Hence $\frac{\partial \bar{s}}{\partial t} \neq 0$ for these levels despite no observable intensity tendency. These changes in the mean environmental temperatures are always less than 1^{o} C per day. Horizontal fluxes of s and q are obtained by compositing individual sounding values of $V_r \cdot s$ and $V_r \cdot q$ in the manner described in section 1.4. Mean vertical fluxes are computed from the mean large scale divergence profiles and the observed s and q fields. Combining Eqs. 6.5 and 6.6:

$$(Q_1 - Q_2 - Q_R) = \frac{-\partial}{\partial p} \overline{(s' + Lq')\omega'} = -\frac{\partial}{\partial p} \overline{h'\omega'} \qquad (6.7)$$

The term on the left of Eq. 6.7 is the apparent source of h due to the large scale circulation and can be determined from conventional observations plus an estimation of Q_R. The term on the right is the vertical eddy flux of h.

Q_1 and Q_2 are measured as discussed above. Q_R is determined by applying the radiational heating profiles shown in Fig. 6.1. These profiles are derived from infrared radiational cooling profiles for cloud clusters based on Albrecht and Cox (1975) and solar warming data from Dopplick (1974). Mean daily profiles were obtained for clear skies and for dense cirrus overcast (Figs. 6.2 and 6.3). The upper levels of these profiles were adjusted slightly at radii less than 6^{o} to account for the very high humidities observed there. Similar profiles were obtained by Gray (1976) for cloud cluster and clear areas. The radiational heating profiles for the 4 regions in Fig. 6.1 were obtained by

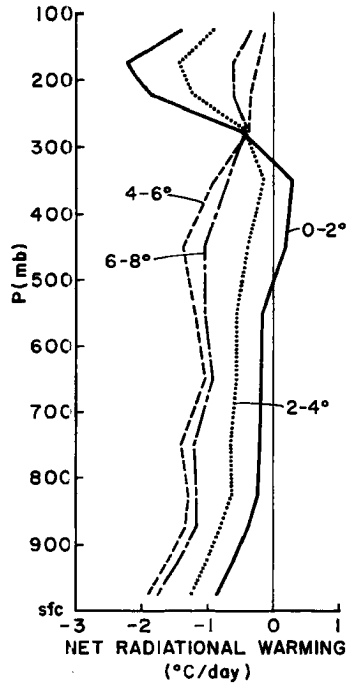

Fig. 6.1. Net radiational warming in $0-2^{o}$, $2-4^{o}$, $4-6^{o}$ and $6-8^{o}$ regions based on Albrecht and Cox (1975) and Dopplick (1974).

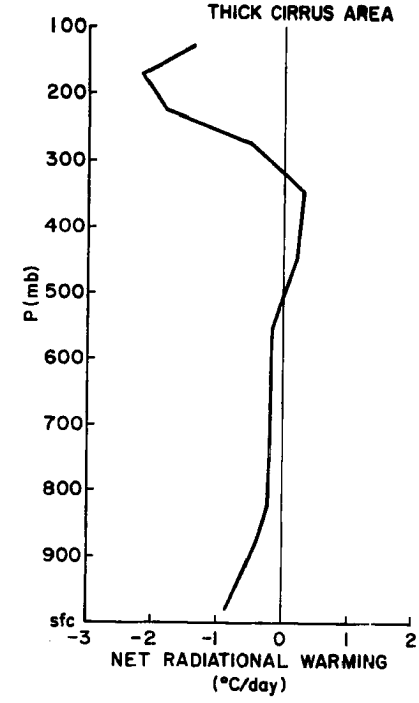

Fig. 6.2. Net radiational warming of tropical atmosphere with 100% dense cirrus cover.

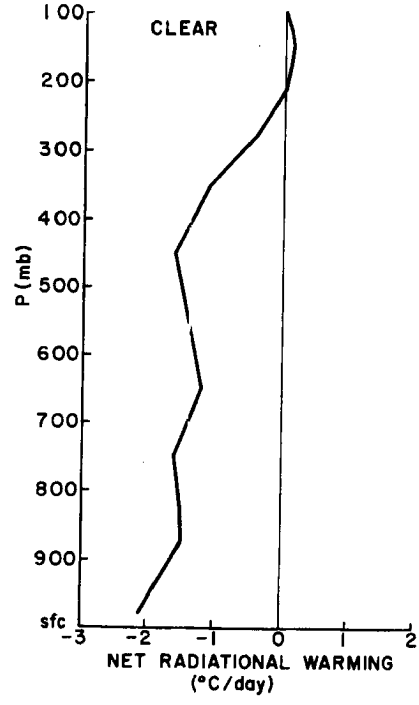

Fig. 6.3. Net radiational warming of clear tropical atmosphere.

assuming total cirrus cover inside 2^{o}, 67% cirrus cover from $2\text{-}4^{o}$, 15% cover from $4\text{-}6^{o}$, and 30% cover from $6\text{-}8^{o}$ and averaging the cirrus and clear profiles accordingly. These cloud/clear relative areas were determined from inspection of satellite photographs.

The author believes that the use of the best possible radiational heating profiles is extremely important. Although convective heat release is at least an order of magnitude greater than radiational cooling in strongly convective tropical weather systems, the cloud mass and energy fluxes which occur are extremely sensitive to Q_R. Yanai, et al. (1976) have shown strong variations in derived cloud populations with different Q_R profiles for disturbed tropical conditions. Gray (1976) has shown that radiation may be one of the fundamental driving forces for tropical cloud clusters, and the effect of radiation on tropical cyclones should be substantial. The climatological radiational heating values of Dopplick (1970) used by many researchers are not typical of cirrus-covered regimes and may give unrealistic results.

Each region is assumed to be in mass balance from the surface to 100 mb. No fluxes of h across 100 mb are allowed at radii greater than 2^{o}. Inside 2^{o} there are downward eddy fluxes of h at 100 mb due to cumulus overshooting of the tropopause. It is necessary to assume these fluxes to achieve realistic solutions to the spectral cloud analyses described below. The sea surface flux of h for each region is determined as a residual required to balance the large scale export of h from the region and the radiational cooling.

6.3 Spectral Cloud Analysis Method

To determine the nature of the vertical eddy fluxes of h, a spectral cloud model is employed. All upward vertical motion is assumed to occur in clouds with cloud base at 950 mb. Subsidence occurs between the updrafts. The mean mass flux ($\bar{\omega}$) at any level is:

$$\bar{\omega} = M_c + \tilde{\omega} \tag{6.8}$$

where M_c is the total mass flux in all clouds at that level and $\tilde{\omega}$ is the subsidence mass flux. The total vertical flux of h at any level is:

$$\overline{\omega h} = M_c \bar{h}_c + \tilde{\omega}\tilde{h} \tag{6.9}$$

where $\bar{h}_c$ and $\tilde{h}$ are the mean cloud and subsidence h values respectively. The eddy flux of h is the difference between the total flux and the mean flux:

$$\overline{\omega' h'} = \overline{\omega h} - \bar{\omega}\bar{h} = M_c \bar{h}_c + \tilde{\omega}\tilde{h} - \bar{\omega}\bar{h} \tag{6.10}$$

It is necessary to assume that the upward motion occurs in only a small fraction of the total area so that $\bar{h}$ is representative of the air outside active convective clouds. This approximation is valid at outer radii ($r \geq 2^o$). Inside about 2^o the approximation is less valid since about 5% of the area is covered by Cb convection and up to 25% of the lower troposphere may be covered by some form of convection (Malkus et al., 1961; Gentry, 1964). However, since most of this 25% total cloud cover is composed of very shallow clouds, the approximation should prove acceptable for convective fluxes above 700 mb.

Previous researchers have assumed that all $\tilde{\omega}$ occurs as gentle broad-scale subsidence at the environmental values of h ($\tilde{h} = \bar{h}$). This is not likely. Subsidence associated with deep convection occurs in a

variety of ways. In addition to the dry subsidence between cloud areas, there is a dynamic return flow around upward moving convective elements. Other strong downdrafts occur in or around clouds driven by evaporating rain and the drag of falling precipitation. These latter three types of downward flow are likely to occur at values of h substantially higher than the mean environmental values due to the high humidities in and adjacent to the clouds. Hence, the observed $\bar{h}$ is probably not typical of the effective mean downdraft $\tilde{h}$ at any level. The h values of these downdrafts and their mass flux magnitudes relative to the dry subsidence are difficult to estimate. Observations in and around cumulus convective elements are not adequate to resolve these problems. It seems very probable that the mass weighted mean value of $\tilde{h}$ is greater than $\bar{h}$ but less than $\bar{h}^*$ ($\bar{h}^*$ = h saturated). If $\tilde{h} > \bar{h}^*$, air would have to be forced downward despite upward buoyancy even if it were saturated. While this may occur in small regions where the frictional drag of heavy rain is important, it does not seem feasible that very much of the subsidence occurs in this manner.

It is convenient to express the value of $\tilde{h}$ in terms of a parameter α which varies from $\alpha = 0$ for $\tilde{h} = \bar{h}$ to $\alpha = 1$ for $\tilde{h} = \bar{h}^*$.

$$\tilde{h} = \bar{h} + \alpha (\bar{h}^* - \bar{h}) \tag{6.11}$$

There is no requirement for α to be a constant for all types of convection or at all levels within a given convective regime. Some effects of varying α upon the derived cloud mass fluxes are shown in the energy budget analysis of the 2-4° region.

With the introduction of the α parameter, it is necessary to alter the definition of Q_1-Q_2 in Eq. 6.7. Combining Eqs. 6.8 and 6.10:

$$\overline{\omega' h'} = M_c \bar{h}_c + (\bar{\omega} - M_c)\,\tilde{h} - \bar{\omega}\,\bar{h}$$

$$= M_c\,(\bar{h}_c - \tilde{h}) + \bar{\omega}\,\tilde{h} - \bar{\omega}\,\bar{h} \qquad (6.12)$$

Equation 6.7 becomes:

$$Q_1 - Q_2 - Q_R = \frac{\partial \bar{h}}{\partial t} + \overline{\nabla \cdot Vh} + \frac{\partial\, \bar{\tilde{\omega}}\, \bar{h}}{\partial\, p} = \frac{-\partial}{\partial p}\left[M_c\,(\bar{h}_c - \tilde{h}) + \bar{\omega}\,\tilde{h} - \bar{\omega}\,\bar{h}\right] \qquad (6.13)$$

By rearrangement one can introduce $(Q_1-Q_2)'$ such that:

$$(Q_1-Q_2)' - Q_R = \frac{\partial \bar{h}}{\partial t} + \overline{\nabla \cdot Vh} + \frac{\partial}{\partial p}\,(\bar{\omega}\tilde{h}) = \frac{-\partial}{\partial p}\, M_c\,(\bar{h}_c - \tilde{h}) \qquad (6.14)$$

$(Q_1-Q_2)' - Q_R$ is observable from large scale data with the stipulation that $\tilde{h}$ must be specified. In this study $\tilde{h}$ is a function of the observed $\bar{h}$ with specified values of α. Equation 6.14 is used to obtain the cloud mass fluxes in the energy budget analyses. Values of $(Q_1-Q_2)' - Q_R$ are determined for layers above cloud base (950 mb).

Cloud Spectrum. A spectrum of 11 types of cloud is assumed such that each cloud type tops out and detrains at the center of a different vertical level between 100-950 mb. Each cloud type is assigned a subscript i according to its detrainment level ranging from i=1 for the 100-150 mb layer to i=11 for the 900-950 mb interval. Clouds are assumed to be saturated at 950 mb at the mean large scale temperature and to have constant entrainment rates λ_i. Entrainment is the rate of mass flux of environmental air into the cloud and is a function of the form:

$$\lambda = \frac{1}{M}\,\frac{\partial M}{\partial z} \qquad (6.15)$$

where M is the mass of the cloud parcel.

Each cloud type is also assumed to have a constant detrainment rate μ_i for levels below the top total detrainment level to account partially for the dying phase of the cloud's life cycle when substantial detrainment occurs at all levels. Detrainment is the rate of mass flux of cloud air out of the cloud. In the uppermost layer of each cloud, all remaining cloud mass detrains. The detrainment rates are formulated as a percentage of the entrainment rates and decrease with cloud top height to simulate the relatively shorter lifetimes of shallow clouds. It is assumed that clouds which penetrate 400 mb have detrainment rates of $\mu = 0.25\ \lambda$. Middle-level clouds (tops from 400-700 mb) detrain at $\mu = 0.50\ \lambda$, and $\mu = \lambda$ for small clouds (tops between 700-950) mb). These values are obviously somewhat arbitrary, but the effects of detrainment upon the derived cloud mass flux profiles and cloud populations are not large. The cloud mass flux of any cloud type i at a level z will be:

$$\omega_{c_i}(z) = \omega_{cb_i}\ \eta_i(z) \tag{6.16}$$

where ω_{cb_i} is the mass flux at cloud base (z_o) and $\eta_i(z)$ is the normalized mass flux after Yanai (1976).

$$\eta_i(z) = e^{(\lambda_i - \mu_i)(z - z_o)} \tag{6.17}$$

The mass flux by all n cloud groups existing at a given level is:

$$M_c = \sum_{i=1}^{n} \omega_{c_i} = \sum_{i=1}^{n} \eta_i\ \omega_{cb_i} \tag{6.18}$$

The value of h_{c_i} of a cloud at a level P is:

$$h_{c_i}(P) = \frac{h_{c_i}(P-1)\ \eta_i(P-1) + \overline{(Ent)}\ \tilde{(h)} - \overline{(Det)\ (h_{c_i})}}{\eta_i(P-1) + (Ent) - (Det)} \tag{6.19}$$

where (Ent) and (Det) are the mass entrainment and detrainment respectively in the P-1 to P layer. The bars denote averages over the layer. Equation 6.19 may be expressed:

$$h_{c_i}(P) = \frac{\eta_i(P-1)\ h_{c_i}(P-1) + \eta_i\ \Delta z \left[\lambda\tilde{h} - \mu_i h_{c_i}\dfrac{(P-1)}{2}\right]}{\eta_i(P-1) + \eta_i\ \Delta z\ (\lambda - \frac{\mu}{2})_i} \tag{6.20}$$

where η_i is the mean value of η_i for the P-1 to P layer. Equation 6.20 is used to determine h_{c_i} for all cloud types, but above 400 mb freezing processes increase h_{c_i} as outlined below. It should be noted that the detrainment rate (μ_i) does not affect h_{c_i}.

The entrainment rate (λ) for each cloud type is computed so that the cloud will top out ($\omega = 0$) at the appropriate level. For clouds with tops below 400 mb, each cloud is assumed to detrain at its level of zero buoyancy. This is approximately the level where $h_c = \bar{h}^*$ ($\bar{h}^*$ = $\bar{h}$ saturated). Clouds with tops above 400 mb are assumed to overshoot their zero buoyancy levels by various amounts. The overshoot is estimated by applying Cotton's (1972) cloud model to the appropriate soundings. This one-dimensional model, which includes freezing processes, is discussed later.

Cb Overshooting. Overshooting by Cb clouds is an important feature of this analysis. Overshooting clouds produce downward fluxes of h at their upper levels. The required eddy fluxes of h from Eq. 6.14 are typically downward at

150 mb and 200 mb for most regions of the tropical storm circulation as is shown later. Therefore, without using an overshooting Cb cloud model, no solution can be obtained for the spectral cloud analysis. The overshooting used in this study is realistic in terms of current cloud theory.

The overshooting behavior of Cb clouds and the cloud population itself may vary according to the vertical profile of $\bar{h}$ and the type of organization associated with the deep convection. The entrainment rates of environmental air into Cb clouds should be lower for Cb's embedded in well organized squall lines than for relatively isolated clouds. The level of zero buoyancy and the amount of overshooting of a cloud depend on its entrainment of environmental air and the buoyancy experienced during ascent. This may have important ramifications for the use of spectral cloud models in parameterization schemes for numerical prediction models. If the overshooting behavior of the deep convective clouds changes significantly as the environment changes, then some sort of feedback may have to be used to relate Cb behavior to lapse rates of $\bar{h}$ and $\bar{h}_s$, convective organization and large scale convergence profiles. At the present time these important feedbacks are not well understood.

6.4 Ice Phase Processes

Ice phase transitions are usually neglected in the simple cloud models employed in spectral cloud analyses. In regions of intense deep convection, however, the effects of freezing water in the updrafts and melting ice at the lower levels may not be negligible. In tropical maritime Cb clouds the great majority of the freezing occurs from 400-250 mb while the melting occurs below the freezing level ($\sim$ 600 mb). Since ice is never observed falling at the surface in tropical storms, the only net effect of freezing upon the vertically integrated energy

budget is the small amount of ice advected outward in the outflow layer. This is neglected.

To investigate the effects of ice phase transitions upon the derived spectral cloud population, a simplified version of Cotton's (1972) cloud model is used. The model is run for constant entrainment rates, steady state and tropical maritime conditions using the mean soundings for the various tropical storm regions. The cloud is assumed saturated at the environmental temperature at 950 mb (cloud base) with no updraft velocity at that level. No supersaturation with respect to water is allowed. Freezing occurs by heterogeneous freezing due to containment of active freezing nuclei and by collection of ice crystals nucleated at the expense of liquid cloud water. Water droplets are assumed to fall out when their terminal velocities exceed the cloud updraft velocity.

The cloud model is run for various entrainment rates low enough to allow the cloud to penetrate 400 mb and hence for freezing to occur. Vertical profiles of h_{c_i} are obtained and compared to h_{c_i} values obtained for the simple constant entrainment/detrainment rate clouds discussed previously. An example of the h_{c_i} profiles of a freezing cloud and a simple nonfreezing cloud is seen in Fig. 6.4 for clouds in the 2-4^{o} region. From profiles such as these and estimates of Cb cloud mass fluxes based on conditions above 250 mb, the amounts of freezing from 400-250 mb are estimated. In the actual spectral cloud analyses, the h_{c_i} profiles of simple non-freezing clouds are used from the surface to 400 mb, and appropriate amounts of freezing are added above this level. This is done to simplify the computations. The cloud entrainment rates are adjusted iteratively to achieve clouds which reach zero buoyancy

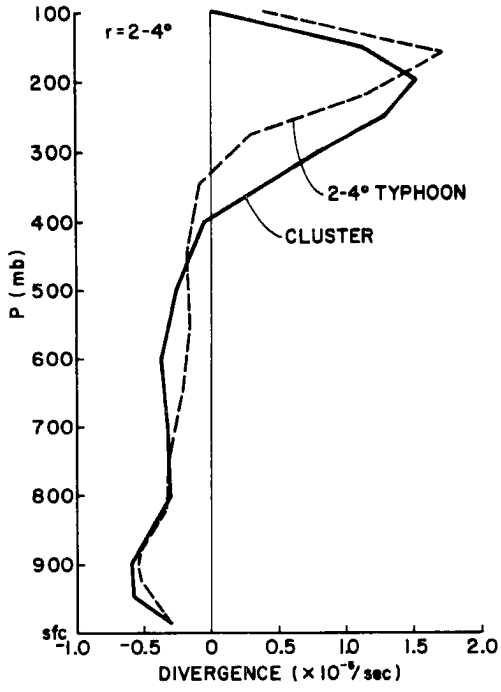

Fig. 6.5. Divergence, 2-4° region of typhoon and 0-2° area of a cloud cluster (Ruprecht & Gray, 1974).

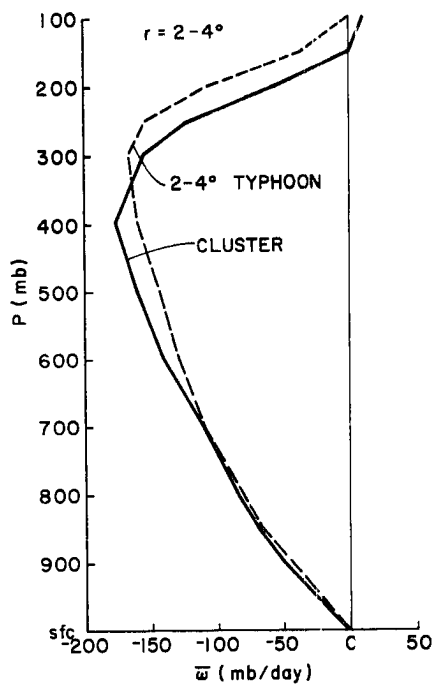

Fig. 6.6. Vertical motion for 2-4° region of typhoon and 0-2° area of cloud cluster.

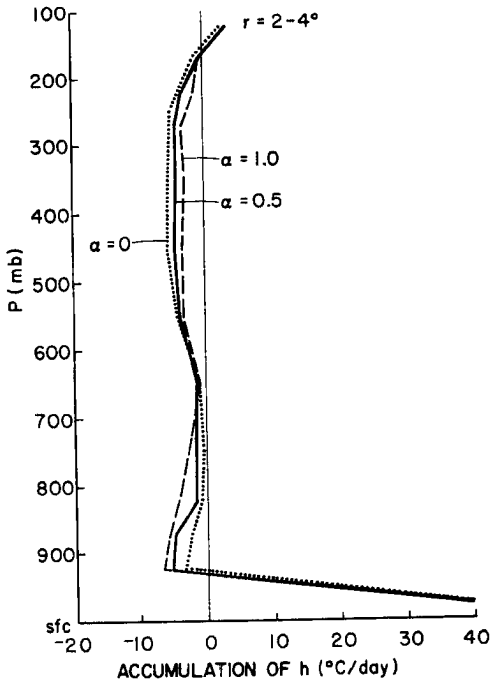

Fig. 6.7. Apparent accumulation of h, equal to $-[(Q_1-Q_2)'-Q_R]$ except in boundary layer where sea surface fluxes of h are included.

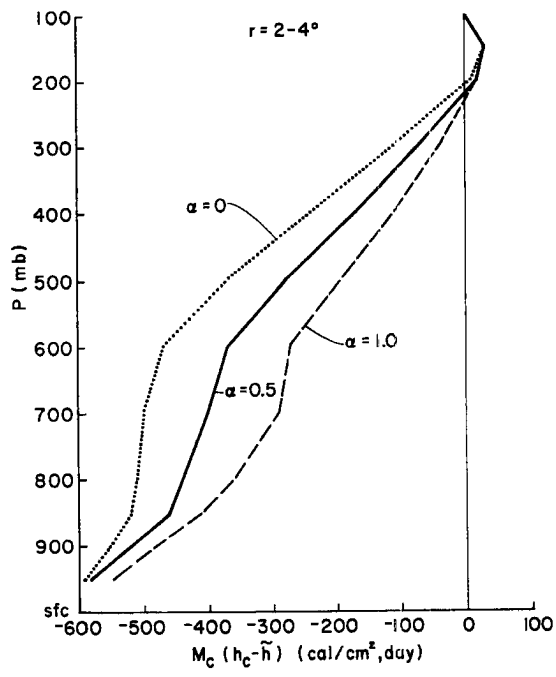

Fig. 6.8. Vertical eddy fluxes of moist static energy $M_c(h_c-\tilde{h})$. Negative numbers denote upward fluxes.

yield a solution at all. The cloud population used is shown in Table 6.1.

The vertical profiles of the total cloud mass fluxes (M_c) for the various α values are shown in Fig. 6.9. An M_c curve is included for an α which varies with height. Above 500 mb there are few differences between the curves. The $\alpha = 1$ curve blows up below 600 mb and is clearly unrealistic. The other curves show increasing amounts of vertical mass recycling in the lower troposphere with increasing α. Based on estimates of cloud momentum fluxes in the angular momentum budget analysis, it appears that $\alpha = 0.5$ gives more reasonable cloud momentum values than does $\alpha = 0$ or the shown variable α. This is by no means the last word on this subject. However, $\alpha = 0.5$ seems to be a reasonable first approximation. Certainly $0<\alpha<1$, and the importance of relatively high $\tilde{h}$ moist downdrafts is likely to be significant in organized deep convective areas such as tropical storm rainbands. The moist static energy analyses of all of the regions are performed assuming that $\alpha = 0.5$.

Figure 6.10 shows the cloud mass flux profiles for $\alpha = 0.5$ with and without ice processes. Also shown is the mean vertical motion ($\bar{\omega}$). The effect of the freezing/melting on M_c is very small. The primary effect of including the ice processes is to slightly increase the cloud mass fluxes of clouds which detrain near 400 mb and 650 mb and to decrease the cloud mass fluxes of clouds detraining from 250-400 mb. This is shown in Fig. 6.11 which shows the cloud base fluxes of the cloud populations in both cases. The ice process effects are not large, but they become increasingly more important for the regions inside 2^o radius where deep convection is significantly stronger. The ice phase parameterization discussed above is employed in the energy budget

TABLE 6.1
Cloud Spectrum (2-4°)

Detrainment Layer	Approximate Level Of Zero Buoyancy	Entrainment Rate (λ) (km^{-1})	Detrainment Rate (μ)
100-150 mb*	225 mb	.0796	.25λ
150-200 mb*	250 mb	.0930	.25λ
200-300 mb*	350 mb	.1127	.25λ
300-400 mb	400 mb	.1375	.25λ
400-500 mb	450 mb	.1679	.50λ
500-600 mb	550 mb	.2481	.50λ
600-700 mb	650 mb	.3230	.50λ
700-800 mb	750 mb	.4192	1.00λ
800-850 mb	825 mb	.6580	1.00λ
850-900 mb	875 mb	.9963	1.00λ
900-950 mb	925 mb	1.2831	1.00λ

*Includes Ice Processes

analyses of all of the regions. The $\alpha = 0.5$ with ice case appears to yield the best solution. The cloud mass flux profile for this case (Fig. 6.10) shows that this flux is about 15% greater than the mean circulation above 400 mb. Below that level the amount of vertical recycling increases dramatically.

The cloud base mass flux profiles of Fig. 6.11 show a bimodel distribution with few clouds topping out in the middle levels (300-700 mb). This is in agreement with the findings of Yanai et al., (1976), Cho & Ogura (1973), and Ogura & Cho (1974) for tropical weather systems containing deep convection. The cloud base mass fluxes of clouds detraining below 700 mb are much higher than reported by these authors primarily due to the assumption that $\alpha > 0$.

It is somewhat surprising that so little vertical mass recycling is indicated in the middle troposphere (300-600 mb). There are numerous reports of strong downdrafts in tropical cyclones and near thunderstorms at these elevations, probably driven by the drag of falling precipitation.

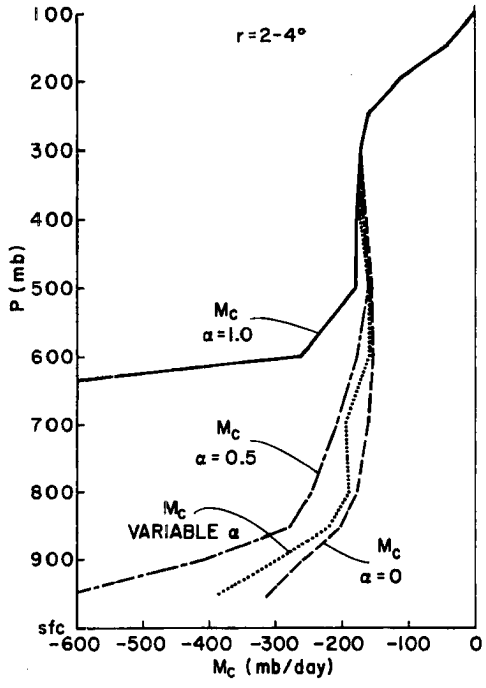

Fig. 6.9. Total cloud mass flux profiles (M_c) for various α values and for a variable α where α=0.6 above 400 mb, α=0.4 from 400-700mb, and α=0.2 below 700mb. Negative values denote upward motion.

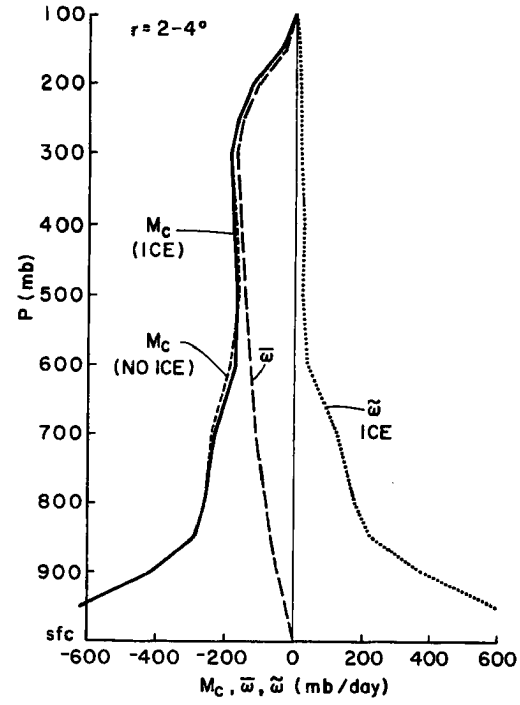

Fig. 6.10. Cloud mass flux profiles (2-4°) for α=0.5, mean vertical motion ($\bar{\omega}$) and extra-cloud subsidence ($\tilde{\omega}$).

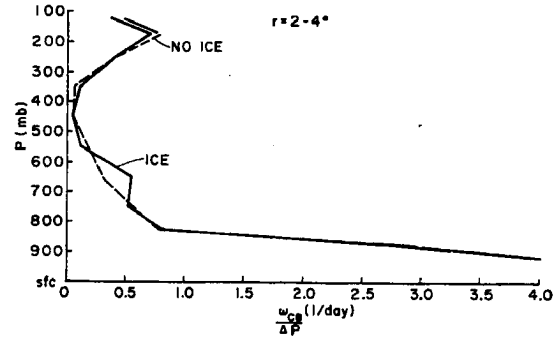

Fig. 6.11. Cloud base mass flux divided by pressure depth of detrainment level for clouds detraining at various heights.

Such downdrafts may come down saturated with neutral or negative buoyancy ($\alpha \geq 1$) and therefore may not be fully detected in an energy budget analysis of vertical mass fluxes. It seems probable that the vertical mass recycling of Fig. 6.10 is somewhat underestimated in the middle troposphere and that there should be more clouds detraining there than are indicated in Fig. 6.11. These observations should be applicable to all regions containing significant deep convection.

Vertical profiles of cloud mass detrainment (constant μ detrainment plus cloud top detrainment) and entrainment (constant λ entrainment) are shown in Fig. 6.12. Detrainment has maxima above 300 mb and just above cloud base while entrainment has a smaller peak above cloud base and is more or less constant up to 400 mb. Figure 6.13 compares the

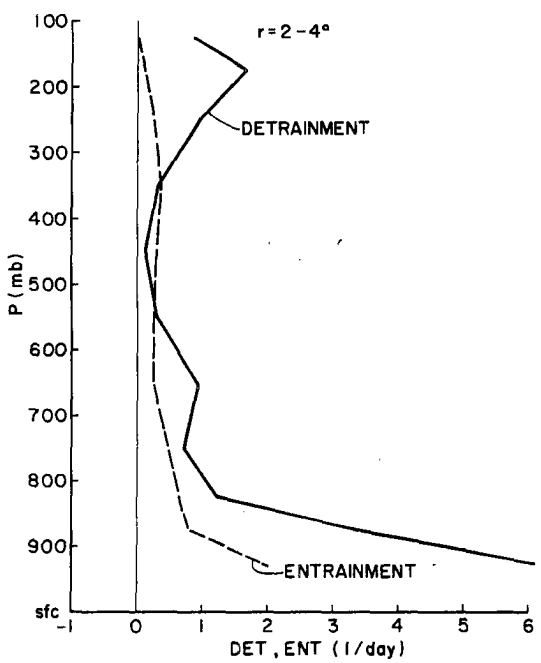

Fig. 6.12. Total cloud detrainment and entrainment per unit pressure depth.

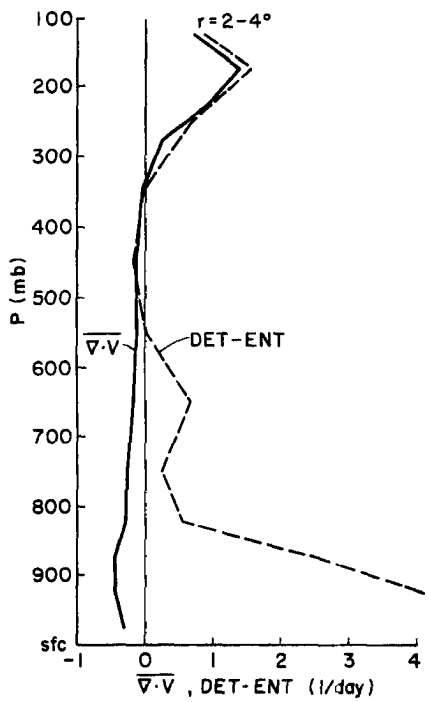

Fig. 6.13. Large scale 2-4° divergence profile and net cloud mass detrainment (detrainment minus entrainment) per unit pressure depth.

net cloud detrainment (detrainment-entrainment) with the large scale mean divergence profile. The two profiles agree very well above 600 mb. Recycling is small at these levels, and the large scale divergence pattern reflects the predominantly upward and outward mass flux of the Cb clouds.

Below 600 mb there is a large amount of net cloud detrainment in addition to large scale mass convergence. Both processes supply mass to the area outside the clouds. This results in strong environmental sinking across cloud base (950 mb). The mean vertical motion at 950 mb is only about 3% of the total cloud base mass flux. Most of the large scale convergence from 950 mb to 600 mb appears to subside into the boundary layer rather than being entrained into clouds or lifted outside of them. This implies that environmental subsidence at cloud base due to large convergence is about 100 mb/day or nearly 5 times the mean upward motion resulting from large scale sub-cloud layer convergence.

0.7-2° Radius (Inner Convective Rainbands). Analysis of the regions inside 2° radius is complicated by the lack of an accurate radial wind profile at r = 0.7° and by the increasingly large percentage of the total area covered by active convection. The latter condition violates the parameterization theory of the spectral cloud model. However, it is felt that the average area of convective cloud cover in the upper and middle troposphere is sufficiently small to permit at least a first approximation of the cloud populations above 700 mb or so in the .7°-2° region. Cloud mass fluxes below 700 mb and inside of 0.7° radius at all levels are highly speculative, but certain conclusions may be reached based on observations from various sources.

An approximate radial wind profile is constructed for r = 0.7° based on flight data (Shea & Gray, 1973) and the limited number of

soundings available near this radius. This profile is shown in Fig. 6.14 and results in a divergence profile with large amounts of low level (surface - 800 mb) convergence and upper tropospheric (100-300 mb) divergence (Fig. 6.15). Little divergence is observed in the middle levels. Horizontal fluxes of h at 0.7^{o} radius are assumed to be those resulting from the mean circulation alone. The large scale accumulation of h is shown in Fig. 6.16, and the required vertical eddy fluxes of h are shown in Fig. 6.17. Note the downward fluxes of h at 100 mb and 150 mb. It is necessary to assume a downward flux of h at the upper boundary to balance the h deficit observed in the 100-150 mb layer with the assumed cloud spectrum. Without this overshoot cooling at the upper boundary, cloud mass fluxes would be significantly less than the mass fluxes by the mean upward vertical motion in the upper troposphere. Due to the large vertical gradients of h at these levels, the amount of Cb mass overshooting required to produce such a 100 mb eddy flux is not large, as is shown later. Satellite photographs and high altitude aircraft observations confirm the frequent penetration of the tropopause by Cb clouds in tropical cyclones. This downward eddy flux of h at 100 mb implies cooling of the lower stratosphere. This cooling is probably balanced by a large scale lower stratospheric divergence accompanied by weak subsidence above the hurricane core and convergence at higher levels. This circulation may be driven mechanically by the net import of angular momentum into the region by the overshooting Cb's. Since pressure gradients in the stratosphere are extremely weak, eddy momentum flux spinning up the air would cause divergence.

The cloud spectrum for $0.7\text{-}2^{o}$ is shown in Table 6.2. It is similar to the cloud population of $2\text{-}4^{o}$. A few clouds of the tallest cloud group are assumed to penetrate 100 mb. The deep convection in

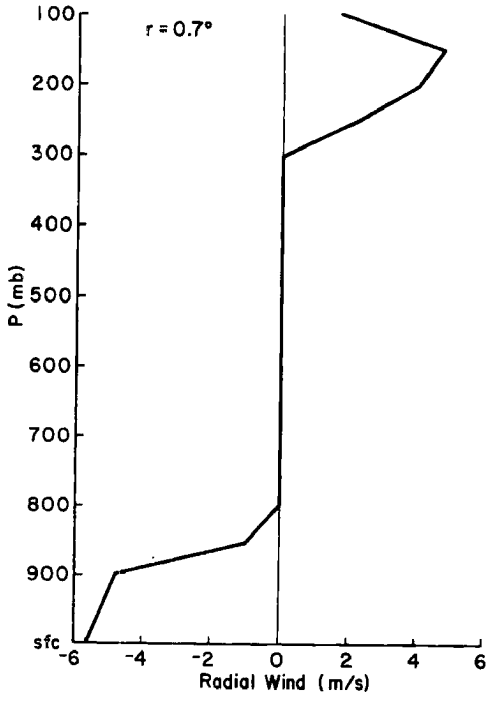

Fig. 6.14. Assumed radial wind profile at r=0.7°.

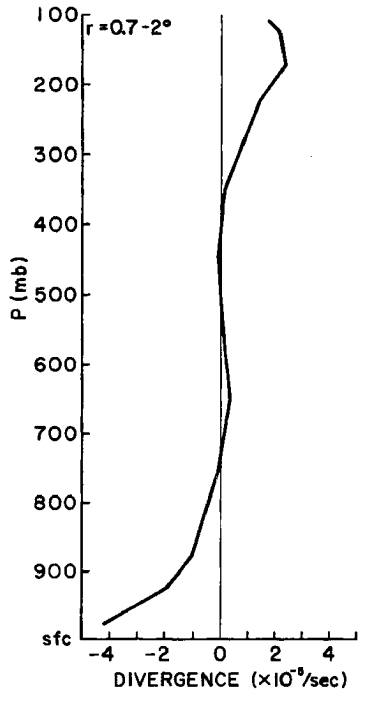

Fig. 6.15. Divergence profile (0.7-2°) based on assumed V_r profile at 0.7° and observed flow at 2°.

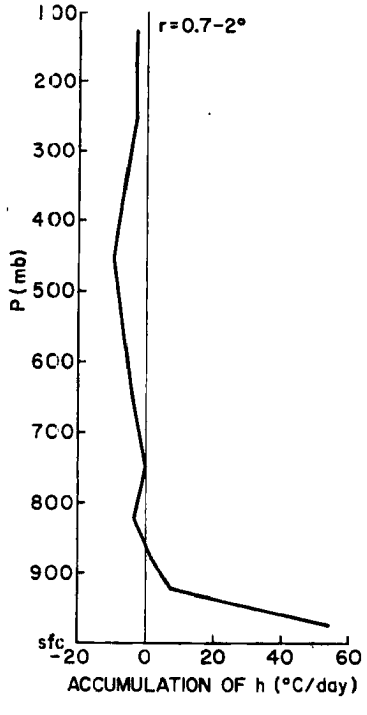

Fig. 6.16. Apparent accumulation of h (0.7-2°) equal to $-[(Q_1-Q_2)'-Q_R]$ except in the boundary layer where sea surface fluxes of h are included.

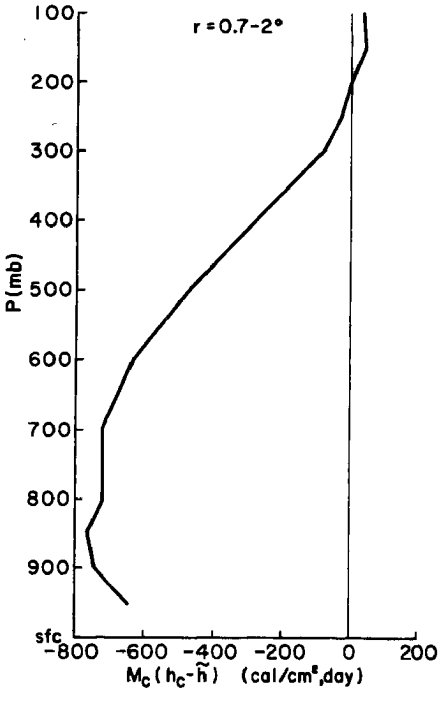

Fig. 6.17. Vertical eddy fluxes of moist static energy (0.7-2°). Negative numbers denote upward fluxes.

TABLE 6.2

Cloud Spectrum ($0.7-2^{o}$)

Detrainment Layer	Level of Zero Buoyancy	Entrainment Rate(λ)(km^{-1})	Detrainment Rate (μ)
100-150 mb	225 mb	.0750	.25λ
150-200 mb	250 mb	.0898	.25λ
200-300 mb	300 mb	.1166	.25λ
300-400 mb	400 mb	.1517	.25λ
400-500 mb	450 mb	.2007	.50λ
500-600 mb	550 mb	.3383	.50λ
600-700 mb	650 mb	.4866	.50λ
700-800 mb	750 mb	.6615	1.00λ
800-850 mb	825 mb	1.0575	1.00λ
850-900 mb	875 mb	1.9353	1.00λ
900-950 mb	925 mb	3.9702	1.00λ

this region occurs predominantly in organized squall lines, and middle level humidities are relatively high. Therefore, the clouds probably undergo less entrainment drying than clouds in the outer storm regions and reach higher levels. However, the temperature lapse rates in this region allow less buoyancy for tall clouds than at greater radii which tends to inhibit overshooting.

The derived M_{c_i}, $\tilde{\omega}$ and $\bar{\omega}$ profiles are shown in Fig. 6.18. As in the previous region, there is considerable vertical recycling at low levels. Considerable environmental subsidence is observed up through 300 mb. Some of this is probably due to dynamic return flow around the cloud elements, and some results from downdrafts driven by evaporation and precipitation drag. The sharp increase in $\tilde{\omega}$ below 600 mb is primarily a result of melting ice. The cloud base mass fluxes of the various cloud groups are displayed in Fig. 6.19. A strong maximum is observed just above cloud base. There are secondary maxima at 175 mb and 650 mb, but the cloud population does not appear to be bimodal. The strong ice processes occurring in this intense convective region are

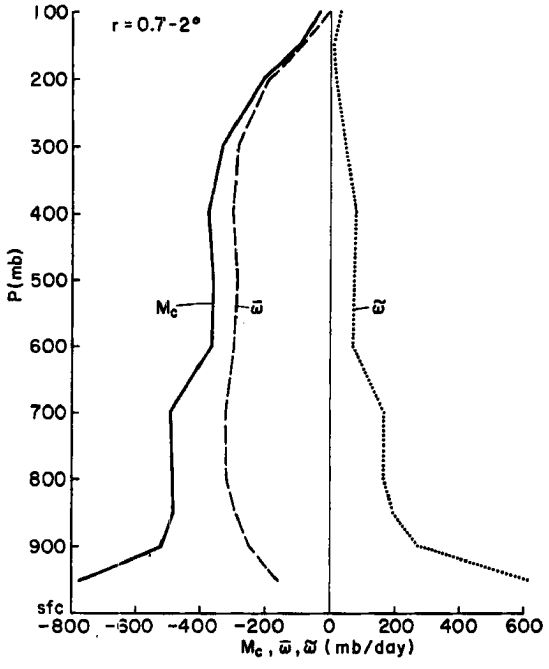

Fig. 6.18. Total cloud mass flux profile (M_c), mean vertical motion ($\bar{\omega}$) and extra-cloud subsidence ($\tilde{\omega}$)(0.7-2°).

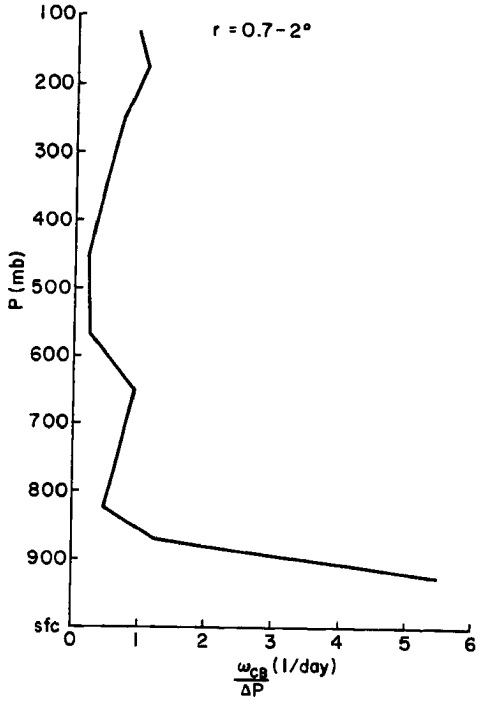

Fig. 6.19. Cloud base mass flux per unit pressure depth of cloud detrainment layer for clouds detraining at different levels.

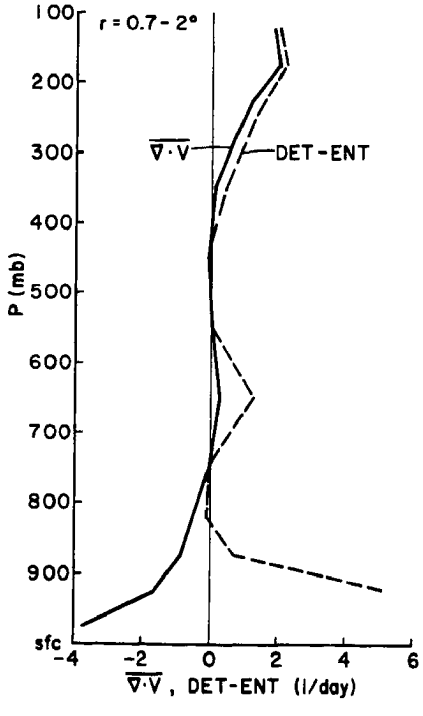

Fig. 6.20. Large scale divergence and net cloud detrainment (detrainment minus entrainment) per unit pressure depth.

most responsible for the lack of the bimodal cloud distribution characteristic of warm cloud model analyses. The net detrainment-entrainment mass flux from the clouds and the large scale convergence profile are compared in Fig. 6.20. As in the 2-4° region, the two curves agree well in the middle and upper troposphere implying that the large scale mass flux above about 700 mb is directly related to the deep convection. Below 800 mb there is evidence of strong frictional convergence as well as net cloud detrainment.

In this region the mean vertical motion at cloud base accounts for about 25% of the total cloud mass flux. The cloud base mass flux of all clouds detraining above 400 mb is about 27% of the total cloud mass flux at cloud base.

0-0.7° Radius (Eyewall Region). As mentioned previously an energy budget for this region must be rather speculative. The spectral cloud parameterization scheme is not reliable because of the large percentage of the area covered by active updrafts and the lack of quantitative data at many levels.

The mean vertical motion based on the assumed radial wind profile of Fig. 6.14 is shown in Fig. 6.21. Surface friction probably accounts for the low-level convergence. Figure 6.22 shows the large scale accumulation of h while Fig. 6.23 shows the required eddy fluxes for α = 0.5 but without ice processes. Estimates of freezing and melting are omitted since they require computation of cloud mass fluxes in Cb clouds. The downward flux of h shown at 100 mb is the minimum required to achieve approximate upper level energy balance assuming no flux at 150 mb (based upon estimates of h_c at cloud base and $\bar{h}$ at 150 mb). The composite data indicates that saturated cloud base air has an h of about 84.64 cal/g. Air of this energy content cannot transport significant amounts of

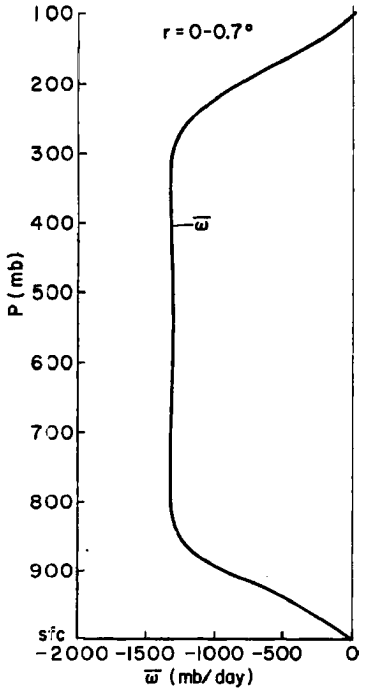

Fig. 6.21. Mean vertical motion (0-0.7°) based on assumed radial wind profile at 0.7° radius.

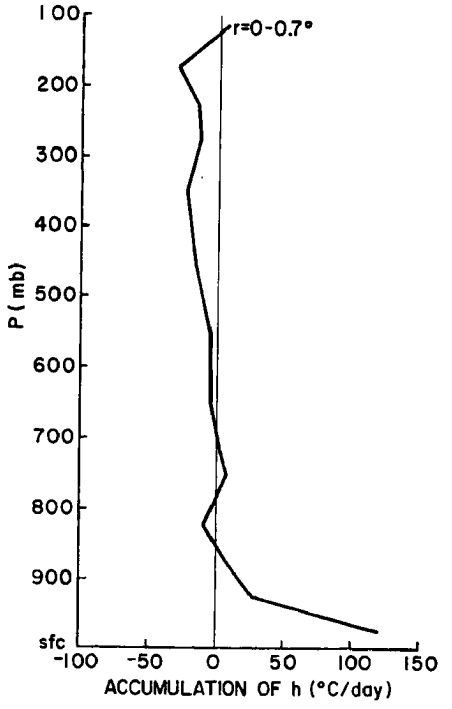

Fig. 6.22. Apparent accumulation of h (0-0.7°) equal to $-[(Q_1-Q_2)'-Q_R]$ except in the boundary layer where sea surface to air fluxes of h are included.

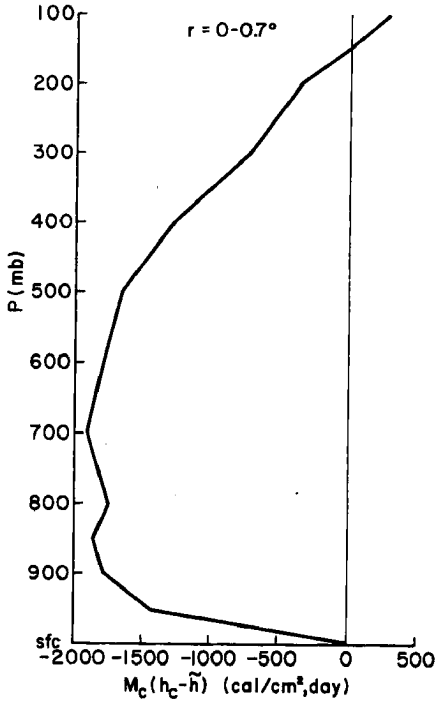

Fig. 6.23. Vertical eddy fluxes of moist static energy (0-0.7°). Negative numbers denote upward fluxes.

of this region contains some outer rainbands and convection typical of conditions beyond the "moat".

The mean 4-6° divergence profile is shown in Fig. 6.24. Weak low level divergence is evident. Weak mid-level convergence and upper level divergence are also observed. The mean vertical motion profile (Fig. 6.25) shows subsidence below 400 mb with mean ascent above that level.

Values of the accumulation of h are shown in Fig. 6.26. Figure 6.27 shows the vertical eddy fluxes of h required for energy balance including ice processes. These fluxes are downward at 150 and 200 mb. It is assumed that there is no significant eddy flux at 100 mb. Estimates of surface evaporation from the water budget analysis indicate that the divergence of q from 4-6° is too large, probably due to a small overestimate of the low level divergence. This does not show up as obviously in the h budget analysis since the low level divergence of q·L is partially balanced by middle level convergence of relatively high s air. The author does not feel that this possible inaccuracy has a substantial effect on the derived cloud fluxes for the 4-6° region.

The cloud spectrum used from 4-6° is essentially the same as the one used in the 2-4° analyses with the entrainment (λ) values adjusted to fit the sounding. Figure 6.28 shows the cloud mass flux and subsidence profiles. Significant subsidence is seen at all levels below 200 mb. Total subsidence greatly exceeds the mean subsidence indicating large amounts of recycling below 300 mb.

The cloud base mass flux distribution for 4-6° is shown in Fig. 6.29. There is evidence of some Cb activity (probably the result of the occasional outer rainbands intruding into the moat region), but the cloud population consists primarily of small clouds detraining

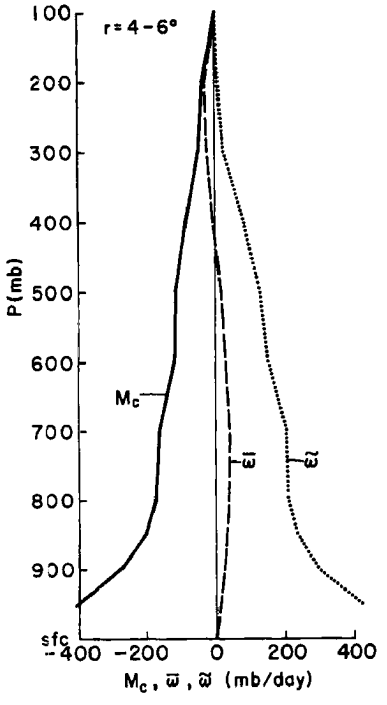

Fig. 6.28. Total cloud mass flux (M_c), mean vertical motion ($\bar{\omega}$) and extra-cloud subsidence ($\tilde{\omega}$).

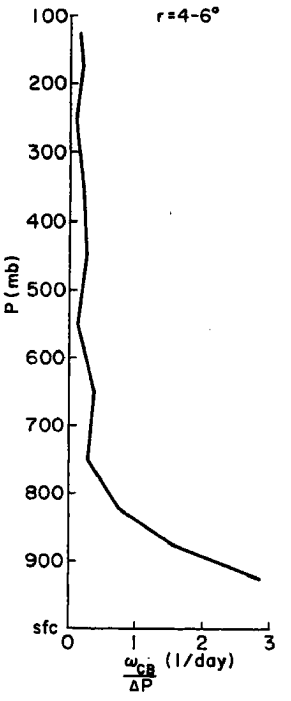

Fig. 6.29. Cloud base mass flux per unit pressure depth of cloud detrainment layer for clouds detraining at various levels.

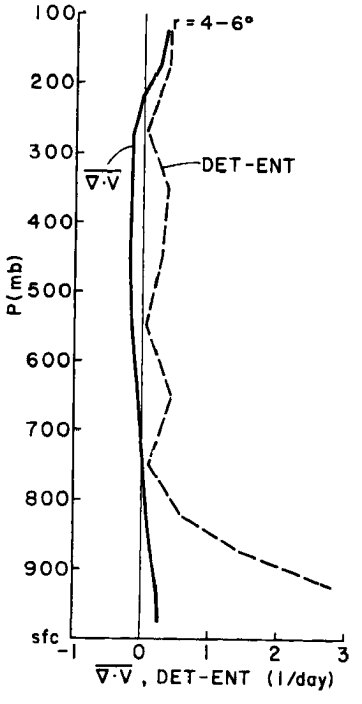

Fig. 6.30. Large scale divergence and net cloud detrainment (detrainment minus entrainment) per unit pressure depth.

below 700 mb. This agrees well with most qualitative descriptions of the moat area. Note that cloud base mass flux and low level cloudiness are significant even in this region of boundary layer divergence. This supports the findings of Ogura and Cho (1974) that small clouds are present in regions exhibiting little or no boundary layer convergence. Cb clouds, however, tend to be well correlated with boundary layer convergence. This is discussed in more detail later.

Total cloud detrainment minus entrainment is compared to the mean divergence profile in Fig. 6.30. The shapes of the two curves are quite similar, but the magnitudes are different reflecting the large amount of subsidence throughout the troposphere.

6-8° Radius (Typical Outer Circulation Region). Composites of the 6-8°, 8-10° and 10-12° regions show relatively similar divergence, radiational warming, and vertical h flux profiles. Therefore, the 6-8° region is presented as typical of the hurricane circulation beyond the moat area. It is uncommon to find typhoon convective rainbands this far from the circulation center. Satellite observations show few obvious differences in cloud populations between these outer radii around tropical cyclones and average tropical conditions despite the obvious influence of the storm circulation.

The divergence profile is shown in Fig. 6.31 and the mean vertical motion profile in Fig. 6.32. Figure 6.33 shows the profile of the accumulation of h while Fig. 6.34 shows the required eddy h fluxes. The flux is again downward, though weak, at 150 mb but is nearly zero at 200 mb.

Approximately the same cloud type spectrum used in the 2-4° and 4-6° analyses is employed here. The resulting profiles of M_c and $\tilde{\omega}$ are shown in Fig. 6.35. The subsidence profile is quite similar in shape to that of the 4-6° region. Strong recycling is again evident through most of the troposphere.

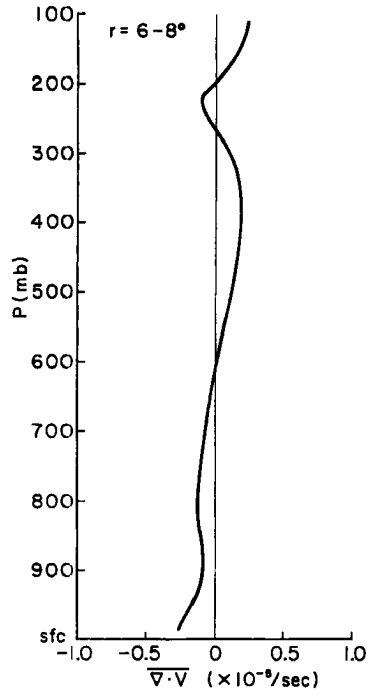

Fig. 6.31. Large scale divergence (6-8°).

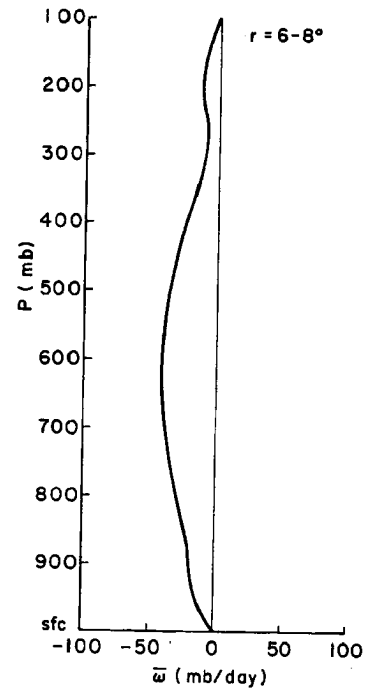

Fig. 6.32. Mean vertical motion (6-8°).

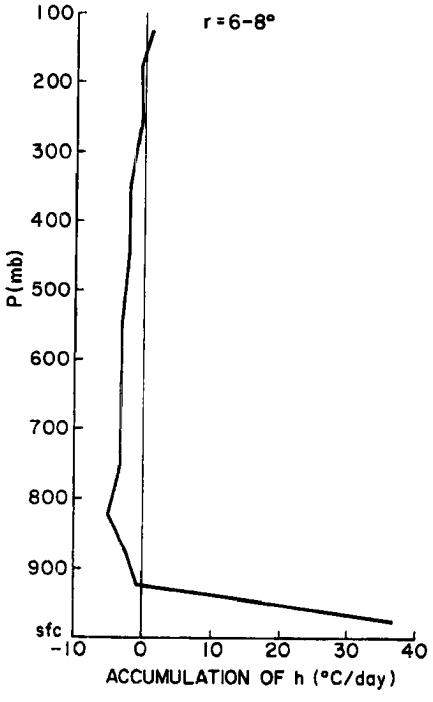

Fig. 6.33. Apparent accumulation of h (6-8°) equal to $-[(Q_1-Q_2)'-Q_R]$ except in the boundary layer where sea surface fluxes of h are included.

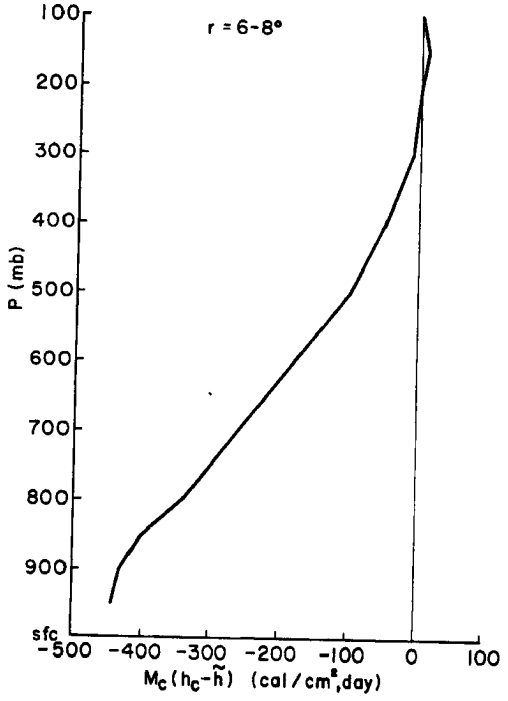

Fig. 6.34. Vertical eddy fluxes of moist static energy. Negative numbers denote upward fluxes.

The cloud base mass flux distribution is shown in Fig. 6.36. An abundance of low level cloudiness is observed, as usual, and smaller but significant amounts of upper and middle level cloudiness are found. The distribution is not bimodal.

Net cloud detrainment minus entrainment and the large scale divergence profiles are shown in Fig. 6.37. These two curves are in good agreement above 500 mb. The difference between the curves is indicative of the subsidence mentioned previously. Below 700 mb there is weak large scale convergence and considerable small-cloud recycling. The mean mass flux at cloud base is about 4% of the total cloud mass flux.

6.6 Discussion

Relationships of Cloud Population to Low Level Convergence. Cho and Ogura (1974) noticed that a spectral cloud analysis of the Reed and Recker (1971) tropical wave data showed abundant low cloudiness in all regions but significant deep convection (penetrating 500 mb) only where low level convergence was present. They found that the cloud base mass flux of deep clouds increased nearly linearly with low level convergence.

Table 6.3 shows the large scale convergence below 700 mb for the four typhoon radial bands from 0.7-8^{o} and the total cloud base mass flux of all convection penetrating the 300 mb level. The 300 mb level is chosen as representative of the lowest cloud top for Cb convection since that level is usually near the bottom of the typhoon outflow. Most of the cloud mass penetrating 300 mb is advected out of the storm above

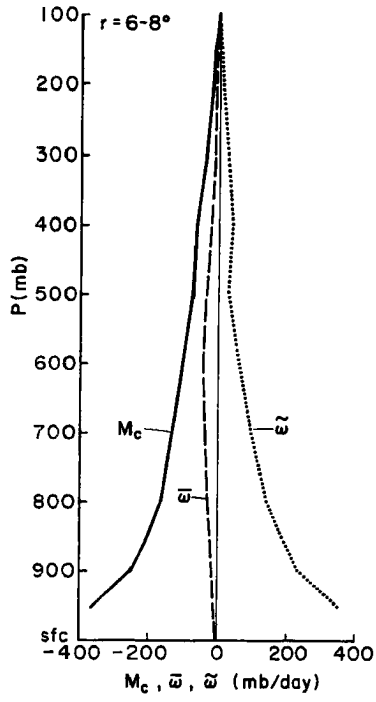

Fig. 6.35. Total cloud mass flux (M_c), mean vertical motion ($\bar{\omega}$), and extra-cloud subsidence ($\tilde{\omega}$).

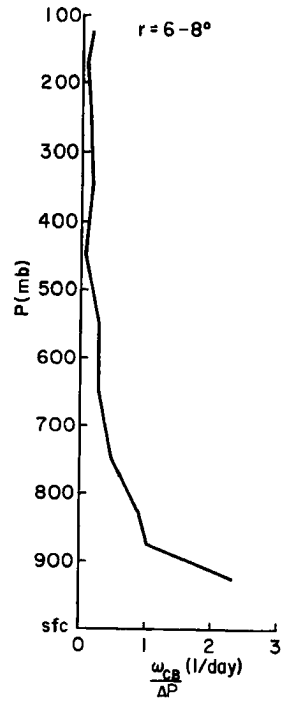

Fig. 6.36. Cloud base mass flux per unit pressure depth of cloud detrainment layer for clouds detraining at various levels.

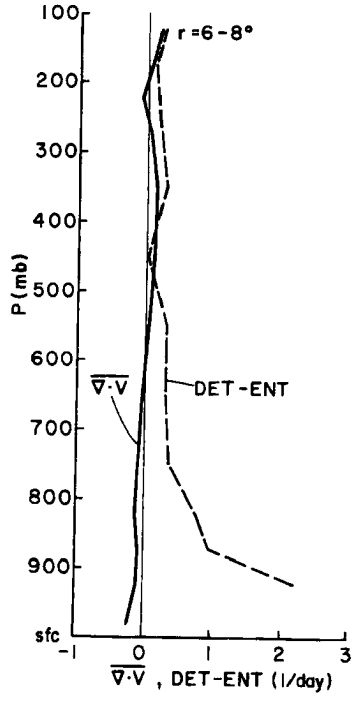

Fig. 6.37. Large scale divergence and net cloud detrainment (detrainment minus entrainment) per unit pressure depth.

that level. Also shown in Table 6.3 are the total cloud base mass fluxes for all cloud types and for shallow clouds.

TABLE 6.3

Cloud Base Mass Fluxes (ω_{cb}) of Cb Clouds, Shallower Clouds, and All Clouds (mb/day) Compared to Low Level Convergence (x $10^{-5}sec^{-1}$).

Radial Band	Mean Convergence Below 700 mb (x $10^{-5}sec^{-1}$)	ω_{cb} for all clouds penetrating 300 mb	ω_{cb} for clouds with tops below 300 mb	ω_{cb} all cloud types
0.7-2°	1.28	169	605	774
2-4°	.41	93	528	621
4-6°	-.15	26	386	412
6-8°	.14	20	344	364

The cloud base mass flux into Cb clouds varies in approximately direct proportion to the low level convergence as noted in the Cho & Ogura (1974) study. The 4-6° anomaly is probably due to the fact that most of that region exhibits low level subsidence while the deep convection is confined to smaller but significant regions which presumably have strong low level convergence. These convective regions are probably extreme outer rainbands drifting away from the storm center. The compositing shows the need for some deep convection to balance the energy budget but shows weak low level subsidence over the large time and space scale averaging.

Total cloud base mass flux for non-Cb clouds also tends to increase somewhat with low level convergence, but the relationship is less strong. Significant numbers of low and middle level convective

clouds occur in all typhoon regimes. An increase of low level convergence from 6-8^{o} to .7-2^{o} of over nine times barely doubles the cloud base mass flux of shallow clouds.

These findings suggest that Cb convection may be controlled by different processes than those controlling lower level clouds. The traditional explanation of the link between deep convection and low level convergence is that the convergence and resulting mean upward vertical motion destabilize the environment and increase middle level moisture enhancing the tendency for Cb development. It is hard to believe that this is the case. The above typhoon data shows generally increasing Cb convection and low level convergence with decreasing radius. However, the stability of the atmosphere also increases with decreasing radius (see section 2.4) due to the upper level warm core of the storm. Strong conditional instability of the atmosphere is often negatively correlated with Cb activity in the tropics. The high middle tropospheric humidities found in tropical convective systems result from cloud detrainment and are a result, not a cause, of deep convection. It is unclear how increased upper level temperature and moisture conditions could feed back to produce the large amounts of local sub-cloud base convergence required to produce a Cb cloud.

The weak relationship of low and middle level cloudiness to low level convergence also appears to cast doubt on the hypothesis that such convergence enhances Cb activity through destabilization. Destabilization would seem to imply increased amounts of cumulus clouds topping out at all levels. This is not observed. When low level convergence is present, it is primarily clouds with tops above 300 mb which respond.

Precipitation vs. Deep Convection. A significant correlation between deep convection and observed precipitation is to be expected. Table 6.4 shows estimated rainfall from Chapter 5 and the total cloud base mass flux of all Cb clouds (tops above 300 mb) for the 5 radial bands inside 8°. The distribution of $0\text{-}2^{\circ}$ precipitation between the $0\text{-}0.7^{\circ}$ and $0.7\text{-}2^{\circ}$ bands is estimated from Miller (1958a).

It is clear that observed rainfall is closely related to Cb cloud base mass flux beyond 2° radius. The ratio of the two varies from .025 - .035. In the inner regions the relationship is less clear, but the cloud mass fluxes and precipitation estimates are rough there. It would seem that a direct relationship between the Cb cloud base mass flux and rainfall may be assumed.

TABLE 6.4

Total Rainfall (cm/day) and Cloud Base Mass Flux (mb/day) of Cb Clouds Also Shown is the Ratio of the Two

Radial Band	Rainfall cm/day	ω_{cb} of Cb clouds mb/day	Rainfall/ω_{cb} (Cb's) cm/mb
$0\text{-}0.7^{\circ}$	14.0*	(1330)	(.010)*
$0.7\text{-}.2^{\circ}$	7.3*	(169)	(.043)*
$2\text{-}4^{\circ}$	2.3	93	.025
$4\text{-}6^{\circ}$	.7	26	.027
$6\text{-}8^{\circ}$	.7	20	.035

*Estimated distribution of $0\text{-}2^{\circ}$ rainfall.

( ) Based on estimated radial wind profile at 0.7°.

Sea Surface Energy Fluxes. Classical hurricane theory assumes a greatly increased flux of both sensible and latent heat from the sea to the air in the storms, primarily due to high wind speeds, (Riehl, 1954, 1963). This hypothesis has been challenged recently by Fendell (1974). Previous energy budget studies of individual storms (Riehl and Malkus, 1961; Hawkins and Rubsam, 1968; Hawkins and Imbembo, 1976) have lacked sufficient radial wind data to obtain good residual estimates of sea surface fluxes of h. Most modeling studies compute these surface fluxes by the bulk aerodynamic method using Eq. 5.12 to compute evaporation and Eq. 6.18 to estimate the sensible heat flux.

$$S = \rho\, C_s\, C_p\, (T_s - T)\, V \tag{6.18}$$

where
- S = Sensible heat flux at surface
- ρ = Density of surface air
- C_s = Coefficient of sensible heat transfer
- C_p = .24 cal/gm ^{o}C
- T_s = Sea surface temperature
- T = Surface air temperature
- V = Wind Speed

In the present study values of total sea surface to air fluxes of h are computed as residuals in the composited vertically integrated h budget computations of this chapter. These fluxes are shown in Table 6.5. Assuming a Bowen Ratio of 0.1 the sensible heat flux and evaporation are estimated. Evaporation values from the moisture budget analysis of Chapter 5 are also shown. The water vapor budget evaporations tend to be higher, especially from 4-6^{o} where the observed moisture divergence is probably too high as previously discussed, but the general agreement is good.

It is generally accepted that tropical cyclones require a warm sea surface layer of significant depth to maintain their intensity.

TABLE 6.5

Sea Surface to Air Fluxes of h, S, q

Sea Surface Fluxes (cal $cm^{-2} day^{-1}$)	0-.7°	.7-2°	2-4°	4-6°	6-8°
h - residual from h budget	1470	820	670	530	470
S	134	75	61	48	43
h-S (-L evaporation)	1336	745	609	482	427
Evaporation (cm/day)	2.2	1.2	1.0	.8	.7
Evaporation From Water Budget (cm/day)		2.3 (0-2° Ave.)	1.1	1.4	.6

Climatological studies by Gray (1975) and Palmén (1948, 1957) have shown that tropical cyclone genesis occurs only in regions where the sea surface temperature is above 26½°C and where the depth of the 26° isotherm is 60 m or more. Ooyama (1969) and Rosenthal (1971) have shown that surface fluxes of moisture and sensible heat are critical in achieving realistic storm intensifications in their models. Brand (1971) has demonstrated the weakening effects of cool surface waters upon typhoons.

Some previous researchers have estimated sea to air moist static energy fluxes of 3000-4000 cal/cm^2 day in the inner 100 km from empirical studies. Table 6.6 compares the sea surface to air fluxes of h inside 2° radius determined from the present h budget analysis to the fluxes determined by bulk aerodynamic computations for Hurricane Daisy by Riehl and Malkus (1961), for Hilda by Hawkins and Rubsam (1968), and for Inez by Hawkins and Imbembo (1976). Also shown are estimates for Hilda by Leipper (1967) and for moderate storms by Malkus and Riehl (1960).

TABLE 6.6

Sea Surface to Air h Fluxes (cal/cm^2 day)

Study	h Fluxes	Region
Present Study	1470	(0-80 km)
	820	(80-220 km)
Daisy (Riehl & Malkus)		
August 25	1019	(0-130 km)
August 27	1675	(0-130 km)
Hilda (Hawkins & Rubsam)	∿2560	(16-130 km)
Hilda (Leipper)	∿4150	(∿0-240 km)
Inez (Hawkins & Imbembo)	∿4018	(18-90 km)
(Malkus & Riehl)	3140	(30-90 km)

The agreement with the Daisy study is relatively good, but the fluxes from the other studies are much larger. Due to the great variability of tropical storms, it is difficult to establish case study results as being very accurate or representative.

According to classical theory, the values of θ_e of the low level inflowing air must increase enormously to allow buoyant convection in the strong warm core environment near the storm center and to explain observed hydrostatic pressure drops (Malkus & Riehl, op. cit.). In addition, surface temperatures are observed to drop only about 1-2^{o}C from the outer regions of strong tropical cyclones to the inner core areas despite pressure drops of 30-100 mb or so. Adiabatic expansion would predict surface temperature drops of 3-9^{o}C as was noticed by Byers (1944). This observation led Malkus & Riehl (1960) to estimate

sea to air sensible heat fluxes of 720 cal/cm^2 day inside 90 km for a fairly strong hurricane - an increase of about 20 times over mean tropical fluxes.

The results of the present study indicate a mean sea to air moist static energy flux of about 1470 cal/cm^2 day inside 80 km. Sensible heat flux is estimated at about 134 cal/cm^2 day (less than 1/5 of the Malkus and Riehl estimate), although this figure would double for a Bowen Ratio of 0.2. This increase is not unreasonable since inner core surface air temperatures are 1-2^o cooler than those at 2^o radius. Nevertheless, surface fluxes of sensible and latent heat would appear to be less than half of the fluxes reported by the above studies.

The 0-0.7^o surface latent heat flux of this study is about 3 times the flux during mean tropical conditions. This is in agreement with the results of tritium-tracing studies of Ostlund (1968, 1970). The author does not feel that case studies of individual storms using conventional data can provide sufficiently accurate measurements of radial winds, sea surface temperatures or eddy fluxes to construct accurate moist static energy budgets. Although the present budgets inside 2^o are somewhat speculative, mean sea surface fluxes of h of the sizes reported in the empirical studies of the above authors do not appear to be consistent with the observations of this study.

The sea surface to air fluxes in the numerical models of Ooyama (1969) and Rosenthal (1971) are computed using the bulk aerodynamic method. As mentioned previously, Ooyama achieved good results with a constant C_E of 1.5 x 10^{-3} applied to the gradient level winds. This agrees well with the C_E of 1.7 x 10^{-3} found in the water budget analysis of the present study using 900 mb winds. Rosenthal uses a variable coefficient:

$$C_E - 1.1 \times 10^{-3} + 4 \times 10^{-5} |V|$$

where $|V|$ is the 10 meter wind in meters per second.

Using this formula and assuming that the 10 meter wind is about 80% of the 900 mb wind, the mean surface C_E inside 2^o radius computed from the typhoon composite data is about $C_{E_{sfc}} \simeq 2.0 \times 10^{-3}$. This is equivalent to a C_E applied to the 900 mb winds of about $C_e = 1.6 \times 10^{-3}$. Therefore, the Rosenthal model also compares well with the 900 mb C_E estimated from the water budget study.

Analysis of evaporation derived from the h budget (Table 6.5) indicates that the 1.7×10^{-3} value may be 10-20% too high. It seems that a constant value of C_E of about 1.5×10^{-3} applied to 900 mb winds is realistic for most purposes. Since reasonable surface fluxes of sensible heat are obtained by using a constant Bowen ratio of .10, it appears that the coefficient of sensible heat transfer (C_s) may be assumed as approximately equal to C_E.

There are at least 3 factors which may account for the apparent overestimate of sea surface sensible heat flux by Malkus and Riehl (1960). One is that an assumption of adiabatic expansion in a turbulent boundary layer is probably not valid (Kraus, 1972). Also, the accuracy of static temperature measurements in the high wind regions near the core of tropical cyclones is questionable. Of greater importance, however, are the depth and vertical motion characteristics of the inflow layer. About 60% of the inflow at 2^o radius is above 950 mb. Since cloud base is typically at or below 950 mb, it is safe to say that no more than a third of the inflow inside 2^o is occurring in the subcloud layer. In addition, the cloud base mass flux in the r = 0.7-2^o region is typically 4-5 times larger than the mean vertical motion at cloud

base. The result is that air does not simply flow in expanding nearly adiabatically, go up in the eyewall, and depart. There is an enormous amount of mass recycling in the lower levels at all radii which results in liberation of the latent heat of condensation and induced environmental subsidence of warm, dry air. Above cloud base adiabatic assumptions are clearly invalid. The subcloud air may be recycled vertically several times before reaching the eyewall.

In this study it is assumed that there is no flux of dry static energy (s) across cloud base. (This is not necessarily correct - there is some evidence that clouds are typically negatively buoyant at cloud base implying a downward flux of s at that level). Under the above conditions the sea surface flux of s required to maintain the observed nearly isothermal surface temperature profile is just the flux required to warm part of the mean inflow below 950 mb. Since there is no significant horizontal temperature gradient at 950 mb, only a portion of the subcloud layer is warmed. For a typical storm with a central pressure of about 960 mb, subcloud inflow layer from 0-2° with a depth of 50 mb and a mean radial wind of 5 m/sec, the air would take an average of about 0.4 days to travel from 2° to the eyewall. In that time it would expand about 40 mb resulting in an adiabatic cooling of almost 4°C. Neglecting friction and assuming about 1-2° C of radiational cooling, a net cooling of nearly 12° C/day should occur. Since the surface air at the core is only about 1° C cooler than air at 2° radius, a maximum sea surface to air sensible heat flux sufficient to maintain equilibrium may be assumed:

Flux S = $(\Delta Q)\ C_p \frac{\Delta P}{g}$ where ΔQ is the cooling rate of the air.

$$\text{Flux S} = \left(\frac{11^{\circ}\ C}{\text{day}}\right)\left(\frac{.24\ \text{cal}}{\text{gm}\ ^{\circ}C}\right)\left(\frac{50}{.98}\ \frac{\text{gm}}{\text{cm}^2}\right) = 135\ \frac{\text{cal}}{\text{cm}^2\ \text{day}}$$

The mean surface flux of S inside 2° radius is estimated in the h budget study to be about 90 $\frac{\text{cal}}{\text{cm}^2\ \text{day}}$. Since the mean depth of the subcloud inflow layer being warmed in the above calculation is probably substantially less than 50 mb, the two values agree well. The apparent miscalculation made by Malkus and Riehl is estimating the surface S flux was in assuming that the entire mass inflow had to be warmed in that manner. Latent heating and subsidence of high s air from middle levels are substantial above cloud base where much of the inflow occurs.

It is clear that the sea surface is an important source of both sensible and latent heat to a tropical cyclone. A constant value of $C_e = C_s \sim 1.5 \times 10^{-3}$ applied to the 900 mb winds gives reasonably realistic sea surface to air fluxes of latent and sensible heat when used in Eqs. 5.2 and 6.18.

7. ANGULAR MOMENTUM BUDGET

Analysis of the angular momentum budget of a tropical cyclone reveals the manner in which the tangential circulation is maintained and many features concerning the nature of vertical transports of momentum in active convective regimes. In this section the angular momentum budget of the composite steady state typhoon is examined for the region extending from the storm center to 10^{o} radius. Particular attention is focused on the role of deep convection in maintaining the observed circulation.

It is best to compute the angular momentum and vorticity budgets in a stationary coordinate system with the storm at its center. A coordinate system moving with the storm, while theoretically desirable, involves the computation of many additional terms which are difficult to estimate with the present data set. These terms are not negligable. It is felt that the use of a moving coordinate system would introduce multiple complexities and inaccuracies which would tend to degrade the quality of the budget analysis. Therefore, this budget study is performed in stationary coordinates.

7.1 Budget Equations

The conservation of relative angular momentum equation in cylindrical stationary coordinates is:

$$\frac{dm}{dt} = - r f V_r - \frac{1}{\rho} \frac{\partial p}{\partial \theta} + r F_\theta \qquad (7.1)$$

where $m = V_\theta \cdot r$ = relative angular momentum, and

$$F_\theta = \frac{1}{\rho} \frac{\partial T_{\theta z}}{\partial z} \qquad (7.2)$$

The local rate of change of the total angular momentum (M) of a hollow cylinder with inner and outer radii of r_1 and r_2 respectively and extending vertically from level P_1 to P_2 is:

$$\frac{\partial M}{\partial t} = \frac{1}{g}\int_{P_1}^{P_2}\int_{r_1}^{r_2}\int_{o}^{2\pi} (r^2 f V_r)\, d\theta\, dr\, dp + \frac{1}{g}\int_{P_1}^{P_2}\int_{r_1}^{r_2}\int_{o}^{2\pi} F_\theta\, r_2\, d\theta\, dr\, dp$$

$$+ \frac{1}{g}\int_{P_1}^{P_2}\int_{o}^{2\pi} [r_2(mV_r)_2 - r_1\,(mV_r)_1]\, d\theta\, dp \qquad (7.3)$$

$$+ \int_{r_1}^{r_2}\int_{o}^{2\pi} [\,(\omega rm)_{p_2} - (\omega rm)_{p_1}\, d\theta\, dr$$

Since the storm is assumed to be in steady state, the term on the left of Eq. 7.3 is assumed to be zero. The second term on the right of Eq. 7.1 vanishes due to integration around a closed path. Equation 7.3 merely states that the convergence of relative angular momentum into a volume (3rd and 4th terms, right hand side (RHS)) is balanced by the increase of relative angular momentum by the radial flow (1st term, RHS) and the surface frictional dissipation (2nd term, RHS).

7.2 Method of Solution

Values of V_θ V_r are computed for each individual sounding and composited as before to obtain an estimate of the total horizontal flux of relative angular momentum ($\overline{V_r V_\theta} \cdot \overline{r} \simeq \overline{V_r\, V_\theta r}$). Past angular momentum budget studies have assumed that the Coriolis torque term ($\overline{fV_r\, r}$) integrates to zero over the total volume since the net radial mass flux

is zero for a steady state storm and near zero for any storm (Palmén and Riehl, 1958; Pfeffer, 1958; Hawkins and Rubsam, 1968). This approximation is good at inner radii where f varies little. As pointed out by Anthes (1974), however, a prevailing north wind component can cause an appreciable net spin-up of a storm at outer radii. The opposite is true for net southerly flow. Therefore, it is desirable to compute a value of $\overline{fV_r r}$ for each grid space in the storm. Computation of this term presents a problem since f values vary substantially with storm location, and the data network is not symmetrical. This could lead to biases in the composite if $\overline{fV_r r}$ is computed for each sounding. Therefore, the term is estimated by applying the average storm latitude of 21.7 ^{o}N and determining north-south differences from this. The mean value of f for each grid box at each level is multiplied by the mean values of r and V_r for that grid box. The resulting values of $\bar{f} \cdot \bar{V}_r \cdot \bar{r}$ are averaged around each radial band to give a mean value at each level and radius. It is felt that this mean value of $\bar{f} \cdot \overline{V_r} \cdot \bar{r}$ is a reasonable approximation of the total Coriolis torque $(\overline{fV_r r})$.

Surface frictional dissipation is computed using the formula:

$$\text{Dissipation} = \rho C_D V_\theta V r \qquad (7.4)$$

where V is the total wind speed. 900 mb wind values are used to reduce the land effects on the low level wind measurements. To compute C_D the total dissipation from 0-4^{o} radius is estimated as a residual in Eq. 7.3 for the surface to 100 mb volume. The mean value of the 900 mb C_D for 0-4^{o} is 1.4×10^{-3}. Values of C_D at outer radii are reduced slightly. These C_D values are obtained by applying Deacon's empirical formula based on 10 meter winds (Roll, 1965):

$$C_D = 1.1 \times 10^{-3} + 4 \times 10^{-5} |V| \qquad (7.5)$$

(V in $\frac{m}{sec}$)

to the 900 mb winds and adjusting the results with a proportionality constant of .74 to fit the estimated mean C_D for the 0-4° region. The use of this variable drag coefficient gives a better fit with the observed momentum budget data than does use of a constant coefficient such as those estimated in the water and moist static energy budget analyses or by Riehl (1963). This does not necessarily imply that the coefficients of momentum, sensible heat, and latent heat transfer must be different. Indeed they appear to be quite similar in magnitude. However, there is no physical reason for believing that they are identical. It is difficult to estimate this momentum drag coefficient from the data alone due to the relatively small magnitude of the frictional term compared to the other terms at large radii. Therefore, the choice of a commonly used estimate of C_D (adjusted for 900 mb winds) which gives reasonable results seems justified.

7.3 Vertically Integrated Balance

Figures 7.1-7.5 show the total ($\overline{V_r V_\theta}$) and mean circulation ($\overline{V}_r \overline{V}_\theta$) horizontal transports of relative angular momentum at 2°, 4°, 6°, 8° and 10°. The total transport at 2° had to be adjusted to balance the estimated 0-2° surface dissipation. This results from an unrealistically large outflux of momentum indicated by the data. The adjusted profile and the 4° profile show that the momentum transport inside 4° radius is accomplished primarily by the mean circulation for steady state storms. Riehl (1961) reported similar findings. At larger radii, however, a substantial eddy influx of relative angular

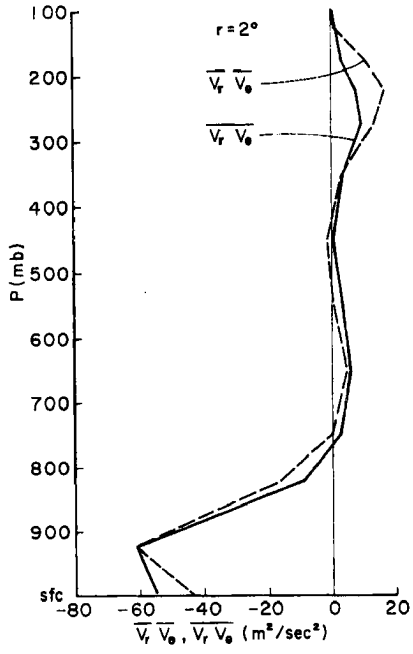

Fig. 7.1. Total horizontal flux of relative angular momentum divided by radius ($\overline{V_r V_\theta}$) and flux by mean circulation ($\overline{V_r} \cdot \overline{V_\theta}$) at r=2°. The difference between the curves is the horizontal eddy flux.

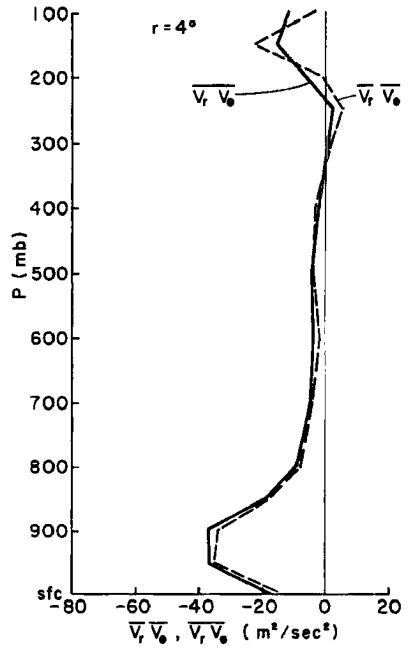

Fig. 7.2. Same as Fig. 7.1 for r=4°.

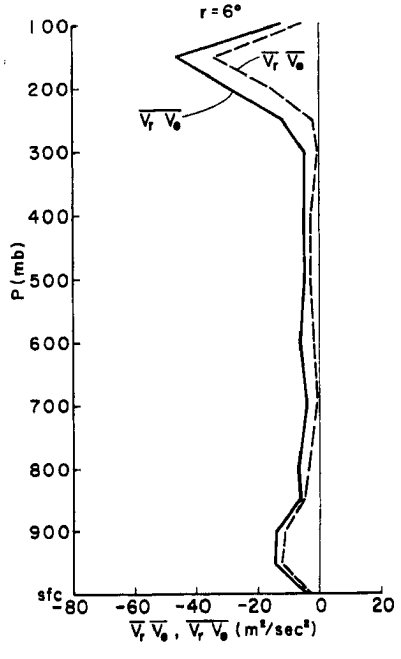

Fig. 7.3. Same as Fig. 7.1 for r=6°.

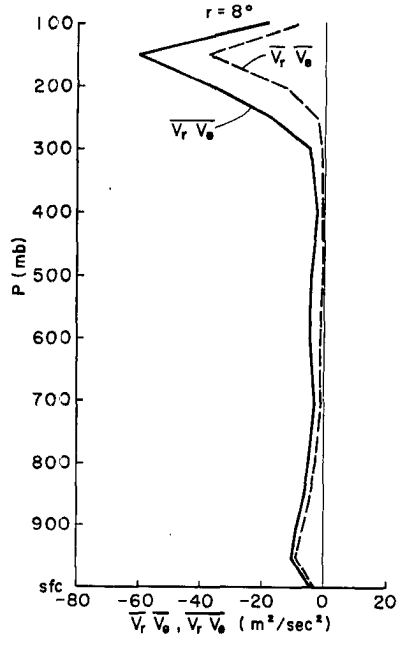

Fig. 7.4. Same as Fig. 7.1 for $r=8^{o}$.

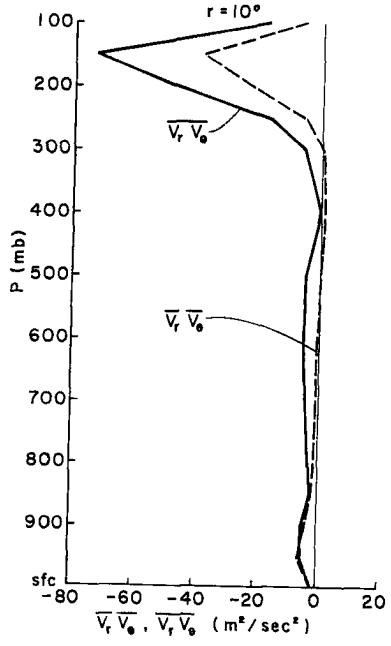

Fig. 7.5. Same as Fig. 7.1 for $r=10^{o}$.

momentum occurs due to the intense anticyclonic winds in the outflow jets. The eddy momentum influx is actually an eddy outflux of negative relative angular momentum. The percentage of the net relative angular momentum import achieved by the mean circulation is only 58% at 6^{o} and drops to 42% at 10^{o} radius. Eddy influxes of angular momentum also have been reported by Black and Anthes (1971), Pfeffer (1958), and Palmén and Riehl (1957).

The Coriolis torque term (fV_r r) does not integrate to zero over the storm volume due to the prevailing southerly winds in which N.W. Pacific typhoons usually are imbedded (see Fig. 3.1). It is clear that the large scale southerly wind flow acts to spin down the storm due to the eddy Coriolis torque. From $0-2^{o}$ this eddy spin down is very small

due to the small variation of f in that volume, and it is neglected in the computations. The effect increases greatly with radius, however. Figure 7.6 shows the vertically integrated convergence of angular momentum, the eddy spin down due to the Coriolis torque, and the computed frictional dissipation. At inner radii the convergence of relative angular momentum is balanced primarily by frictional dissipation. In the storm outer regions the frictional loss is small, and the balance is primarily between relative momentum convergence and the eddy Coriolis torque spin down. Note that the convergence of relative angular momentum is not sufficient to balance the two sink terms at large radii. Since the Coriolis torque term is believed to be known less accurately than the other 2 terms, it is adjusted (dashed line) to give momentum balance for use in the more detailed analyses below. It should be noted that it is quite possible that the terms should not achieve perfect balance at large radii. It remains to be shown whether a typical asymmetrical storm moving across a fixed grid is really in steady state at all radii.

7.4 Level by Level Momentum Budget

In the lowest levels of tropical cyclones, relative angular momentum is created primarily by the Coriolis torque acting upon the radial inflow. (Import of relative angular momentum in the lower troposphere is negligible at large radii). A portion of this relative angular momentum is lost to the sea due to frictional torque. The rest of the high relative momentum air is transported upward within the storm and exported above 300 mb in the outflow layer, primarily in strong jets. The outflowing air loses relative angular momentum due to the Coriolis torque and arrives at outer radii with strong anticyclonic velocity due

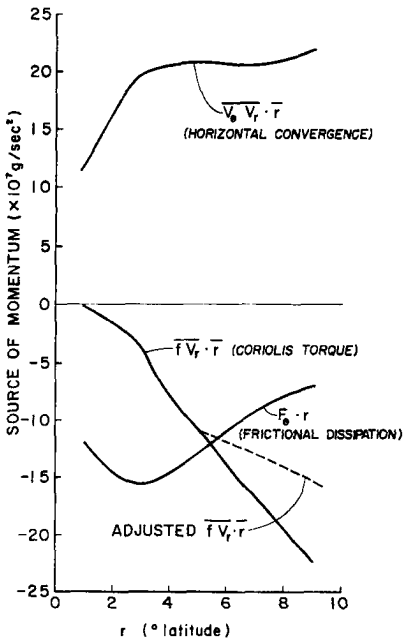

Fig. 7.6. Vertically integrated angular momentum budget terms: horizontal convergence of momentum ($\overline{V_\theta V_r} \cdot r$), surface dissipation ($\overline{F_\theta} \cdot r$) and net spin down by Coriolis torque ($\overline{f}\ \overline{V_r}\ \overline{r}$). Dashed line is adjustment to Coriolis term to achieve balance.

to the frictional losses of momentum to the sea surface. The outflow jets exhibit above average anticyclonic velocities at all outer radii and are responsible for the large eddy import of relative angular momentum in the upper levels (Figs. 7.1 - 7.5). Over the large storm domain (0-10° radius) this eddy sink of negative relative angular momentum (source of positive momentum) is required to balance the overall eddy Coriolis torque spin down resulting from the deep southerly flow and the surface losses. Without this momentum source the entire storm volume would spin down unless it could achieve an equilibrium with weaker surface winds (and frictional dissipation) and stronger upper level anticyclonic flow than are observed.

The relative angular momentum budget of the composite typhoon is shown in Figs. 7.7 and 7.8 for the 0-10° radius region. In Fig. 7.7 the units are momentum gain per unit area. The upper number in each box is the convergence of relative angular momentum by the horizontal circulation. The arrows adjacent to these numbers show the direction of the momentum flux. The middle value is the Coriolis torque spin up, and the lowest value shows the vertical transport required to achieve balance. The Coriolis torque is assumed to integrate vertically to zero inside 2°. Transports of relative angular momentum at r = 0.7° are assumed to be the mean transports which arise from the radial wind profile assumed in the moist static energy budget analyses.

In the central core region (0-.7°) the frictional dissipation accounts for only about 1/3 of the relative angular momentum converged in the lower troposphere. The rest is transported vertically and exported above 300 mb. The Coriolis torque is almost negligible in this region due to the small radius. The vertical momentum transport is constant.

The inner rainband area (.7-2°) shows greater low level frictional dissipation and increasing importance of the Coriolis term. About 60% of the momentum converged or generated below 800 mb is dissipated while the rest is transported vertically to the outflow layer. The vertical transport decreases with height from 800-300 mb.

The 2-4° outer rainband region is quite different from the inner regions. Over 90% of the low level (surface - 800 mb) angular momentum accumulation is dissipated at the surface. Upward momentum transport increases with height in the middle levels due to convergence of relative

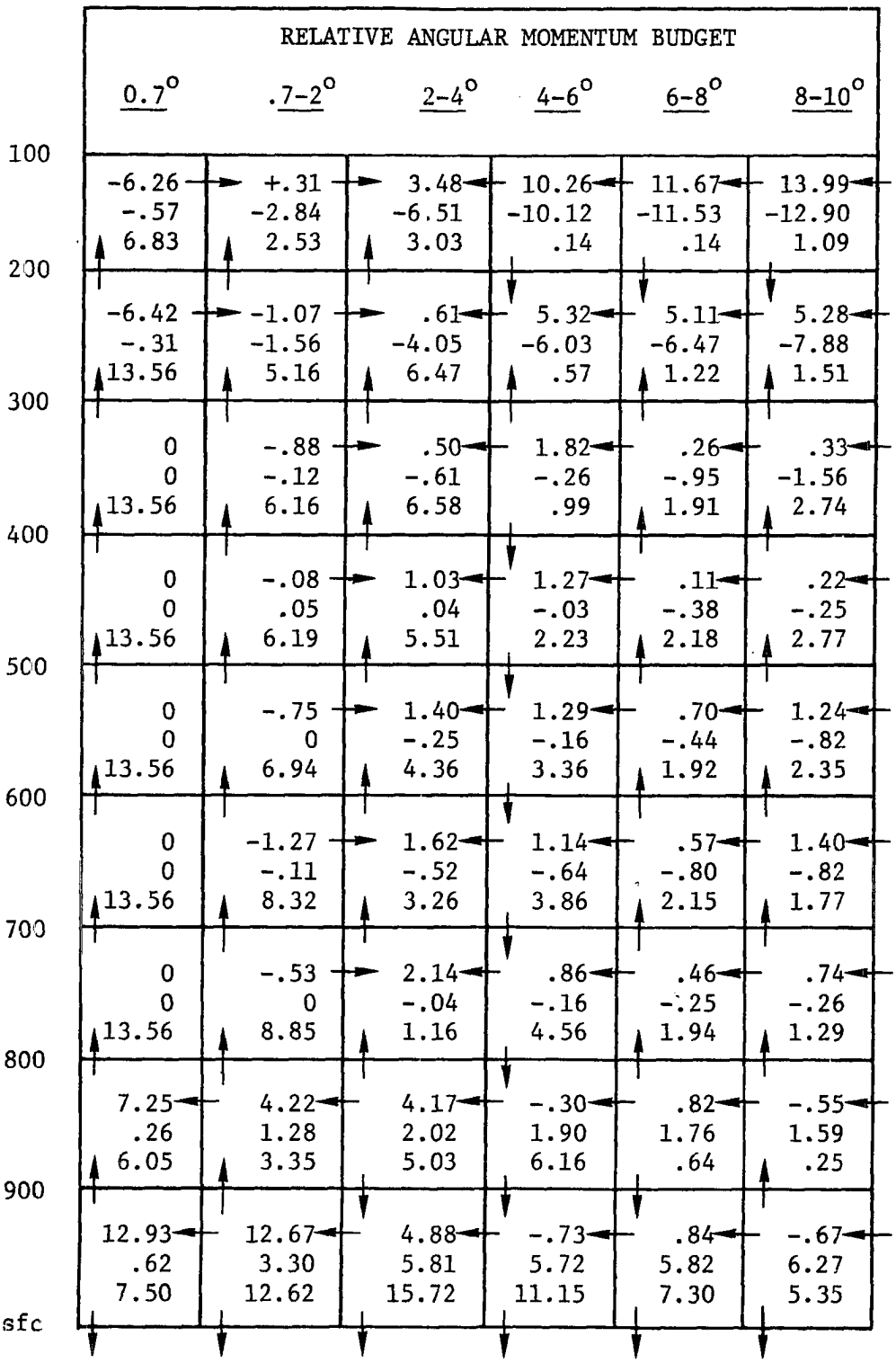

Fig. 7.7. Gain of angular momentum per unit area. Top number is the convergence due to the horizontal circulation (arrows show direction of transport). Middle term is the Coriolis torque spin-up. Third number is the vertical transport. Surface dissipation shown at bottom of figure. Units = gm/sec^2.

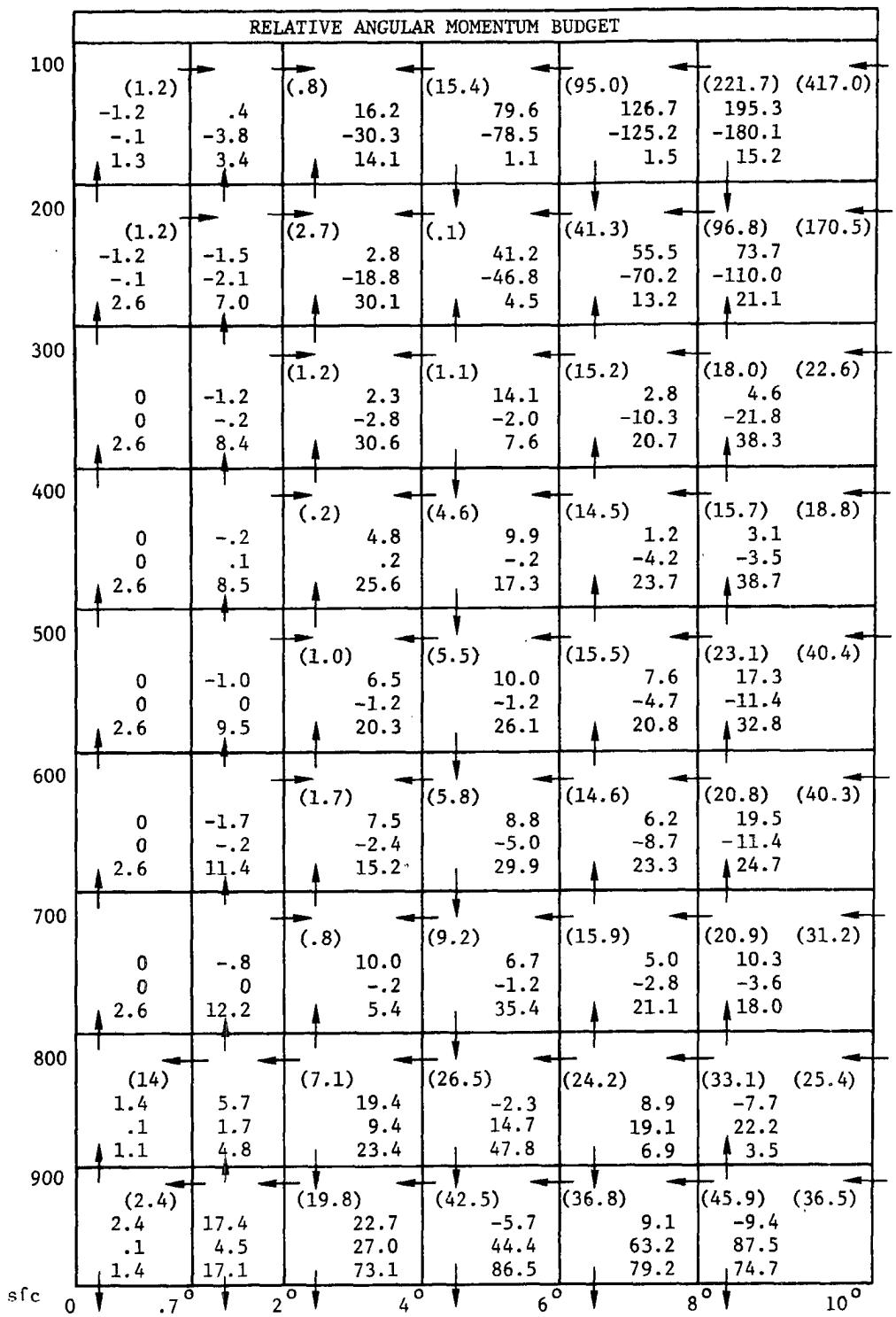

Fig. 7.8. Total gain of angular momentum. Numbers in parenthesis indicate horizontal transport (arrows show direction). The second number in each box is convergence due to horizontal transport. The third number is the Coriolis torque spin-up and the fourth number is the vertical transport. Surface dissipation is shown at the bottom of the figure. Units = 10^{22} gm cm^2/sec^2.

angular momentum. In the outflow layer the Coriolis torque sink prevails and is balanced by the upward momentum transport.

The "moat" region (4-6^{o}) shows downward momentum transport at and below 400 mb. This is related to the mean subsidence which is observed at these levels. Convergence of relative angular momentum is strongest in the outflow layer where it nearly balances the Coriolis torque sink. Weak momentum convergence in the middle levels and the Coriolis source term in the lower troposphere balance most of the surface dissipation.

Beyond 6^{o} radius the outflow layer is in near balance between the convergence and Coriolis terms. In the lower troposphere most of the Coriolis torque generation balances the surface dissipation. The middle levels show a weak Coriolis term sink at all levels resulting primarily from the southerly flow. This sink is more or less balanced by weak relative momentum convergence. Upward transport occurs from 800-300 mb.

Figure 7.8 shows the angular momentum budget in units of total angular momentum transport or accumulation (x10 ^{22} gm cm^{2}/sec^{2}). The upper number in parenthesis shows the horizontal transport, the second is the accumulation due to horizontal transports, and the 3rd and 4th numbers are the Coriolis torque spin up and vertical flux, respectively. It is evident from Fig. 7.8 that the small inner 2^{o} region does not play a large role in the angular momentum budget of the entire 0-10^{o} circulation. This may be why the inner core circulations can vary so much for similar outer flow features. Frictional dissipation from 0-2^{o} is only 5-6% of the 0-10^{o} dissipation despite the strong surface winds in the inner region. The other terms show similar relative magnitudes. This results from the relatively small area of the core region, the radial dependence of

angular momentum and the increase in the eddy f term with north-south distance from the center.

From the above one may conclude that the large scale ($0-10^{o}$) storm circulation does not depend upon sources and sinks of momentum in the core region ($0-2^{o}$). However, the dynamic effects of the inner storm upon the outer flow may affect the balance of the entire region. For example, if the upper level outflow did not occur in the observed anitcyclonic jets creating eddy import of momentum, the anticyclone would strengthen reducing the momentum of the total circulation volume. The effects of the inner core circulation upon the structure of the outflow layer are unknown, but they could be significant.

7.5 Vertical Transport of Relative Angular Momentum

Although clouds are known to cause stresses in the troposphere through momentum transport (Gray, 1966), the roles of clouds in the vertical transport of momentum are poorly understood. Most cumulus parameterization schemes omit such transports altogether greatly hampering their use in studies of tropical cyclones which have significant cumulonimbus activity and unusually large amounts of angular momentum. Gray (1967) has shown that cumulus momentum transport is an important feature of the inner core circulation of tropical cyclones.

The total vertical flux of relative angular momentum (m) occurring in a region where all upward vertical motion is assumed to occur in clouds may be expressed:

$$\overline{\omega m} = \overline{\omega}_c \, \overline{m}_c + \tilde{\omega} \, \tilde{m} \qquad (7.6)$$

where $\overline{\omega}_c$ is the total cloud mass flux at a level and $\overline{m}_c$ is the effective mean cloud angular momentum for all clouds existing at that level. The tilda (~) refers to extra-cloud (cloud environment) average values. Furthermore, the mean vertical motion ($\overline{\omega}$) is just:

$$\overline{\omega} = \overline{\omega}_c + \tilde{\omega} \tag{7.7}$$

Equation 7.6 may be written

$$\overline{\omega m} = \overline{\omega}_c \overline{m}_c + \overline{\omega}\tilde{m} - \overline{\omega}_c \tilde{m} \tag{7.8}$$

In regions where the active cloud updrafts are only small percentages of the total area (valid for $r > .7^o$), $\tilde{m} \sim \overline{m}$. Substituting this into Eq. 7.8 and rearranging:

$$\overline{m}_c = \frac{\overline{\omega m} - \overline{\omega}\,\overline{m}}{\overline{\omega}_c} + \overline{m} \tag{7.9}$$

All terms on the right side of Eq. 7.9 except $\overline{\omega}_c$ are observed or computed in the preceding momentum budget analysis. $\overline{\omega}_c$ is taken from the moist static energy budget analysis. Although that study was done in moving coordinates, the cloud mass fluxes should be identical in stationary coordinates.

The total required vertical angular momentum transports for the regions from $0.7\text{-}8^o$ radius are shown in Figs. 7.9-7.12. The area inside 0.7^o is omitted for the same reasons discussed in the moist static energy analysis, and the $8\text{-}10^o$ region is assumed to be essentially similar to the $6\text{-}8^o$ region. Also shown are the vertical transports of momentum by the mean circulations and the differences between the mean and total transports (the eddy fluxes). It is clear that the vertical eddy fluxes

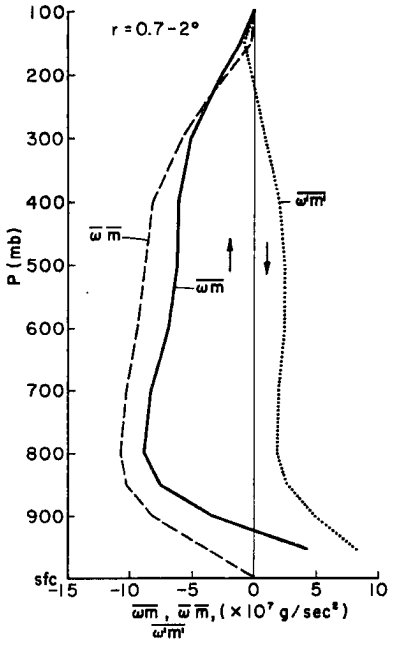

Fig. 7.9. Total vertical flux of relative angular momentum ($\overline{\omega m}$), flux by mean circulation ($\overline{\omega}\,\overline{m}$) and eddy flux ($\overline{\omega' m'} = \overline{\omega m} - \overline{\omega}\,\overline{m}$) for 0.7-2° region.

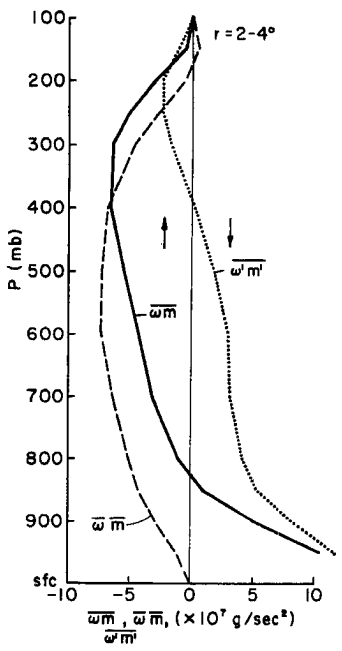

Fig. 7.10. Same as Fig. 7.9 for 2-4°.

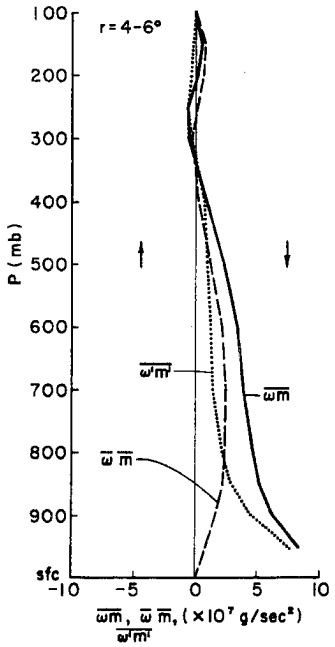

Fig. 7.11. Same as Fig. 7.9 for 4-6°.

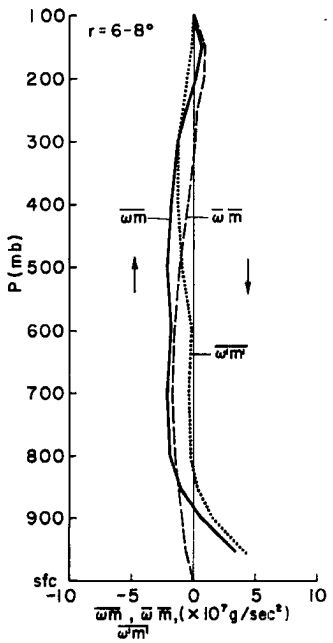

Fig. 7.12. Same as Fig. 7.9 for 6-8°.

are significant. In the lowest 100-200 mb of each region there are large downward eddy momentum fluxes. Above the boundary layer the total upward transport generally is less than the mean circulation transport in the lower levels and greater in the upper troposphere. From 6-8^{o} the total transport is slightly greater than the mean transport in the lower levels, perhaps due to a small underestimate of the surface dissipation. Above the boundary layer these eddies cannot be explained by classicial down-gradient mixing. There are downward eddy momentum fluxes in the lower half of the troposphere in most regions despite gradients of momentum decreasing with height (shown in Figs. 7.13 - 7.16).

It is hypothesized that the observed vertical momentum fluxes result primarily from cumulus momentum transports. Figures 7.13 - 7.16 show vertical profiles of the mean angular momentum of all cloud types $\overline{m}_c$ determined from Eq. 7.9. Also shown are the observed mean angular momentum profiles. Several features stand out. Despite different environmental momentum profiles, the cloud momentum in each region is relatively constant from about 850 mb to 300-400 mb or so. The bulge in the cloud momentum from 700-900 mb in the 6-8^{o} region may result from a small error in the surface friction as mentioned above. The resulting overestimate of the total upward momentum flux in the lower troposphere would result in an unrealistically high value of $\overline{m}_c$ required for balance.

A sharp decrease in $\overline{m}_c$ below about 850 mb is evident in each region. There are at least two reasonable explanations. The large number of shallow clouds indicated in section 6.5 may have significantly lower angular momentum values in the lowest levels than the clouds which

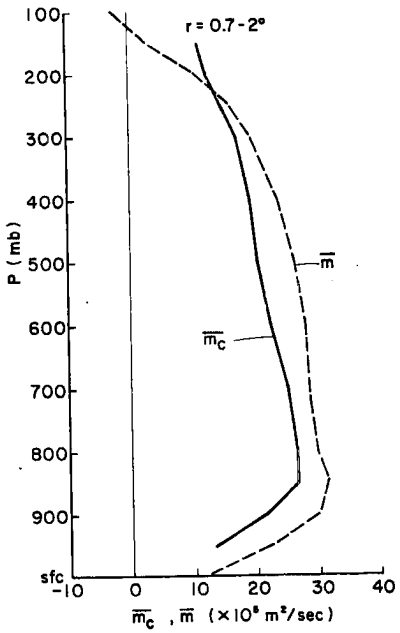

Fig. 7.13. Vertical profile of mean relative angular momentum ($\overline{m}$) and effective mean momentum of all clouds existing at each level ($\overline{m_c}$) from Eq. 7.9, 0.7-2° region.

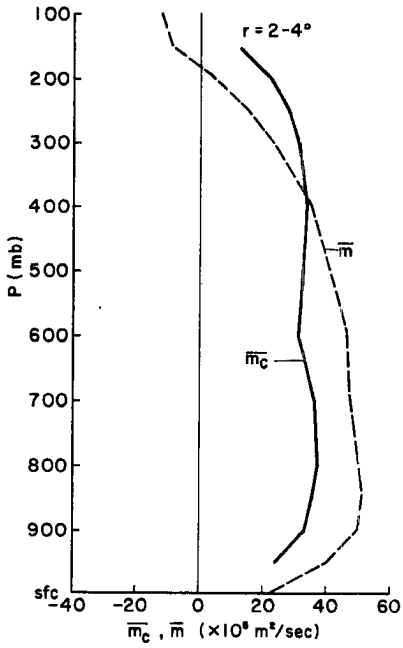

Fig. 7.14. Same as Fig. 7.13 for 2-4°.

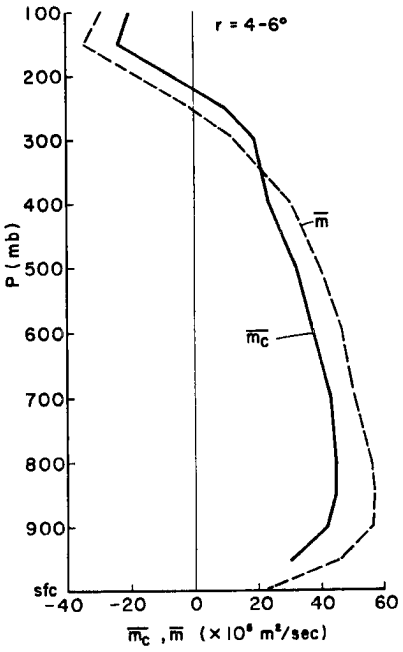

Fig. 7.15. Same as Fig. 7.13 for 4-6°.

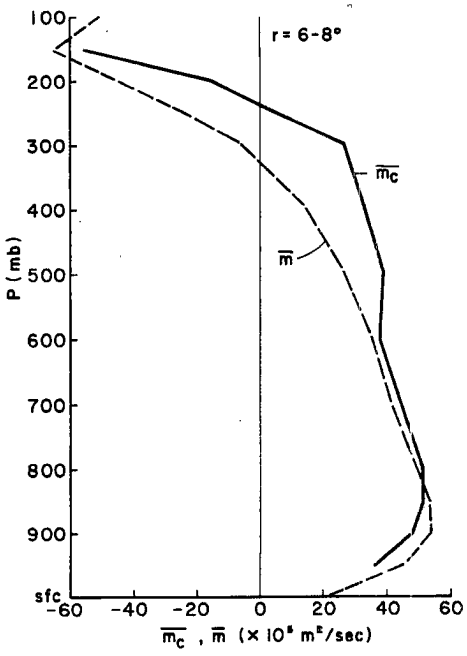

Fig. 7.16. Same as Fig. 7.13 for 6-8°.

detrain above 850 mb and/or a large portion of the low level momentum fluxes may result from dry turbulent mixing processes causing an apparent decrease in $\bar{m}_c$. Both factors probably contribute since shallow clouds and turbulent boundary layer processes are closely related. The shallow clouds may be thought of as simple extensions of turbulent mixing in the presence of extremely high relative humidities where latent heat acts as a feedback to deepen the mixing length scale. As a first approximation it may be assumed that the above processes are contained below 850 mb and that the $\bar{m}_c$ of all clouds detraining above that level remains relatively constant from 850 mb down to cloud base (950 mb).

Note that at the 850 mb level $\bar{m}_c$ is less than $\bar{m}$ in all regions. This means that the clouds have a lower mean V_θ than the large scale flow. Values of $V_{\theta\ \text{cloud}} - \bar{V}_\theta$ are shown in Table 7.1.

TABLE 7.1

$V_{\theta\ \text{cloud}} - \bar{V}_\theta$ at 850 mb (m/sec)

0.7-2°	2-4°	4-6°	4-8°
-2.9	-4.8	-2.2	-0.2

The average difference is about 2.5-3.0 m/s although the 6-8° value seems low. Inspection of Figs. 7.13-7.16 shows that $\bar{m}_{c_{850}}$ is about equal to the cloudbase environmental momentum ($\bar{m}_{950}$) from 0.7-6° radius. If the 700-900 mb level bulge in m_c from 6-8° proves to be erroneous, this result would be valid there as well. It appears that clouds detraining above 850 mb transport mean cloud base momentum upwards while

shallow clouds and dry mixing accomplish the bulk of the low level momentum transports.

Above 300-400 mb $\overline{m}_c$ bends sharply toward the $\overline{m}$ curve. This seems to indicate that clouds lose their dynamic ability to conserve momentum in the vicinity of their zero buoyancy levels. As the Cb clouds overshoot into the strong anticyclone, they detrain and mix with the environmental air and rapidly acquire environmental momentum. Their tops are blown off in the strong vertical shear. The $\overline{m}$ profile obviously is affected by the detraining momentum as well. Clouds detraining from 800-300 mb probably behave in a similar manner, but their effects on the middle levels of the $\overline{m}_c$ profiles are much smaller than those of the Cb clouds in the outflow layer for three reasons. These middle height clouds detrain at levels where vertical wind shears are weak and cloud momentum is not too different from $\overline{m}$. Second, the rates of mass detrainment in the middle levels are small compared to the total cloud mass flux at those levels. This is not true in the outflow layer. Finally, the middle height clouds do not overshoot significantly so that $\overline{\omega}_c$ at a middle level is composed almost entirely of active buoyant clouds detraining above. This is in contrast with the outflow layer above 300 mb where overshooting Cb clouds detraining and mixing with the environment compose appreciable fractions of $\overline{\omega}_c$.

It is interesting that $\overline{m_c}$ decreases slightly with height at all radii. There is no indication that the $\overline{m_c}$ profiles lean towards the $\overline{m}$ profiles in the 0.7-8^o regions as would be expected for large amounts of entrainment of environmental air into the clouds. Since entrainment is known to occur, its effect on the $\overline{m_c}$ profiles must be counteracted by some other phenomenon. One possibility is that the deeper Cb clouds

tend to exhibit slightly lower cloud base angular momentum values than the clouds detraining at middle levels. This would cause $\overline{m_c}$ to decrease with height as the Cb clouds increasingly dominate the total cloud mass flux. Such a hypothesis requires the Cb clouds either to have "deeper roots" in the sub-cloud layer than other clouds or to exist preferentially in regions of low V_θ. These are possible. However, the links between boundary layer dynamics and cloud mass and momentum fluxes are poorly understood, and a definitive answer cannot be obtained from the present data.

The above analysis suggests an overall picture of vertical momentum fluxes in tropical cyclones which may prove useful as a parameterization philosophy for other tropical weather systems. In the presence of low level convergence, deep clouds exist. These clouds transport cloud base momentum upwards conserving most of their momentum until they lose buoyancy. They then detrain rapidly, mix with the surrounding air, and begin to acquire environmental momentum. This process may be approximated by assuming a protected core for the convection which ends near the zero buoyancy level. Environmental subsidence may be approximated by a smooth down-gradient flux of momentum. The combination of the cloud and environmental fluxes gives the total transport of momentum by deep clouds at any level.

In the levels below about 850 mb much of the momentum transport is achieved through turbulent mixing in both clear air and shallow clouds. From a momentum viewpoint one may assume that these two processes are essentially similar and that the presence of shallow clouds acts only to increase the depth of the mixing. Since the amounts of dry turbulence and low level cloudiness are related to the low level wind and

moisture fields, the momentum fluxes by these processes may be parameterized in terms of observable large scale quantities. The total momentum fluxes in the surface - 850 mb layer would be the sum of these turbulent fluxes and the fluxes by the deeper clouds described above.

A model of vertical momentum flux based on mean vertical transports plus down gradient eddy mixing is completely inadequate. The environmental gradient of momentum affects the total transport only in terms of the subsidence between the clouds. Down gradient transports of momentum by mechanical turbulence are probably very small above the boundary layer. The eddies involved in the vertical momentum fluxes are of the scale of Cb clouds, not a few meters. The degree to which all Cb clouds conserve their cloud base source momentum is open to question since convection in isolated Cb clouds may differ substantially from the rainband type of convection which predominates in tropical cyclones. Nevertheless, it appears that vertical transports of momentum by cumulus clouds must be parameterized if one wishes to obtain a physically realistic model of a tropical convective regime.

8. KINETIC ENERGY BUDGET

Tropical storms generate and dissipate huge quantities of kinetic energy (K). These storms maintain strong warm core upper level radial baroclinicity. Geopotential heights slope downward with decreasing radius except in the outer outflow layer where the opposite is true. The kinetic energy is generated by down gradient flow. This is primarily due to the radial circulation which is generally inward below 300 mb and outward above that level. Observed mean radial winds are generally down gradient at all levels and hence generate kinetic energy at all levels. Frictional dissipation is probably strongest in the boundary layer, but a significant amount of internal dissipation of K probably occurs at other levels. The available potential energy is maintained primarily by the release of latent heat in the highly convective core region, although sea surface fluxes of energy and radiational cooling are also important. A more thorough discussion of the maintenance of the observed static energy structure and gradients is presented in the moist static energy budget analysis. Most of the latent heat released is used to raise the air in cumulus clouds increasing its potential energy. Since the upward moving air in the clouds is warmer than the subsiding air between them, there is a net conversion of potential energy to kinetic energy. This cumulus cloud scale conversion of potential to kinetic energy is on a quite different scale than the synoptic scale rising and sinking of warm and cold air masses which occurs in mid-latitude cyclones.

There have been several empirical studies of tropical cyclone kinetic energy (K) budgets (Hawkins & Rubsam, 1968; Miller, 1962; Riehl & Malkus, 1961; Palmén, 1958; and Palmén & Jordan, 1955). These studies

have concentrated primarily on the energetics of the inner few degrees of radius. The latter three studies are the only ones which included the outer storm region (beyond 4^{o} radius), and they neglected eddy horizontal transports of kinetic energy.

The above researchers generally concluded that the eddy horizontal transports and generation of kinetic energy were small and did not play an important role in the storm energy budgets. Numerical modeling studies (Ooyama, 1969; Rosenthal, 1970) have reinforced this viewpoint by showing that the models do not require outside sources of kinetic energy to generate and maintain a mature tropical cyclone.

The results of this study indicate that eddy processes are of great importance in the overall energetics of tropical cyclones and their environments. Although the active convective storm region ($0-4^{o}$) is relatively self-contained with little net horizontal flux of kinetic energy, the outer storm circulation region exhibits a substantial net generation. The net export of K at 10^{o} is quite large and occurs almost completely in the upper troposphere. It is largely an eddy process. It is the author's contention that tropical cyclones act as strong sources of kinetic energy which can play important roles in the energetics of the general circulation. Palmén (1958) reached similar conclusions for a hurricane developing into an extratropical storm over North America. Erickson and Winston (1972) also have implied that typical cyclones export large amounts of K at upper tropospheric levels.

The excess generation of kinetic energy in the outer storm regions is largely the result of eddy generation processes. The mean generation and dissipation of K nearly balance. This apparent balance of mean quantities is one reason that the eddy transports generation and dissipation often have been neglected.

8.1 Budget Equation

The conservation of kinetic energy equation is:

$$\frac{\partial \overline{K}}{\partial t} = - \overline{\nabla \cdot V k} - \frac{\partial \overline{\omega K}}{\partial p} - \overline{V \cdot \nabla \Phi} + \overline{V \cdot F} \qquad (8.1)$$

where K = kinetic energy per unit mass
$\Phi = gz$ = potential energy

This equation was integrated over a cylindrical volume from the surface to 100 mb. No fluxes of K were allowed at 100 mb, and $\omega = 0$ at the sea surface. The term on the left of Eq. 8.1 is the local rate of change of kinetic energy and is zero for the mean steady state storm. The first term on the right is the horizontal flux divergence of kinetic energy. The second term is the vertical flux divergence of K, and the third term is generation of kinetic energy by down gradient flow. The last term is the frictional dissipation. The term friction refers here to all dissipative forces, not merely to drag at the sea surface.

8.2 Method of Solution

The horizontal flux term ($\overline{\nabla \cdot VK}$) is computed by compositing values of $V_r \cdot V^2$ for each individual sounding to obtain estimates of the total flux. This is the same technique used in the other budget studies. It is assumed that horizontal fluxes of K at 2^o radius are equal to the transports by the mean circulation. This is in line with the findings of the previously mentioned studies that eddy fluxes are probably small at inner radii. Since multiplying the radial wind by the square of the wind speed tends to magnify errors in the observations, the total vertically integrated transport of K shows a variation with radius which is less smooth than the observed transports of most other quantities (Fig. 8.1). To obtain realistic results the transports were smoothed as

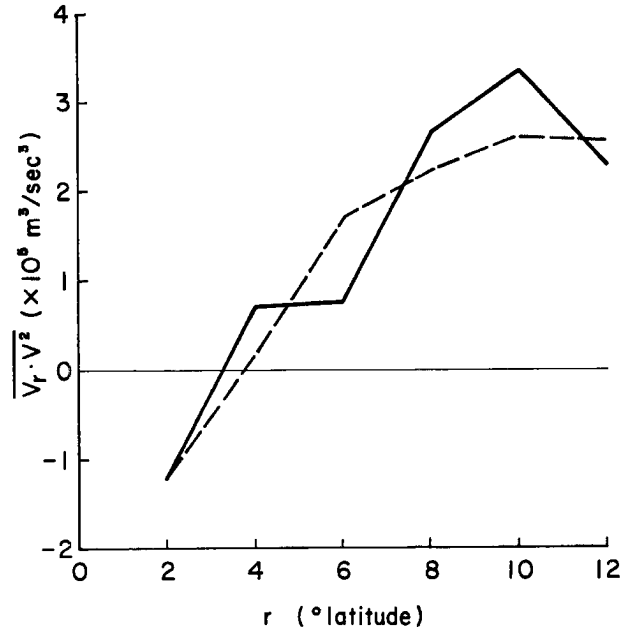

Fig. 8.1. Vertically integrated total horizontal flux of kinetic energy (solid line) and smoothed curve used in budget calculations (dashed line).

shown by the dashed line. The vertical flux term integrates to zero over the storm volume.

It is not possible to measure $\overline{V \cdot \nabla\Phi}$ for each sounding. Therefore, only the generation by the mean circulation ($\overline{V}_r \cdot \overline{\frac{\partial\Phi}{\partial r}}$) is computed. This product is also computed for each octant at each level and averaged. This latter quantity minus $\overline{V}_r \cdot \overline{\frac{\partial\Phi}{\partial r}}$ gives an estimate of the standing eddy generation. Transient eddies of radial generation of K and azimuthal eddy generation ($\overline{V_\theta' \cdot \frac{\partial\Phi'}{r\partial\theta}}$) must be estimated as a residual.

Frictional dissipation of kinetic energy in the boundary layer is estimated by the bulk aerodynamic method using the equation:

$$\text{Dissipation} = \frac{C_D V^3}{\Delta z} \qquad (8.2)$$

The drag coefficient is the same one used in the momentum budget analyses, and V is the 900 mb wind. Internal dissipation of K above the boundary layer cannot be computed. This additional sink is probably substantial.

By solving for vertically integrated values of all the terms of Eq. 8.1 mentioned above, a residual for each radial band is determined:

$$\frac{\partial K}{\partial t} = \text{Horizontal Convergence} + \text{Vertical Convergence} + \text{Mean Generation} - \text{Sfc Dissipation} + R = 0, \text{ where}$$

$$R = \text{Eddy Generation} - \text{Internal Dissipation}$$

This residual is assumed to be the eddy generation minus the internal dissipation of kinetic energy. No budget analysis is attempted for the inner 2^{o} region due to limited height gradient data availability.

8.3 Results

Vertical profiles of the total horizontal transport of kinetic energy are shown in Figs. 8.2 - 8.6. The values have been adjusted slightly by constant factors to correspond with the smoothing of the vertically integrated horizontal fluxes of Fig. 8.1. Also shown are the transports by the mean circulation. At 2^{o} they are assumed to be the same. With increasing radius, however, the eddy fluxes of kinetic energy become larger. At outer radii the eddy fluxes are predominant and occur primarily in the upper troposphere. These eddies are evidence of the high speed outflow jets generated in the outflow layer. Note the large export of K at 10^{o} radius. This export implies a mean excess generation of kinetic energy over the entire $0\text{-}10^{o}$ radius region of 4.8 watts/m^2. This is slightly larger than the 3.4 watts/m^2 annual export of kinetic energy from North America (Kung, 1967). Since there

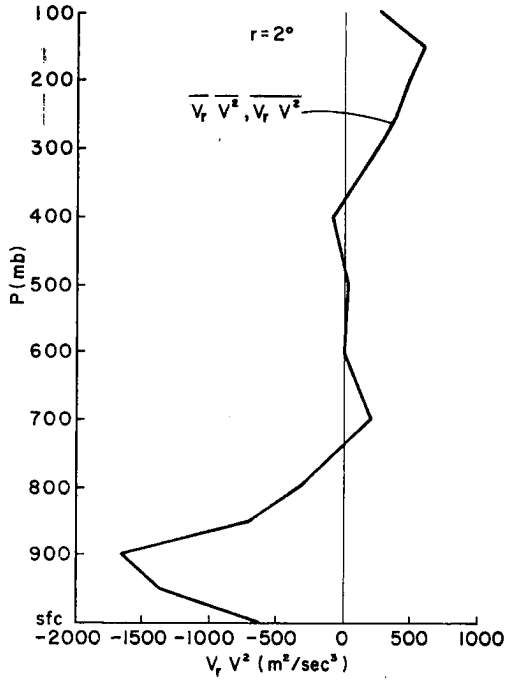

Fig. 8.2. Total horizontal transport of kinetic energy ($\overline{V_r V^2}$) and transport by the mean circulation ($\overline{V_r}\ \overline{V^2}$) at r=2°.

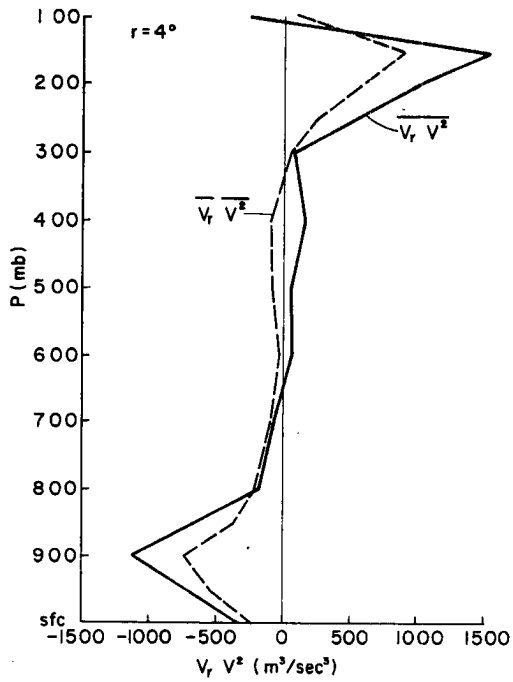

Fig. 8.3. Same as Fig. 8.2 for r=4°.

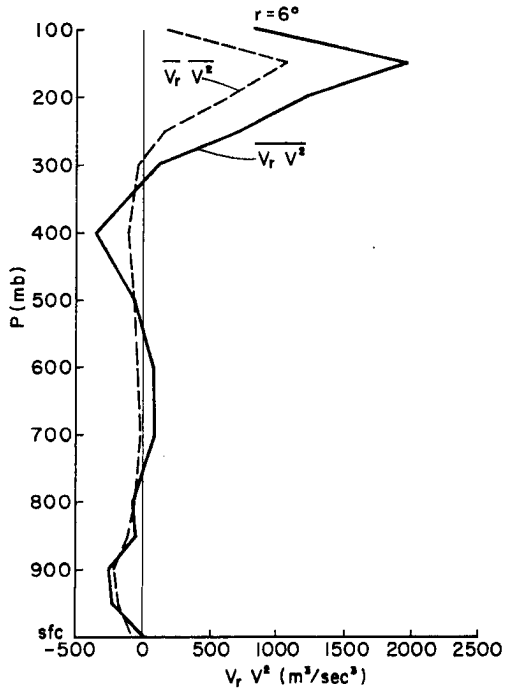

Fig. 8.4. Same as Fig. 8.2 for r=6°.

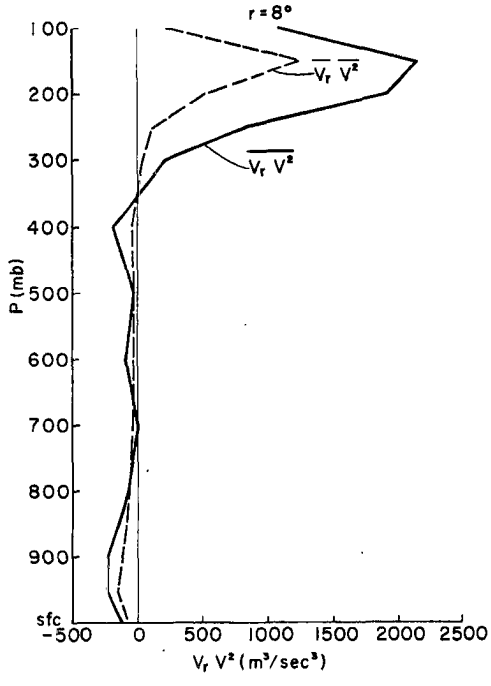

Fig. 8.5. Same as Fig. 8.2 for r=8°.

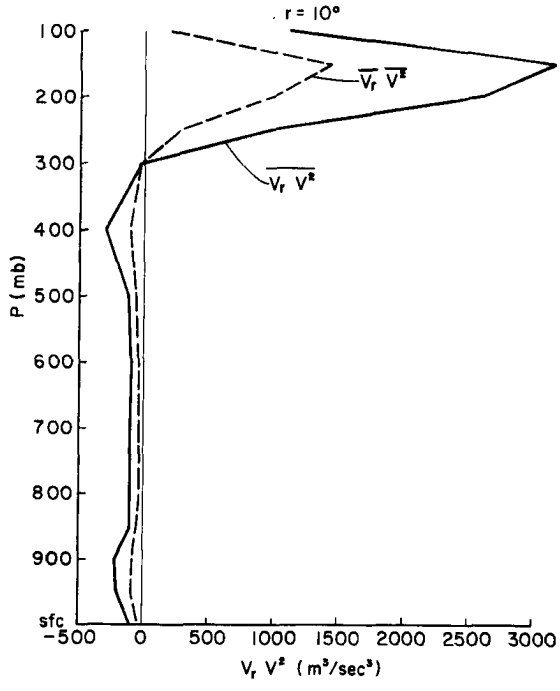

Fig. 8.6. Same as Fig. 8.2 for r=10°.

are only about 60-70 tropical cyclones of typhoon intensity per year worldwide, (Gray, 1975), they obviously do not play a major role in the global kinetic energy budget. Nevertheless, they may be important seasonal sources of kinetic energy to the tropics and to the mid-latitude upper level westerlies.

Vertical profiles of the mean generation of kinetic energy ($\overline{V} \cdot \overline{\nabla\Phi}$) are shown in Figs. 8.7 - 8.10. The generation shows dual maxima at all radii with peaks at 950 mb and 150 mb. At inner radii the lower tropospheric generation is the larger, but from 4° radius outward the outflow layer peak becomes increasingly predominant. No significant variations in these profiles are observed when the octant by octant mean values of $\overline{V} \cdot \overline{\nabla\Phi}$ are computed and averaged. This implies that the generation of

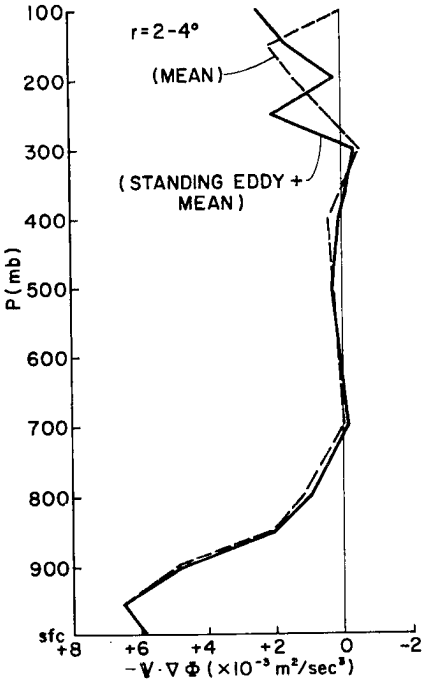

Fig. 8.7. Generation of kinetic energy by the mean circulation ($-\bar{\mathbf{V}} \cdot \overline{\nabla\phi}$) and by the mean + standing eddy circulations for 2-4°.

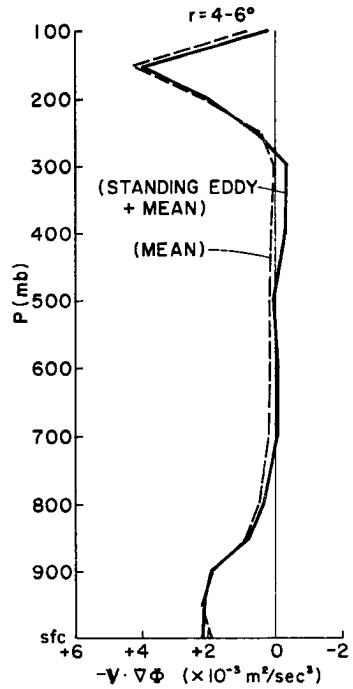

Fig. 8.8. Same as Fig. 8.7 for 4-6°.

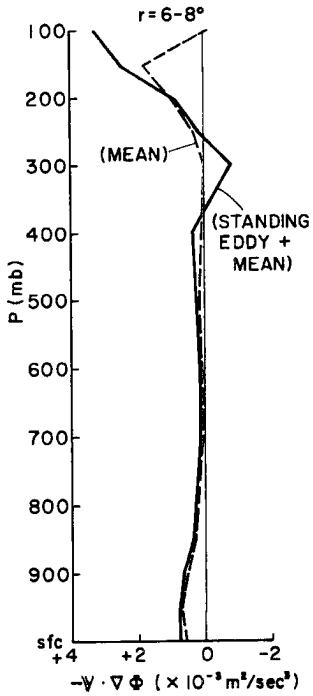

Fig. 8.9. Same as Fig. 8.7 for 6-8°.

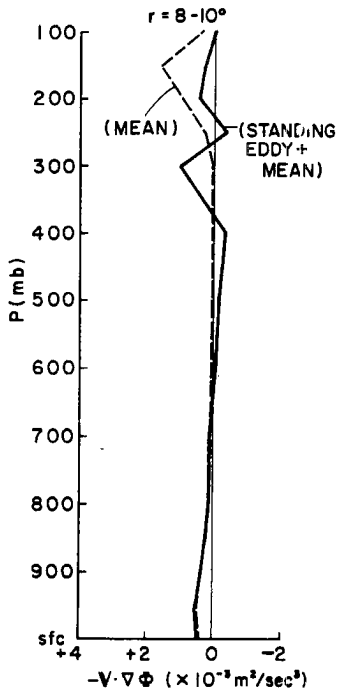

Fig. 8.10. Same as Fig. 8.7 for 8-10°.

kinetic energy by standing eddies is negligible. The role of transient eddies in the generation of K are not negligible, however.

Surface frictional dissipation of kinetic energy (surface to 900 mb) is shown in Table 8.1 along with the K generation by the mean circulation and the horizontal convergence of K. These are net tropospheric values for Sfc to 100 mb. Since surface dissipation is nearly proportional to the cube of the wind speed, it varies substantially with radius. The increases of C_D with wind speed also contribute to this effect

Substantial amounts of kinetic energy also may be dissipated internally within the storm. The strong vertical wind shears, high wind speeds, and strong convection all act to reduce kinetic energy by small scale turbulent processes. The importance of internal dissipation due to clear air turbulence and wave momentum fluxes have been emphasized by Trout and Panofsky (1969) and Lilly (1972) respectively. Convective processes probably dissipate substantial amounts of energy as well. The deep Cb convection of the tropical cyclone may generate small scale eddy or wave turbulence not too unlike that generated by mountain barriers. There is no satisfactory method of estimating this quantitatively. Some studies, from lack of knowledge to the contrary, have estimated the inner core region ratio of internal dissipation to surface dissipation (I.D./S.D.) as about 1 to 1 (Riehl & Malkus, 1961), 1/1 (Miller, 1962) and 0.5/1 (Hawkins & Rubsam, 1968). However, all of these studies solved for internal dissipation as a residual in kinetic energy budgets which neglected eddy generation. Their results probably give underestimates of internal dissipation. It seems safe to say that the magnitude of the internal dissipation of kinetic energy in tropical cyclones and their environments will remain somewhat speculative until the dissipative processes occurring on the cloud or smaller scales are better understood. For the purposes

TABLE 8.1

Vertically Integrated Kinetic Energy Budget (watts/m^2)

(Positive numbers indicate a source of kinetic energy)

Radius:	$2\text{-}4^o$	$4\text{-}6^o$	$6\text{-}8^o$	$8\text{-}10^o$
$\overline{V} \cdot \overline{\nabla\Phi}$	11.9	8.0	3.2	2.5
$\overline{\nabla \cdot V_r V^2}$	-4.9	-8.5	-5.0	-4.3
$\overline{V \cdot F_{sfc}}$	-10.8	-3.7	-1.5	-0.8
Residual	-3.8	-4.2	-3.3	-2.6

of this study it is assumed that internal dissipation is somewhere between 0.5 and 3.0 times the surface dissipation for the $2\text{-}10^o$ region around a mean tropical cyclone.

When the horizontal transport and mean generation terms are vertically integrated from the surface to 100 mb and added to the surface dissipation, the kinetic energy budget of the $2\text{-}10^o$ region is determined as shown in Table 8.1. The residual in Table 8.1 must be equal to the total eddy generation of kinetic energy in the absence of any internal dissipation. The values of eddy generation shown are comparable in magnitude to the mean generation. Table 8.2 shows the kinetic energy budget for an I.D./S.D. ratio of 1.0. For this case eddy generation equals or exceeds mean generation at all radii. It is unlikely that the ratio I.S./S.D. is much less than 0.5. It may be substantially higher (and it may well vary with radius). The required amounts of eddy generation of kinetic energy for different I.D./S.D. ratios are plotted in Fig. 8.11 together with the mean generation. For the probable range of I.D./S.D. ratios (0.5-3.0), the eddy generation is comparable to or greater than the mean generation at all radii. The eddy generation is substantial even when internal dissipation is neglected.

TABLE 8.2

Kinetic Energy Budget (watts/m^2), I.D./S.D. = 1.0

(Positive numbers indicate a source of kinetic energy)

Radius:	2-4°	4-6°	6-8°	8-10°
$\overline{V} \cdot \overline{\nabla\Phi}$	11.9	8.0	3.2	2.5
$\overline{V} \cdot \overline{V_r V^2}$	-4.9	-8.5	-5.0	-4.3
$\overline{V \cdot F_{sfc}}$	-10.8	-3.7	-1.5	-0.8
Internal Dissipation	-10.8	-3.7	-1.5	-0.8
Residual (Balanced by Eddy Generation)	-14.6	-7.9	-4.8	-3.4

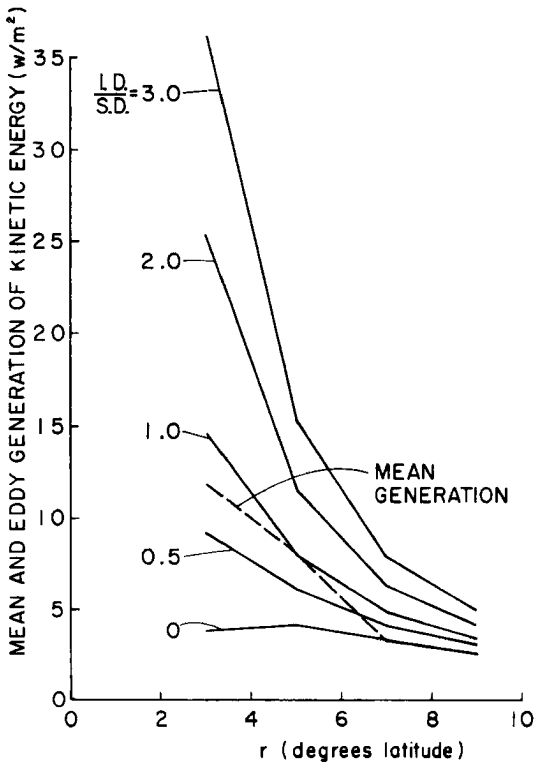

Fig. 8.11. Total eddy generation of kinetic energy for various ratios of internal dissipation (I.D.) to surface dissipation (S.D.). Also shown is the generation by the mean circulation.

It is clear that a substantial amount of the kinetic energy generation in tropical cyclones occurs as an eddy process. At certain radii these eddies may be the predominant generation mechanism. Since the net standing eddy generation is negligible, it may be assumed that transient eddies in the radial and/or tangential flow fields are responsible for all the required eddy generation.

8.4 Discussion

The horizontal eddy fluxes of kinetic energy result from the strong outflow jets at outer radii discussed previously. The source of the eddy generation of K, however, is not so obvious. To determine the vertical distribution of this eddy generation process, a simple model is considered. The region from 2-10^{o} radius is separated into 3 vertical levels: surface to 800 mb, 800-300 mb, 300-100 mb. These levels roughly correspond to the maximum inflow, middle troposphere, and outflow layers respectively. The kinetic energy budget of each layer is computed in the following manner.

Horizontal divergence of V^2 is computed using the smoothed fluxes at 2^{o} and 10^{o} radius shown in Figs. 8.2 and 8.6. Vertical transports of K by the mean circulation are computed from averaged data. Area weighted averages of mean generation ($\overline{V} \cdot \overline{\nabla\Phi}$) are computed and assigned to each level. Surface frictional dissipation is area averaged and assigned to the lowest level. Internal dissipation is assumed to equal surface dissipation ($\frac{I.D.}{S.D.} = 1.0$) and is distributed evenly by mass weighting in the vertical. This estimation of the internal dissipation is only a first approximation, but it should lead to reasonable qualitative results. The residual in each layer is the eddy generation in the absence of any vertical eddy fluxes in kinetic energy. Such eddies

cannot be resolved from this data set. It is assumed that they are small in these computations, but they may not be insignificant. Moncrieff and Green (1972) have shown that the upper level winds and shears can be increased by eddy cloud momentum fluxes. Vertical eddy fluxes of momentum and moist static energy are important in the overall balances of these quantities, and eddy fluxes of K may be likewise important. If such eddies are large, they would affect the vertical distribution of required eddy generation of kinetic energy.

The results are shown in Fig. 8.12. Eddy generation of kinetic energy is the circled number in each box of Fig. 8.12. It is confined almost entirely to the inflow and outflow layers with the latter showing the strongest values. In the outflow layer eddy generation is more than twice as large as the mean generation, and the 4.3 watts/m^2 eddy value is close to the total net production of K over the entire 0-10^o region of 4.8 watts/m^2. Most of the storm's net export of kinetic energy appears to result from transient eddy generation above 300 mb. The eddy generation in the inflow layer balances part of the surface dissipation, and the middle levels require almost no eddy generation.

It must be remembered that this computation assumed a value of I.D./S.D. = 1.0 and neglected vertical eddy fluxes of kinetic energy. Changes in I.D./S.D. would affect the magnitudes of the required eddy generation term somewhat, and vertical eddy fluxes probably cause some redistribution of K in the vertical. Nevertheless, the qualitative results determined from Fig. 8.12 appear valid. Transient eddy generation and the cause of the upper level maximum of this quantity appear to be topics of crucial importance in understanding the energetics of deep convective tropical weather systems and the role of tropical

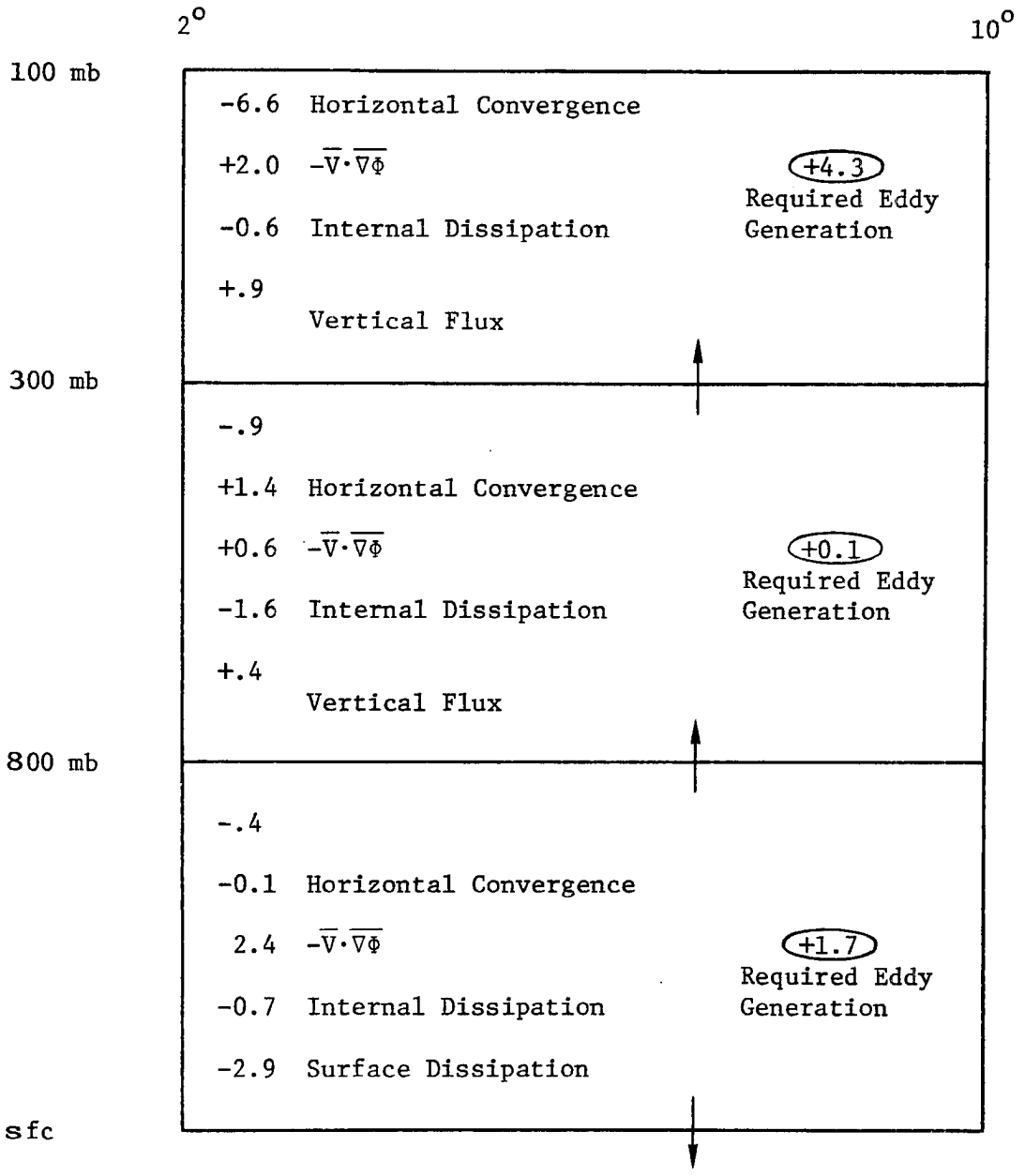

Fig. 8.12. Three level kinetic energy budget. Top left number in each box is the convergence of K by the horizontal circulation. The second number is the generation of K by the mean circulation, the third is the assumed internal dissipation, and the fourth is the gain due to mean vertical transport ($\overline{\omega}\ \overline{K}$). Surface dissipation is also shown in the lowest box. The circled number to the right is the eddy generation of K required for balance. Units = watts/m^2.

cyclones in the general circulation. They should be investigated in future research.

9. SUMMARY AND DISCUSSION

Overall, the success of compositing as an analysis technique for remote or data-sparse weather systems may be one of the most important findings of this study. By proper handling of the data it has been possible to obtain independent budgets which are mutually consistent and physically realistic. Radial wind profiles required only very slight alteration to achieve vertically integrated mass balance, and many eddy characteristics were accurately determined. These factors are strong evidence that the use of compositing to achieve a useful data density can yield accurate quantitative analysis of weather systems. In regions such as the tropics where traditional data sources are scarce or lacking, this may be the only feasible method of performing quantitative analysis. The possible applications of compositing for future research are enormous.

Some of the more specific new findings are discussed below. Particular attention is payed to those results which are most relevant to numerical modeling simulations of tropical cyclones.

Axisymmetry. Most current tropical storm models are axisymmetric (Kasahara, 1961; Ogura, 1964; Yamasaki, 1968; Ooyama, 1969; Rosenthal, 1970; Sundquist, 1970; and Carrier et al., 1971), although some 3-dimensional models are operational (Anthes et al., 1971; Kurihara & Tuleya, 1974, Mathur, 1975). Many features of the observed storm structure are relatively symmetrical, and horizontal eddy fluxes of sensible heat and water vapor are not too large. However, the angular momentum and kinetic energy analyses of Chapters 7 and 8 show very large eddy fluxes of these quantities at outer radii. Unless these fluxes can be parameterized, it is doubtful whether an axisymmetric model can

be considered realistic. Some of the observed similarities between the circulations of such models and observed tropical storms are probably fortuitous. The eddy generation, dissipation, and export of kinetic energy are all large terms which tend to cancel, but this does not justify their neglect. Eddy momentum fluxes are required to obtain realistic momentum balance in the outflow layer at large radii and to compensate for standing eddies in the Coriolis torque term. Although many features of the tropical cyclone's inner circulation may be modeled adequately in 2-dimensions, the author does not believe that such models can yield realistic simulations of the outer cyclone regions.

Observed Structure. The large scale structure of tropical cyclones is well documented in Chapters 2 and 3, but several features are particularly important. The deep inflow from 4^{o} radius outward is not simulated in most models which generally depend on low level frictional convergence alone to force their radial circulations. It appears that most of the middle level inflow subsides into the boundary layer before being cycled upward in clouds. The exact cause of the mid-level inflow is not clear, but this phenomenon has a significant effect on the overall storm moist static energy budget. The magnitude of this inflow casts doubt on the use of CISK as the exclusive forcing mechanism of tropical cyclones. The poor correlation of vorticity and convergence in the boundary layer also suggests that a reevaluation of CISK is needed.

The soundings of section 2.4 show more conditional instability at inner radii than usually is assumed, and mid-level humidities are higher than expected. The inner regions show substantial potential for buoyant convection except in the eye. The available data do not show constant vertical profiles of h (or θ_e) or moist adiabatic lapse

rates at inner radii. It must be emphasized that soundings inside $r = 0.7^{o}$ are based on flight data from Gray & Shea (1973).

The scale of the circulation is very large. Even at 14^{o} radius there is substantial mean radial flow. Upper level mean and eddy radial fluxes of momentum and kinetic energy are large at outer radii. The common assumption of a closed boundary at 1000 km radius or so does not seem justified. The outer circulation may be independent of inner core structure.

Cumulus Parameterization. All tropical cyclone models must use some sort of cumulus parameterization scheme to simulate the latent heating processes. The results of Chapter 6 indicate substantial convection at all radii and large amounts of vertical mass recycling everywhere beyond the eyewall region, especially in the lower troposphere. The moist static energy budget analysis suggests that parameterization schemes should include the effects of Cb overshoot cooling and extracloud subsidence at values of $\tilde{h}$ higher than the observed $\overline{h}$. Deep convection seems well related to low level (sfc to $\sim$ 800 mb) convergence, while shallow clouds are probably more closely related to low level winds, turbulence and humidities. The effects of ice phase transitions are probably negligible except in areas of extremely intense Cb convection. Spectral cloud parameterization schemes may have to adjust the types of clouds used according to the type of organization of the deep convection. Vertical momentum fluxes by clouds should be parameterized as discussed below.

Sea Surface Fluxes. Estimates of sea surface fluxes of sensible heat, moisture, momentum and kinetic energy obtained by using conventional bulk aerodynamic theory give realistic results in the budget

studies of Chapters 5-8. A constant sensible heat/evaporation coefficient of 1.5×10^{-3} applied to the 900 mb winds seems adequate for fluxes of those quantities. The sensible and latent heat fluxes of this study are considerably smaller than the estimates of most previous empirical studies. A variable drag coefficient applied to the 900 mb winds gives better estimates of momentum and kinetic energy fluxes (see Chapter 7).

Radiation. The observed diurnal variations in tropical storm convection and temperatures (Chapter 4) indicate that cloud/cloud free radiation differences should be incorporated into tropical cyclone models. The radiational forcing occurs day and night and may well be a factor in such important storm features as the middle level inflow. Since the dominant factor in the radiation budget is the existence of dense cirrus cover, the extent of the cirrus shield must be predicted.

Angular Momentum. In addition to the importance of horizontal eddy transports of momentum mentioned above, it must be noted that the Coriolis torque term ($fV_r r$) does not integrate to zero in a region containing persistent northerly or southerly flow. At large radii this may become a major term in the angular momentum budget.

Vertical eddy fluxes of momentum by cumulus clouds are required to explain the observed circulation. They should be included in cumulus parameterization schemes wherever vertical wind shears are significant. As a first approximation, angular momentum can be treated as a conserved quantity in clouds.

Kinetic Energy. The use of mean circulation quantities alone gives a poor facsimile of the true kinetic energy budget. Horizontal eddy fluxes are large, and internal dissipation and eddy generation are

substantial - perhaps dominant. The large scale storm circulation is a strong source of kinetic energy exporting about 4.8 watts/m^2 averaged over the 0-10^o radius region.

Future Research. The compositing technique developed for this study has been applied to the same data set to study tropical cyclone motion (George, 1975) and to N.W. Pacific cloud cluster data to analyze storm genesis (Zehr, 1976). The Pacific data set is being expanded to 20 years, and 20 years of Atlantic data has been acquired to further research on all facets of tropical cyclone structure, energetics, motion and genesis.

ACKNOWLEDGEMENTS

The author gratefully acknowledges the support and guidance of his advisor, Professor William M. Gray. The author has been fortunate to have had the previously assembled 10-year West Pacific Rawinsonde data set of Professor Gray's project at his disposal and the extensive numerical programming assistance of Mr. Edwin Buzzell and Mr. Charles Solomon. Thanks are also extended to Mrs. Barbara Brumit and Mrs. Dianne Schmitz for assistance in data reduction and manuscript preparation.

This research has been partially supported by the National Science Foundation Grant No. ATM75-01424 A01 with significant supplemental financial support from National Oceanic and Atmospheric Administration (National Environmental Satellite Services) Grant No. 04-3-158-51, #3, and National Oceanic and Atmospheric Administration (National Hurricane Experimental Meteorology Laboratory) Grant No. 04-6-022-44021, #1. The U.S. Navy Environmental Prediction Research Facility (through Mr. Samson Brand) arranged for the card punching of the Japanese rawinsonde stations used in this study.

BIBLIOGRAPHY

Albrecht, B. and S. K. Cox, 1975: The large-scale response of the tropical atmosphere to cloud-modulated infrared heating. J. Atmos. Sci., 32, 16-24.

Anthes, R., S. L. Rosenthal and J. W. Trout, 1971: Preliminary results from an asymmetric model of the tropical cyclone. Mon. Wea. Rev. 99, 744-758.

Anthes, R., 1974: The dynamics and energetics of mature tropical cyclones. Rev. of Geoph. & Space Phys., Vol. 12, No. 3, 495-522 pp.

Arakawa, A. and W. H. Schubert, 1974: Interaction of a cumulus cloud ensemble with the large scale environment, Part 1, J. Atmos. Sci. 31, 674-701.

Arnold, C. A., 1977: Forthcoming CSU report on tropical cyclone convection using DMSP satellite data.

Ausman, M., 1959: Some computations of the inflow angle in hurricanes near the ocean surface. Univ. of Chicago Dept. of Meteor. Res. Rept., 19 pp.

Black, P. G. and R. A. Anthes, 1971: On the asymmetric structure of the tropical cyclone outflow layer. J. Atmos. Sci., 1348-1366.

Brand, S., 1971: The effects on a tropical cyclone of cooler surface waters due to upwelling and mixing produced by a prior tropical cyclone. J. Appl. Meteor. 10, 865-874.

Byers, H. R., 1944: "General Meteorology": 2nd, ed., McGraw-Hill, N.Y., 578-581 pp.

Carrier, G. F., A. L. Hammond and O. D. George, 1971: A model of the mature hurricane. J. Fluid Mech. Vol. 47, Part 1, 145-170 pp.

Cho, H. R. and Y. Ogura, 1974: A relationship between cloud activity and the low-level convergence as observed in Reed-Recker's composite easterly waves. J. Atmos. Sci., 31, 2058-2065.

Cline, I. M., 1926: "Tropical Cyclones", The Macmillan Co., New York, 301 pp.

Cotton, W. R., 1972: Numerical simulation of precipitation development in supercooled cumuli. Mon. Wea. Rev. 100, No. 11, 757-783 pp.

Cry, G. W., 1967: Effects of tropical cyclone rainfall on the distribution of precipitation over the eastern and southern United States. ESSA Professional Paper 1, available from U.S. Government Printing Office, Washington, D.C.

Dopplick, T. G., 1970: Global radiative heating of the earth's atmosphere. Rept. No. 24, Planetary Circulation Project, Dept. of Meteor., M.I.T. 128 pp.

Dopplick, T. A., 1974: Radiative heating in the atmosphere in the General Circulation of the Tropical Atmosphere and Interactions With Extratropical Latitudes, Vol. 2, by Newell, Kidson, Vincent, and Boer, M.I.T. Press, Cambridge, 1-25.

Dunn, G. E. and B. I. Miller, 1964: "Atlantic Hurricanes", 2nd ed., Louisiana St. U. Press, Baton Rouge, 377 pp.

Erickson, C. O. and J. S. Winston, 1972: Tropical storm, mid-latitude cloud-band connections and the autumnal buildup of the planetary circulation. J. Appl. Meteor., 11, 23-36.

Fendell, F. E., 1974: "Tropical Cyclones", Advances in Geophysics, N.Y., Vol. 17, 2-100 pp.

Foltz, Gary S., 1976: Diurnal variation of the tropospheric energy balance. M.S. Thesis. Colo. State Univ. Atmos. Sci. Dept., Ft. Collins, CO, 135 pp.

George, J.E., 1975: Tropical cyclone motion and surrounding parameter relationships. Colo. State Univ., Atmos. Sci. Paper No. 214, 105 pp.

Gentry, R. C., 1964: A study of hurricane rainbands. National Hurricane Res. Proj. Rept. No. 69, 85 pp., (available from NOAA Weather Bureau, Miami office).

Gray, W. M., 1962: On the balance of forces and radial accelerations in hurricanes. Quart. J. Roy. Meteor. Soc., 88, 430-458 pp.

Gray, W. M., 1966: On the scales of motion and internal stress characteristics of the hurricane, J. Atmos. Sci., 23, 278-288 pp.

Gray, W. M., 1967: The mutual variation of wind, shear and baroclinicity, in the cumulus convective atmosphere of the hurricane. Mon Wea. Rev., 95, 55-73.

Gray, W. M., 1973: Cumulus convection and large scale circulations, Part I: Broadscale and meso-scale interactions, Mon. Wea. Rev., 101, 839-855 pp.

Gray, W. M. and D. J. Shea, 1973: The hurricane's inner core region, II. Thermal stability and dynamic characteristics, J. Appl. Meteor. 30, 8, 1565-1576.

Gray, W. M., E. Ruprecht, and R. Phelps, 1975: Relative humidity in tropical weather systems, Mon. Wea. Rev., 103, 8, 685-690.

Gray, W. M., 1975: Tropical cyclones genesis. Colo. State Univ., Atmos. Sci. Paper No. 243; Ft. Collins, CO, 119 pp.

Gray, W. M., W. M. Frank and J. E. George, 1975: Typhoon studies in support of Project Stormfury, Unpublished report to NOAA, available from Colo. State Univ., Dept. of Atmos. Sci., Ft. Collins, CO.

Gray, W. M., 1976: Diurnal variation of oceanic deep cumulus convection. Paper II: Physical hypothesis. Colo. State Univ., Atmos. Sci. Paper No. 243, Ft. Collins, CO, 106 pp.

Hawkins, H. F., and D. T. Rubsam, 1968: Hurricane Hilda, 1964: II. Structure and budgets of the hurricane on October 1, 1964. Mon. Wea. Rev., 99, 427-434.

Hawkins, H. F. and S. M. Imbembo, 1976: The structure of a small, intense hurricane - Inez 1966. Mon. Wea. Rev. 104, 418-442 pp.

Hughes, L. A., 1952: On the low level wind structure of tropical cyclones, J. Meteor. 9, 442-428 pp.

Izawa, T., 1964: On the mean wind structure of typhoons. Japan Typhoon Research Laboratory. Tech. Note. No. 2, 45 pp.

Jacobson, R. W., Jr. and W. M. Gray, 1976: Diurnal variation of oceanic deep cumulus convection. Colo. State Univ., Dept. of Atmos. Sci. Paper No. 243, Ft. Collins, CO,106 pp.

Jordan, E. S., 1952: An observational study of the upper wind circulation around tropical storms. J. Meteor. 9, No. 5, 340-346 pp.

Jordan, C. L., 1958: Mean soundings for the West Indies area. J. Appl. Meteor., 15, 1, 91-97.

Jordan, C. L., 1961: Marked changes in the characteristics of the eye of intense typhoons between the deepening and filling stages. J. Meteor., 18, 779-789.

Kasahara, A., 1961: A numerical experiment on the development of a tropical cyclone. J. Meteor. 18, No. 3, 259-282.

Kraus, E. B., 1972: "Atmosphere-Ocean Interaction," Oxford Univ. Press (Clarendon), London and New York.

Kung, E. C., 1967: Diurnal and long-term variations of the kinetic energy generation and dissipation for a five-year period. Mon. Wea. Rev., 95, 9, 593-606 pp.

Kurihara, Y. and R. E. Tuleya, 1974: Structure of a cyclone developed in a three-dimensional numerical simulation model. J. Atmos. Sci. 31, No. 4, 893-919 pp.

LaSeur, N. E. and H. F. Hawkins, 1963: An analysis of hurricane Cleo, (1958) based on data from research reconnaissance aircraft. Mon. Wea. Rev. 91, 694-709 pp.

Leipper, D. F., 1967: Observed ocean conditions and Hurricane Hilda, 1964. J. Atmos. Sci., 24, 182-196.

Lilly, D. K., 1972: Wave momentum flux-a GARP problem, Bull. Amer. Meteor. Soc., 20, 17-23 pp.

Lopez, R. E., 1968: Investigation of the importance of cumulus convection and ventilation in early tropical storm development. Colo. State Univ., Atmos. Sci, Paper No. 124, Ft. Collins, CO, 86 pp.

Lopez, R. E., 1973: Cumulus convection and larger scale circulations. Part II: Cumulus and mesoscale interactions. Mon. Wea. Rev., 101, 856-870 pp.

Malkus, J. S. and H. Riehl, 1960: On the dynamics and energy transformations in steady-state hurricanes. Tellus 12, 1-20.

Malkus, J. S., C. Ronne and M. Chaffee, 1961: Cloud patterns in Hurricane Daisy, 1958. Tellus, 13, 8-30.

Mathus, M. B., 1975: Development of a banded structure in a numerically simulated hurricane. J. Atmos. Sci. 32, 3, 512-522 pp.

Miller, B. I., 1958a: Rainfall rates in Florida hurricanes. Mon. Wea. Rev., 86(7), 258-264.

Miller, B. I., 1958b: The three dimensional wind structure around a tropical cyclone. National Hurricane Res. Proj. Rept. No. 15, 41 pp. (Available from NOAA Weather Bureau, Miami office).

Miller, B. I., 1962: On the momentum and energy balance of hurricane Helene (1958). National Hurricane Res. Proj. Rept. No. 53, 19 pp. (Available from NOAA Weather Bureau, Miami office).

Moncrieff, M. W. and J. S. A. Green, 1972: The propegation and transfer properties of steady convective overturning in shear, Quart. J. Roy. Meteor. Soc., 98, 336-352 pp.

Newell, R. E., J. W. Kindson, D. G. Vincent, and G. J. Boer, 1972: The general circulation of the tropical atmosphere and interactions with extratropical latitudes. MIT Press, Cambridge, Mass., 258 pp.

Nitta, T., 1975: Observational determination of cloud mass flux distributions. J. Atmos. Sci. 32, 73-91 pp.

Ogura, Y., 1964: Frictionally controlled, thermally driven circulations in a circular vortex with application to tropical cyclones. J. Atmos. Sci. 21, 610-621 pp.

Ogura, Y. and H. R. Cho., 1973: Diagnostic determination of cumulus cloud populations from observed large-scale variables. J. Atmos Sci., 30, 1276-1286.

Ooyama, K., 1969: Numerical simulation of the life cycle of tropical cyclones. J. Atmos. Sci., 26, 3-40.

Ostlund, H. G., 1968: Hurricane tritium II. Air-sea exchange of water in Betsy 1965. Tellus 20, 577-594.

Ostlund, H. G., 1970: Hurricane tritium III. Evaporation of sea water in Hurricane Faith 1966. J. Geophys. Res., 75, 2303-2309 pp.

Palmén, E. H., 1948: On the formation and structure of tropical cyclones. Geophysica, Helsinki, 31, 26-38 pp.

Palmén, E. H., and C. L. Jordan, 1955: Note on the release of kinetic energy in tropical cyclones Tellus 7, 186 pp.

Palmén, E. H. and Riehl, 1957: Budget of angular momentum and energy in tropical storms. J. Meteor., 14, 150-159 pp.

Palmén, E. H., 1958: Vertical circulation and release of kinetic energy during the development of Hurricane Hazel into an extratropical storm. Tellus 10, No. 1, 1-23 pp.

Pfeffer, R. L., 1958: Concerning the mechanics of hurricanes. J. Meteor. 15, 113-120 pp.

Reed, R. J. and E. E. Recker, 1971: Structure and properties of synoptic scale wave disturbances in the equatorial western Pacific. J. Atmos. Sci. 28, 1117-1133.

Riehl, H., 1961: On the mechanisms of angular momentum transports in hurricanes. J. Meteor., 18, 113-115 pp.

Riehl, H., 1963: Some relations between wind and thermal structure of steady hurricanes, J. Atmos. Sci., 20, 276-287 pp.

Riehl, H. and J. S. Malkus, 1961: Some aspects of Hurricane Daisy, 1958. Tellus, 13, 181-213 pp.

Robinson, M. K. and R. A. Bauer, 1971: Atlas of monthly mean sea surface and subsurface temperature and depth of the top of the thermocline North Pacific Ocean. Fleet Numerical Weather Central Rept., 96 pp. Monterey, Calif.

Roll, H. U., 1965: "Physics of the Marine Atmosphere", Academic Press, New York, N.Y., 426 pp.

Rosenthal, S. L., 1970: A circularly symmetric primitive equation model of tropical cyclone development containing an explicit water vapor cycle. Mon. Wea. Rev., 98, 643-663.

Rosenthal, S. L., 1971: The response of a tropical cyclone model to variations in boundary layer parameters, initial conditions, lateral boundary conditions and domain size. Mon. Wea. Rev. 99 (10), 767-777 pp.

Ruprecht, E. and W. M. Gray, 1974: Analysis of satellite-observed cloud clusters. Colo. State Univ., Atmos. Sci. Paper No. 219, Ft. Collins, CO, 91 pp.

Sadler, J. C., 1975: The upper tropospheric circulation over the global tropics, U. of Hawaii Met. Dept. Report No. UH MET-75-05, 35 pp.

Shea, D. J. and W. M. Gray, 1973: The hurricane's inner core region: I, Symmetric and asymmetric structure II. Thermal stability and dynamic characteristics. J. Atmos. Sci. 30, 1544-1576 pp.

Sheets, R. C., 1967a: On the structure of Hurricane Janice (1958). National Hurricane Res. Lab. Rept. No. 76, 30 pp. (available from NOAA Weather Bureau, Miami office).

Sheets, R. C., 1967b: On the structure of Hurricane Ella (1962). National Hurricane Res. Lab. Rept. No. 77, 33 pp. (available from NOAA Weather Bureau, Miami office).

Sheets, R. C., 1968: On the structure of Hurricane Dora (1964). National Hurricane Res. Lab. Rept. No. 83, 64 pp. (available from NOAA Weather Bureau, Miami office).

Schoner, R. W., 1957: Frequency and distribution of areal rainfall associated with tropical storms entering the coast of the United States (Texas to Maine). U.S. Weather Bureau, Hydrolic Svc. Div., Washington, D. C., 60 pp. (unpublished).

Simpson, R. H., 1952: Exploring the eye of Typhoon Marge, 1951, Bull. Amer. Meteor. Soc., 33, 7, 286-298 pp.

Simpson, R. H. and L. G. Starrett, 1955: Further studies of hurricane structure by aircraft reconnaissance, Bull. Amer. Meteor. Soc., 36, 9, 459-468.

Sundquist, H., 1970: Numerical simulation of the development of tropical cyclones with a ten-level model, Part 1. Tellus 12, 359-390 pp.

Trout, D. and H. A. Panofsky, 1969: Energy dissipation near the tropopause. Tellus, 21, 355-358 pp.

Williams, K. T. and W. M. Gray, 1973: Statistical analysis of satellite observed cloud clusters in the western North Pacific. Tellus, 25, 178-201 pp.

Yamasaki, M., 1968: Numerical simulation of tropical cyclone development with the use of primitive equations. J. Meteor. Soc. Japan 46, 178-201 pp.

Yanai, M., 1961: A detailed analysis of typhoon formation. J. Meteor. Soc. Japan 39, 187-214 pp.

Yanai, M., S. Esbensen, and J. H. Chu, 1973: Determination of bulk properties of tropical cloud clusters from large-scale heat and moisture budgets. J. Atmos. Sci., 30, 611-627.

Yanai, M., J. H. Chu, T. E. Stark and T. Nitta, 1976: Response of deep and shallow tropical maritime cumuli to large-scale processes. J. Atmos. Sci., 33, 6, 976-991 pp.

Zehr, Raymond M., 1976: Typhoon genesis and pre-typhoon cloud clusters. M.S. Thesis, Colo. State Univ., Atmos. Sci. Dept., Ft. Collins, CO, 79 pp.

Zipser, E. J., 1964: On the thermal structure of developing tropical cyclones. National Hurricane Res. Proj. Rept. No. 67, 23 pp. (Available from the NOAA Weather Bureau, Miami office).

W. M. GRAY'S FEDERALLY SUPPORTED RESEARCH PROJECT REPORTS SINCE 1967

CSU Dept. of Atmos. Sci. Report No.	Report Title, Author, Date, Agency Support
104	The Mutual Variation of Wind, Shear, and Baroclinicity in the Cumulus Convective Atmosphere of the Hurricane (69pp). W. M. Gray. February 1967. NSF Support.
114	Global View of the Origin of Tropical Disturbances and Storms (105pp). W. M. Gray. October 1967. NSF Support.
116	A Statistical Study of the Frictional Wind Veering in the Planetary Boundary Layer (57pp). B. Mendenhall. December 1967. NSF and ESSA Support.
124	Investigation of the Importance of Cumulus Convection and Ventilation in Early Tropical Storm Development (88pp). R. Lopez. June 1968. ESSA Satellite Lab. Support.
Unnumbered	Role of Angular Momentum Transports in Tropical Storm Dissipation over Tropical Oceans (46pp). R. F. Wachtmann. December 1968. NSF and ESSA Support.
Unnumbered	Monthly Climatological Wind Fields Associated with Tropical Storm Genesis in the West Indies (34pp). J. W. Sartor. December 1968. NSF Support.
140	Characteristics of the Tornado Environment as Deduced from Proximity Soundings (55pp). T. G. Wills. June 1969. NOAA and NSF Support.
161	Statistical Analysis of Trade Wind Cloud Clusters of the Western North Pacific (80pp). K. Williams. June 1970. ESSA Satellite Lab. Support.
---	A Climatology of Tropical Cyclones and Disturbances of the Western Pacific with a Suggested Theory for Their Genesis/ Maintenance. W. M. Gray. NAVWEARSCHFAC Technical Paper No. 19-70 (225pp). November 1970. (Available from U.S. Navy, Monterey, CA). U.S. Navy Support.
179	A Diagnostic Study of the Planetary Boundary Layer over the Oceans (95pp). W. M. Gray. February 1972. Navy and NSF Support.
182	The Structure and Dynamics of the Hurricane's Inner Core Area (105pp). D. J. Shea. April 1972. NOAA and NSF Support.
188	Cumulus Convection and Larger-Scale Circulation, Part I: A Parametric Model of Cumulus Convection (100pp). R. E. Lopez. June 1972. NSF Support.

CSU Dept. of Atmos. Sci. Report No.	Report Title, Author, Date, Agency Support
189	Cumulus Convection and Larger-Scale Circulations, Part II: Cumulus and Meso-Scale Interactions (63pp). R. E. Lopez. June 1972. NSF Support.
190	Cumulus Convection and Larger-Scale Circulations, Part III: Broadscale and Meso-Scale Considerations (80pp). W. M. Gray. July 1972. NOAA-NESS.
195	Characteristics of Carbon Black Dust as a Tropospheric Heat Source for Weather Modification (55pp). W. M. Frank. January 1973. NSF Support.
196	Feasibility of Beneficial Hurricane Modification by Carbon Black Seeding (130pp). W. M. Gray. April 1973. NOAA Support.
199	Variability of Planetary Boundary Layer Winds (157pp). L. R. Hoxit. May 1973. NSF Support.
200	Hurricane Spawned Tornadoes (57pp). D. J. Novlan. May 1973. NOAA and NSF Support.
212	A Study of Tornado Proximity Data and an Observationally Derived Model of Tornado Genesis (101pp). R. Maddox. November 1973. NOAA Support.
219	Analysis of Satellite Observed Tropical Cloud Clusters (91 pp). E. Ruprecht and W. M. Gray. May 1974. NOAA-NESS Support.
224	Precipitation Characteristics in the Northeast Brazil Dry Region (56pp). R. P. L. Ramos. May 1974. NSF Support.
225	Weather Modification through Carbon Dust Absorption of Solar Energy (190pp). W. M. Gray, W. M. Frank, M. L. Corrin, and C. A. Stokes. July 1974.
234	Tropical Cyclone Genesis (121pp). W. M. Gray. March 1975. NSF Support.
---	Tropical Cyclone Genesis in the Western North Pacific (66pp). W. M. Gray. March 1975. U.S. Navy Environmental Prediction Research Facility Report. Technical Paper No. 16-75. (Available from the U.S. Navy, Monterey, CA). Navy Support.
241	Tropical cyclone Motion and Surrounding Parameter Relationships (105pp). J. E. George. December 1975. NOAA Support.

CSU Dept. of Atmos. Sci. Report No.	Report Title, Author, Date, Agency Support
243	Diurnal Variation of Oceanic Deep Cumulus Convection. Paper I: Observational Evidence, Paper II: Physical Hypothesis (106pp). R. W. Jacobson, Jr. and W. M. Gray. February, 1976. NOAA NESS Support.